Engineering coherent photons from semiconductor quantum dots

Ralph N. E. Malein, MPhysPhil (Oxon)

Thesis submitted for the degree of Doctor of Philosophy

Heriot-Watt University

School of Engineering and Physical Sciences

June 2015

Abstract

Self-assembled semiconductor quantum dots (QDs) have great promise as quantum light sources due to their ability to generate single indistinguishable photons and entanglement. In this thesis, confocal microscopy experiments have been carried using non-resonant photoluminescence (PL) and resonant fluorescence (RF) on QDs with the goal of characterising and developing them into high-quality quantum light sources.

Through the application of uniaxial strain and an electric field, single particle energies in a QD and their behaviour with strain are determined using a perturbative Coulomb blockade model. The exciton energy tuning magnitude is found to be a result of the near-cancellation of much larger single electron and hole tuning tuning. In addition, the rate of electron confinement energy tuning with strain is found to be correlated with the nominal unstrained confinement energy. An attempt is made at characterising the composition of the QDs through extracting deformation potentials, but the simple model does not capture the full system. Further, strain tuning of the fine structure splitting (FSS) of the neutral exciton X^0 from QDs emitting at telecommunications wavelengths is shown. FSS tuning as large as 46 μeV was observed, and using a phenomenological model select QDs were identified to achieve FSS $< 1\mu$eV.

RF is used to examine noise sources in QDs. Two sources of noise are considered: electric charge noise due to a fluctuating charge environment, and nuclear spin noise due to the hyperfine interaction of single electron spins with a large number ($\sim 10^5$) of nuclear spins. While the charge noise contributes to a loss in overall photon emission rates, but does not negatively impact the photon antibunching or indistinguishability at low Rabi frequencies, spin noise allows inelastic Raman scattering which reduces photon indistinguishability. The application of an external magnetic field in the Faraday geometry screens the electrons from the nuclear spins, recovering a high degree of photon indistinguishability.

For my grandfather, Tony Malein

Acknowledgements

Firstly, I'd like to thank Professor Brian Gerardot for being an excellent and patient supervisor. I would never have been able to complete this thesis without his guidance and motivation. I must also thank him for giving me the opportunity to continue working with him in the fabled "new lab" whenever it's finally completed.

Secondly, I'd like to thank the members of the Quantum Photonics Lab, both current and past, for their help and guidance throughout my PhD. Thanks to Chris Kuklewicz for taking me under his wing for my first few months at HWU and teaching me a lot more than I really needed to know; to Joanna Zajac and Ted Santana for their hard work running the RF experiments with me, after much alignment, collimation and realignment to squeeze as much signal-to-noise out of the system as was possible; to Luca Sapienza and Rima Al-Khuzeyri for their infinite patience running the 1300nm strain experiments with me, where even a simple measurement could take hours; to Yong Ma for providing me with the brightest samples in the world and the technique to process them myself; to Santosh Kumar for help with the attempt to take a shortcut to determine QD composition – we'll do it somehow, it just won't be as easy as we expected; and to everyone else: Tunmise Dada, Pragati Kumar, Art Kaczmarczyk, Guillem Ballisteros-Garcia and Antonis Koutroumanis for making the QPL great.

I thank my family: Mum, Dad, Alice, Edmund, and everyone else; I also thank my friends, scattered around the world, too numerous to name. I've really appreciated all your support, even though I don't see you all as often as I should. In particular, I thank Thomas Schratwieser for being a great friend and flatmate and preventing me going crazy from isolation: when you're all alone in a new city, it's always a good move to find someone approximately the same amount of nerdy as you and band together to avoid hermithood.

Last, but by no means least, thank you to Rebecca. I don't think I would have been able to do this without you.

ACADEMIC REGISTRY
Research Thesis Submission

Name*:*			
School/PGI:			
Version: *(i.e. First, Resubmission, Final)*		Degree Sought (Award **and** Subject area)	

Declaration

In accordance with the appropriate regulations I hereby submit my thesis and I declare that:

1) the thesis embodies the results of my own work and has been composed by myself
2) where appropriate, I have made acknowledgement of the work of others and have made reference to work carried out in collaboration with other persons
3) the thesis is the correct version of the thesis for submission and is the same version as any electronic versions submitted*.
4) my thesis for the award referred to, deposited in the Heriot-Watt University Library, should be made available for loan or photocopying and be available via the Institutional Repository, subject to such conditions as the Librarian may require
5) I understand that as a student of the University I am required to abide by the Regulations of the University and to conform to its discipline.

* *Please note that it is the responsibility of the candidate to ensure that the correct version of the thesis is submitted.*

Signature of Candidate*:*		Date:	

Submission

Submitted By *(name in capitals):*	
Signature of Individual Submitting:	
Date Submitted:	

For Completion in the Student Service Centre (SSC)

Received in the SSC by *(name in capitals):*			
Method of Submission *(Handed in to SSC; posted through internal/external mail):*			
*E-thesis Submitted (**mandatory for final theses)***			
Signature:		Date:	

Please note this form should bound into the submitted thesis.

Updated February 2008, November 2008, February 2009, January 2011

Contents

Chapter 1

Semiconductor quantum dots

In this chapter, I will describe the motivation for this thesis and then introduce the background and state-of-the-art for strain tuning of self-assembled quantum dots (QDs), and generation of indistinguishable photons from exciton transitions in QDs.

1.1 Motivation

QDs are promising candidates for many potential applications in quantum technologies. A QD is the extension of a 2D quantum well or 1D quantum wire to 0D, or, equally, a region of very high confinement (whether of electrons, holes or excitons) in 3 dimensions. There are many ways to facilitate this confinement, such as electrostatically "cordoning off" part of a 2D electron gas, or using a semiconductor heterostructure band structure to trap electrons or holes in small regions where lower energy states are allowed. It is the latter of these examples that I will concentrate on.

Semiconductor heterostructure quantum dots take the form of a very small region of one semiconductor (eg. InAs) embedded in a semiconductor with a larger band gap (eg. GaAs). They confine excitons and can be optically excited to produce an electron-hole pair, which bind together into an exciton. The strength of the confinement, and so the energies of the electron and hole (which give the transition energy of exciton creation and recombination) are determined by the band gap and size of the QD. Thus it is possible to pre-select, to a degree, the emission wavelength of a QD during the growth process. QDs are sometime known as "artificial atoms" due to the fact that electrons within a QD act very much like electrons in a single shell of an atom, with very sharp, discrete energy levels and transitions between them. However, QDs are made up of up to 10^6 atoms in a crystal, so are much easier to work with than single atoms, as they can be incorporated into solid-state semiconductor devices, which allows for example simple application of electric fields or deterministic charging via a field-effect device structure, or embedding the QD

within an optical cavity to enhance optical coupling into and out of the QD. Working with single atoms, on the other hand, requires isolating them in an electrostatic trap which is much more complex than working with solid-state semiconductors.

One of the significant future applications of QDs is in linear optical quantum computing (LOQC). This is the processing of quantum information encoded in polarisation and phase states of photons using beamsplitters, polarising beamsplitters, wave plates and phase shifts (see eg. Ref. [1] for further discussion). Two vital requirements for LOQC are sources that emit single photons, and sources that emit indistinguishable photons. A third property that is desirable is the ability to generate polarisation-entangled pairs of photons.

Another potential application is in quantum repeaters[2, 3]. Quantum repeaters in quantum communication are analogous to signal amplifiers in long-distance classical communication: quantum communication relies on maintaining entanglement between two particles over large distances, but such entangled states will decohere with time, predominately due to fibre losses over large distances in the case of optical communication. Quantum repeaters can be used to break a large distance L into $N = 2^n$ smaller intermediate steps of length L/N, and then to perform entanglement swapping on these entangled pairs to end up with the particles at either end of L being entangled. It is clear that sources of entanglement are thus vital for quantum repeaters. Implementation of quantum repeaters also requires "quantum memories" to store the entangled states while the necessary teleportation processes are carried out. Single electron spins in charge-tunable QDs could be used to store polarisation states of photons[4, 5]

In order for self-assembled QDs to be viable for use as light sources in these technologies, there are three major properties of their emission that must be considered: their brightness, the indistinguishability of the photons emitted and their ability to generate entangled photons.

1.1.1 Collection efficiency

Exciton states in self-assembled quantum dots generally have fluorescence lifetimes on the order of 1 ns corresponding to a photon emission rate on the order of 1 GHz at saturation. Self-assembled QDs are, however, embedded in a semiconductor substrate such as GaAs. The refractive index mismatch between the semiconductor and free space means that the critical angle is very small: only 16.7° for GaAs. As such, there is a very high degree of total internal reflection, and high divergence of the output light in the far-field, which corresponds to a coupling efficiency $\eta \sim 1\%$ to an objective lens even with high numerical aperture (NA).[6]

One approach to increase the coupling of light out of the semiconductor is to embed the QD in a high quality factor (Q) optical cavity. Engineering of the cavity allows improvements in the far-field profile and increase in the Purcell factor F_p,

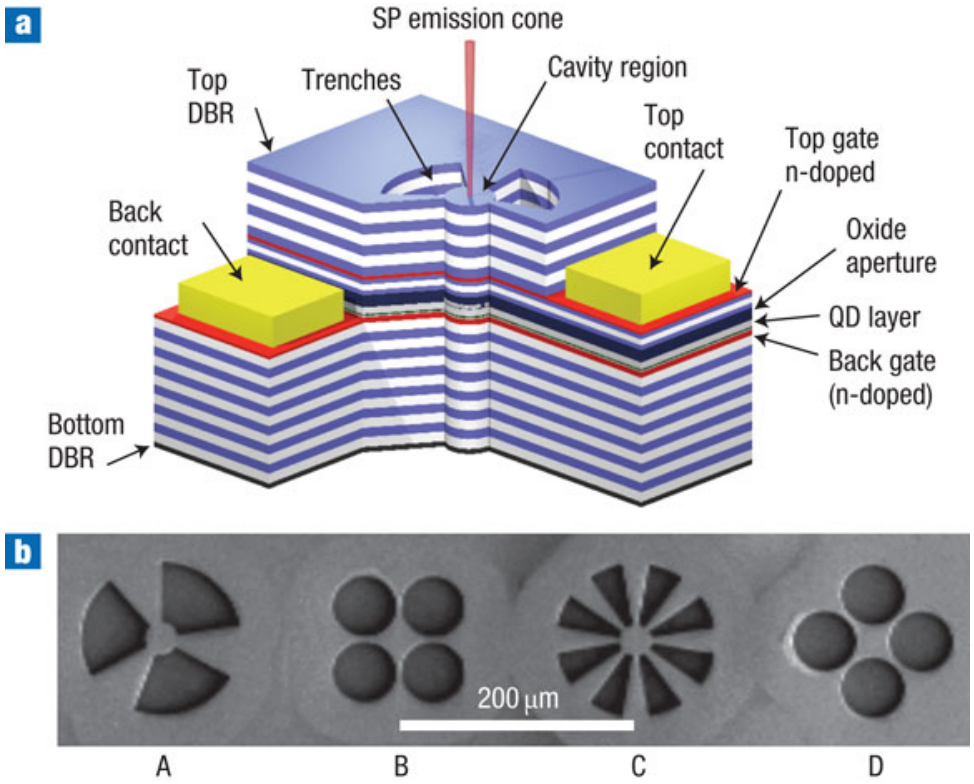

Figure 1.1: Example of a charge-tunable micropillar cavity for increased coupling out of the sample. (b) shows four different geometries of the top view, with the bars between the trenches providing electrical contacts to the central micropillar. Image taken from Ref. [7]

thus increasing both the emission rate of the QD and the coupling of the light out of the semiconductor and into the objective. This has been achieved with photonic crystal and micropillar cavities, obtaining $\eta \approx 44\%$ and a count rate at saturation of $\sim$ 1 MHz for photonic crystals[8]. Work with micropillars has reported η of up to 79% with a count rate of 700 kHz[9], and a maximum count rate of 4 MHz with $\eta \approx 38\%$ using the structure shown in Fig. 1.1 [7]. However, the problem with using these kinds of optical cavity is that the QD and cavity modes must spectrally and spatially overlap to effectively increase sample brightness. Given the distribution of self-assembled QD sizes, it is difficult to ensure that QD in an optical cavity will couple efficiently to the cavity mode. In addition, some applications of QDs such as generating entangled photon pairs via the biexciton cascade[10, 11] involve emission of photons with different energies which will not couple to a single cavity mode. One potential solution is to have one QD embedded in two coupled micropillars (a "photonic molecule") which exhibits splitting of the cavity modes[12]. While $\eta \approx 34\%$ for photon pairs has been demonstrated, this approach requires very challenging processing to produce a photonic molecule with only one QD in one of the individual pillars, and the diameter and centre-to-centre distance of the molecule to be accurately tuned to obtain the desired mode splitting.

A less spectrally specific approach is to use a broadband antenna, such as a

nanowire antenna. A nanowire acts as a waveguide: light emitted for a QD in a nanowire will be funnelled into the nanowire over a wide spectral range. In order to increase coupling in the direction of the collection optics, the base of the nanowire can be terminated with a mirror, and the top of the nanowire can be tapered to adiabatically expand the guided mode into a plane wave in free space. The angle of this taper allows the far field emission pattern to be tuned, specifically to reduce the divergence of the beam and facilitate more complete collection without the requirement for very high NA. Using a tapered nanowire antenna, $\eta \approx 0.72$ has been demonstrated with a count rate of 65 kHz.[13]

Nanowire antennae have a number of drawbacks, however. Firstly, the collection efficiency of a QD in a nanowire is highly dependent on the radial position of the QD in the wire. Ideally, the QD will be directly on the axis of the wire, but for self-assembled QDs without site control, this is not necessarily the case. Additionally, the QD is very sensitive to a fluctuating charge environment, leading to spectral fluctuations that inhomogeneously broaden the QD emission spectrum from the desired transform limit. Spectral fluctuations can be caused by surface charges and defects at interfaces, to which nanowires are particularly susceptible. On top of this, there is the problem of tuning the QDs. In bulk or cavity samples, it is simple to embed the QDs in a charge-tunable device structure that allows Stark shifting of excitonic states and deterministic charging to select particular states. In nanowires, it is much more challenging to fabricate such a structure due to the difficulty of making a "top contact" above the QD. Biaxial strain tuning has been demonstrated by attaching the nanowires to a gold mirror that makes the top electrode of a piezoelectric lead magnesium niobate lead titanate (PMN-PT) crystal.[14] This presents greater difficulties than in bulk, however, as there is significant strain relaxation along the length of the wire.

A relatively spectrally- and spatially-insensitive method to increase η is to use a broadband planar antenna. This is where a QD is embedded in a weak cavity in a bulk membrane sample. So far, experimental work using a circular dielectric grating (a "bullseye") on a membrane containing QDs demonstrated a collection efficiency of $\approx 10\%$,[15] but finite-difference time-domain (FDTD) simulations on planar cavity antennae have predicted a peak collection efficiency $\eta \sim 41\%$ with objective NA = 0.68 for modest Purcell factor enchancement $F_p \sim 1.25$, giving a power flux $\eta \times F_p > 50\%$ around 950 nm with spectral bandwidth ~ 110 nm.[6]. Samples used in this thesis designed by Ma (5th order planar cavity, Au back mirror, no DBR above QD layer, glass SIL) show collection efficiencies $\sim 25\%$ and saturation count rates up to 4 MHz (with significant charge noise: correcting for charge noise a count rate of ~ 7 MHz is expected).

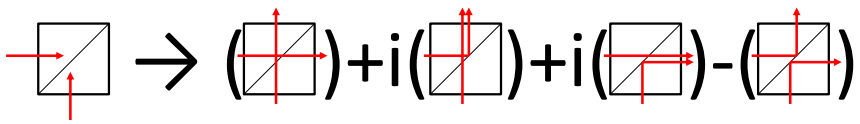

Figure 1.2: Diagram of the the four possible output states from two photons incident on different inputs to a 50:50 beamsplitter. If the photons are indistinguishable, the first and last "terms" will destructively interfere due to their opposite phases, leaving only the middle two terms: both photons will exit from the same output. Photon paths have been exaggerated for clarity; in reality, the photons must meet at the same spatial position on the beamsplitter for the Hong-Ou-Mandel effect to occur.

1.1.2 Single photon generation

QDs are good emitters of single photons. Fluorescence from QDs occurs when an electron and a hole in an exciton recombine, emitting a photon. When an exciton is created, either by resonant excitation or non-radiative relaxation after non-resonant excitation, the exciton exists on average for a finite lifetime T_1 before recombining. In order to emit another photon, another exciton must be established in the QD and recombine again. As such, the photons are "antibunched": there is a characteristic delay between consecutive photons emitted from a QD and two photons will never be emitted at the same time. While elastic scattering from a QD does not involve creation of electrons or holes, it still displays the same antibunched behaviour as fluorescent emission.

Measurement of the single photon character of a QD emission entails use of a Hanbury-Brown-Twiss interferometer (HBT). This consists of a 50:50 beamsplitter with photon detectors on each output channel, with a time-correlated single photon counting (TCSPC) system to measure time delays between counts on each channel. By sending the output from the QD to the input to the HBT, and measuring time delays between single counts on one channel and single counts on the other, it is possible to plot a histogram of time delays τ between consecutive photons on each channel. Since the photons from a QD are antibunched, the histogram will show a dip at zero delay. The histogram is a plot of the second-order correlation function $g^2(\tau)$ for the exciton emission, and the relevant measure of the single photon character of the exciton emission is given by $g^2(0)$. For a perfectly antibunched source, $g^2(0) = 0$.

1.1.3 Photon indistinguishability

Measurement of indistinguishability of photons is performed by taking advantage of the Hong-Ou-Mandel effect (HOM)[16]. When two photons are incident on the two inputs of a 50:50 beamsplitter, there are four possible output states, see Fig. 1.2. If the inputs are represented by a and b and the outputs by c and d, and state $|a_1 b_2\rangle$ represents photon 1 entering a and photon 2 entering b, the state evolution of the two photons becomes

$$|a_1 b_2\rangle \rightarrow 1/2\left(i\,|c_1 c_2\rangle + i\,|d_1 d_2\rangle + |c_1 d_2\rangle - |d_1 c_2\rangle\right) \tag{1.1}$$

In the case where the two photons are indistinguishable, the phase difference between the final two terms in Eq. 1.1 causes these states to destructively interfere, resulting in final state $|c_1 c_2\rangle + |d_1 d_2\rangle$: that is, both photons will exit the same output. Measuring coincidences from the two outputs will result in a dip at zero delay between the two output arms. A quantitative measure of indistinguishability is the visibility of the dip, which is measured by examining the HOM effect for a fully distinguishable case, and for the best indistinguishable case, and finding the normalised difference between the two. Since this is usually achieved by rotating the polarisation of one of the input photons, the parallel (indistinguishable) HOM signal is denoted by $g^2_{\parallel}(t)$, and the perpendicular (completely distinguishable) signal is $g^2_{\perp}(t)$. The visibility is then given by

$$V_{\mathrm{HOM}} = \frac{g^2_{\perp}(0) - g^2_{\parallel}(0)}{g^2_{\perp}(0)} \tag{1.2}$$

In addition to having the same energy and polarisation, the fundamental requirement for generation of indistinguishable photons from a single emitter is that the linewidth (defined hereafter as the full width at half maximum of the spectral peak – frequencies given in MHz are in units of ordinary frequency ν) of the emitted photons must be at or lower than the "transform limit". The linewidth of emitted photons depends on the lifetime of the transition T_1 via the uncertainty relation. In addition, there will be other effects that will further broaden the emission wavelength through non-radiative processes, such as interactions between the exciton and phonons in the crystal lattice. These non-radiative broadening effects, known as "pure dephasing" will have a characteristic lifetime T_2^*. The coherence time of the emitted photons T_2 is given by

$$\frac{1}{T_2} = \frac{1}{2T_1} + \frac{1}{T_2^*} \tag{1.3}$$

where the linewidth of the emitted photons will be $2/T_2$. Obtaining photons below the transform limit from QDs relies on elastic Rayleigh scattering from resonance

fluorescence, which is covered below.

At the transform limit, the photon coherence time is determined only by the radiative lifetime of the QD ($1/T_2^* = 0$) and so the linewidth from Eq. 1.3 is given by $2/T_2 = 1/T_1$. Any dephasing will broaden the spectrum, resulting in a drop in indistinguishability. The probability of measuring a coincidence from the HOM setup for two otherwise indistinguishable photons (i.e. same polarisation, energy, spatial position on the beamsplitter) is given by

$$g_{\parallel}^2(0) = 1 - \frac{T_2}{2T_1} \tag{1.4}$$

It is clear that at the transform limit the coincidence dip goes to zero. In the presence of pure dephasing $T_2 < 2T_1$, the coincidence dip becomes shallower, reducing the visibility of indistinguishability. An interpretation of this is that the two photon wavepackets have duration of $T_2/2$, so must meet on the beamsplitter within this time window: as T_2 decreases due to the introduction of pure dephasing, the probability of two photons meeting at the beamsplitter simultaneously (i.e. within T_1 of each other) but within this window and coalescing into the two-photon state given in Eq. 1.1 decreases.[17]

Resonance fluorescence (RF, Fig. 1.3) is a powerful tool for generation of highly coherent, narrow-linewidth photons. RF allows the direct excitation of the desired exciton state, in contrast to photoluminescence (PL) which involves generating an exciton in some excited state, then allowing the electron and hole to quickly relax to a ground exciton state before recombining and emitting a photon. PL typically suffers from additional inhomogeneous broadening due to decoherence or dephasing effects in the relaxation step, whereas RF does away with these particular effects.[18, 19]

The RF spectrum is made up of a highly coherent elastic part resulting from elastic Rayleigh scattering from the QD, whose energy and coherence properties, including linewidth, are given by those of the excitation laser, along with an inelastic part resulting from fluorescence, whose energy is given by the transition energy and whose linewidth is given by the radiative lifetime T_1, the coherence time T_2 and the Rabi frequency Ω, with power broadening occurring at high Ω. In addition $\Omega > \Omega_S$ where $\Omega_S = 1/\sqrt{T_1 T_2}$ results in the appearance of the Mollow triplet, further increasing the inelastic quality of the spectrum. As such, for indistinguishable photon generation, it is desirable to work in the low power regime, where the Mollow triplet and power broadening are absent. Work has been done by Weiler *et al.*[20], demonstrating indistinguishability visibility of up to 43% from the raw data, and 97% after deconvolution for photons from one of the Mollow sidebands, but this approach required spectral filtering of one of the sidebands, achieved via a double Michelson interferometer. Working below saturation in RF obviates the need for any spectral filtering.

Lowering Ω also results in the spectrum being made up of a higher proportion

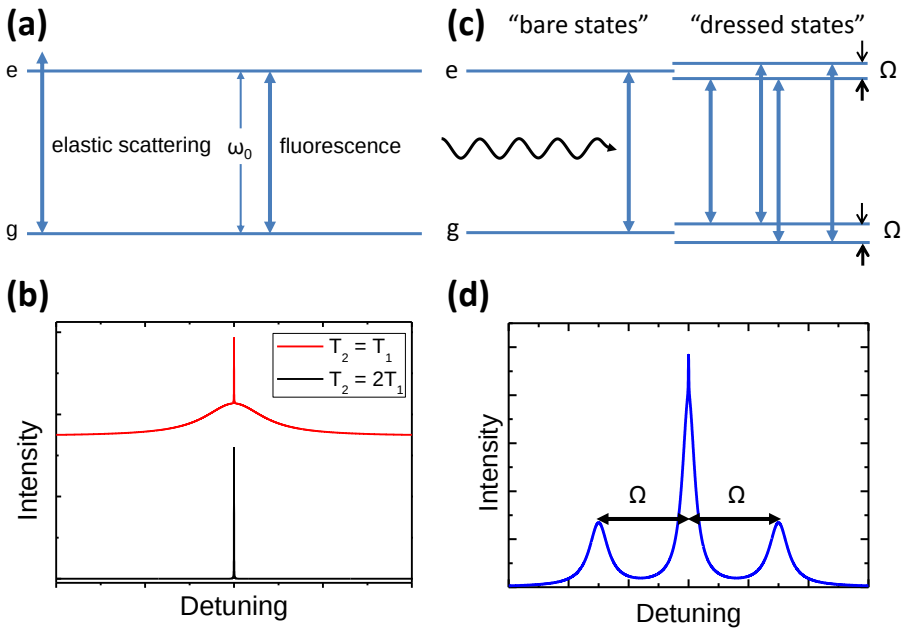

Figure 1.3: Level diagrams and spectra for resonance fluorescence. (a): At low power, the exciton acts as a two-level system, with fluorescence occurring at the exciton resonance due to absorption of a photon to form an exciton followed by recombination, and elastic Rayleigh scattering at the laser energy. (b): at the very low power limit, the form of the spectrum is determined by the decoherence time. With no pure dephasing $T_2 = 2T_1$, the spectrum is entirely composed of elastically scattered photons. With pure dephasing $T_2 < 2T_1$, there is a wide inelastic component to the spectrum with linewidth $2/T_2$. (c): At high power, the two-level system hybridises with the light field, resulting in dressed states split by the Rabi frequency Ω. The four transitions between these states give the characteristic Mollow triplet spectrum (d).

of highly coherent, narrow linewidth Rayleigh-scattered photons, further increasing indistinguishability. The proportion of the elastic Rayleigh-scattered photons in the total light emitted or scattered from the QD is given by

$$I_{\mathrm{e}}/I_{\mathrm{total}} = \frac{T_2}{2T_1}\frac{1}{1+\Omega^2 T_1 T_2} \tag{1.5}$$

which comes to a limit of $T_2/2T_1$ at the limit of low Ω.

Under continuous-wave resonant excitation, the state-of-the-art visibility seen is 0.60, with a value of 0.90 obtained by deconvolving with the instrument response of the detectors, using a post-selective scheme.[19] Without post-selection, pulsed excitation has yielded raw visibility of 0.91, with a corrected value obtained by taking into account experimental factors such as imperfect beamsplitter reflection and transmission of 0.97.[21]

1.1.4 Entanglement generation

Linear optical quantum computation

One method for generating entanglement from QDs is to simply use QDs as emitters and entangle the photons after emission using LOQC techniques. The HOM set-up described in the previous section generates spatially-entangled photons and can thus be done with any QD source of highly indistinguishable photons. As previously stated, He *et al*[21] demonstrated high visibility of 0.97 for photons from their QD samples. In addition, they also implemented a controlled-NOT (CNOT) gate with two consecutive photons, demonstrating an entanglement fidelity of 0.85 in the XX and ZZ bases, with a full process fidelity $0.70 \leq F_{proc} \leq 0.85$, well above the 0.5 threshold for entanglement.

A method similar to that used above to entangle separate spins can be used to entangle a single spin with a photon. An exciton in a QD can be used as a Λ-system: a three-level system where one excited state can decay to one of two possible ground states. This is achieved by using a magnetic field to split the single electron states of the electron-negatively charged exciton transition, resulting in two recombination paths with orthogonal photon polarisations. In this case, recombination of the exciton results in a entangled state of single electron spin states and polarisations, but with an energy difference $\hbar\Delta\omega$ between the photons providing which-path information, due to decoherence of the spin state after a measurement with a timing jitter $t > \Delta\omega$. This can be overcome by making photon detection measurements with timing jitter $t < \Delta\omega$, for example by using single photon detectors with very small timing jitter[22, 23] or using a frequency downconversion process pumped with short pulses to time gate the detection.[24] In these approaches, obtainable entanglement fidelity is limited by the time resolution of the detection, so the downconversion protocol with sub-10-ps time resolution reports a fidelity of 0.8[24], though with loss of

counts due to the gating of the detector, whereas the fast detector methods report fidelity of 0.59 with detector jitter of 48 ps[23] and fidelity of 0.67 with detector jitter of 60 ps[22].

A related method is to use spatially-separated QDs to emit indistinguishable photons and generate entanglement, either through entangling the photons as above, or entangling spins in the QDs: if two emitters emit indistinguishable photons and the "which-path" information of the photons emitted can be erased (i.e. it becomes unknown which emitter emitted a given photon), it is possible to entangle spins in the emitters. For example, by preparing both emitters in their excited state, after one photon is emitted, it is unknown which emitter emitted the photon, resulting in entanglement between the spins in the separated emitters.[25] Generation of indistinguishable photons from spatially-separated QDs has been demonstrated by strain tuning[26] and charge tuning[27] one QD into resonance with another QD on a separate sample (and, in the case of the charge-tuned sample, in a separate cryostat). Both cases show modest raw visibility in the CW post-selective case (0.47 for strain tuning, 0.33 for charge tuning), with the understanding that finite time resolution in the measurement is a major limiting factor. With infinite time resolution, they expect visibilities of 0.98 and 0.96 respectively. However, both experiments were carried out using non-resonant PL, and so the coherence time T_2 of the exciton states in the QD is also a limiting factor. Use of RF would both increase T_2 due to the elimination of any dephasing in the non-radiative relaxation to the exciton ground state, and also allow the emission of Rayleigh-scattered photons, which inherit their long coherence times from the excitation laser.

Quantum dot tuning

Another method of generating entangled photons from a QD is via the biexciton-exciton-vacuum cascade. The biexciton state XX consists of two electrons in the conduction band and two holes in the valence band bound together. This state first recombines to the neutral exciton state X^0, then to the vacuum, emitting two photons of different energy in the process. The spin state of the intermediate X^0 determines the polarisation of the photons emitted: if the X^0 are degenerate, the cascade emits non-degenerate circular polarisation-entangled photons. This is only the case for symmetric QDs, however: asymmetry of the QD in the plane results in a lifting of the degeneracy of the 2 X^0 due to the electron-hole exchange interaction, splitting the states by the fine-structure splitting (FSS) and resulting in the photons becoming linearly polarised along the asymmetry axes. If this FSS can be tuned to within the linewidth of the XX and X^0 emission, the cascade becomes a source of polarisation-entangled photons.

A number of tuning techniques have been attempted to tune the FSS, such as magnetic fields[28], vertical electric fields[29, 30], in-plane electric fields[31, 32, 33]

and strain[34, 35]. For approaches involving only one tuning technique, while some success has been achieved at cancelling FSS, in most cases [29, 34, 35], an anticrossing between the X^0 states occurs, suggesting a coherent coupling of the states, putting a lower bound on the FSS, as theoretically predicted in Ref. [36].

So far, the best candidate for reliable tuning of any QD to zero FSS is to combine two tuning techniques on one QD. This has been demonstrated both theoretically via two uniaxial strain fields[37, 38] and experimentally most notably by Trotta *et al.*[39, 40]. They demonstrate a peak maximally-entangled state fidelity of 0.88 with charge tunability: they show that Bell's inequality will be violated for their QD over a photon energy tuning range of 2 meV, with fidelity above the classical limit over a photon energy tuning range of 7 meV. The ability to spectrally tune an emitter of entangled photons is highly desirable.

A proposed method of entanglement generation, related to those given above using spatially-separated QDs, is to tune two QDs on one chip into resonance with each other.[41] This relies on the fact that self-assembled QDs have randomly distributed electronic and optical properties, specifically their photon energy tuning with strain.[42]

1.1.5 Telecommunication wavelength

So far, all of the results given are in the 950 nm regime. While QDs emitting at 950nm are more useful for research applications due to the high efficiency of Si detectors, they are not as useful for implementing real-world quantum communications due to the high rate of attenuation of light at 950nm through optical fibres. As such, QDs have been developed that emit in one of the optical telecommunication bands, either around 1300 or 1500nm (Fig. 1.4).

So far, very little work has been done on self-assembled QDs emitting at telecommunication wavelengths due to two major hurdles: the lack of efficient single photon detectors in this wavelength regime, which are vital for quantum communication; and difficulties in growing large enough QDs while maintaining a low enough QD density to address individual QDs. While Si single photon detectors have low efficiency at telecoms wavelengths, single photon avalanche photodiodes (APDs) can be fabricated using InGaAs, which has an absorption window from 900 to 1700 nm. Measurements made on low-density samples containing QDs emitting at 1300 nm using these InGaAs APDs have demonstrated antibunching of the photons emitted.[43] An alternative approach is to use a superconducting nanowire single photons detector (SNSPD). SNSPDs are potentially much faster than single photons APDs, with much lower time jitter and dark counts. Recently, a WSi SNSPD has demonstrated an efficiency $> 90\%$ in a window between 1520 and 1610 nm, with a dark count rate of ~ 1 Hz and timing jitter of ~ 150 ps.[44]. Experiments on QDs emitting at 1300 nm using NbN SNSPDs have also demonstrated antibunching.[45].

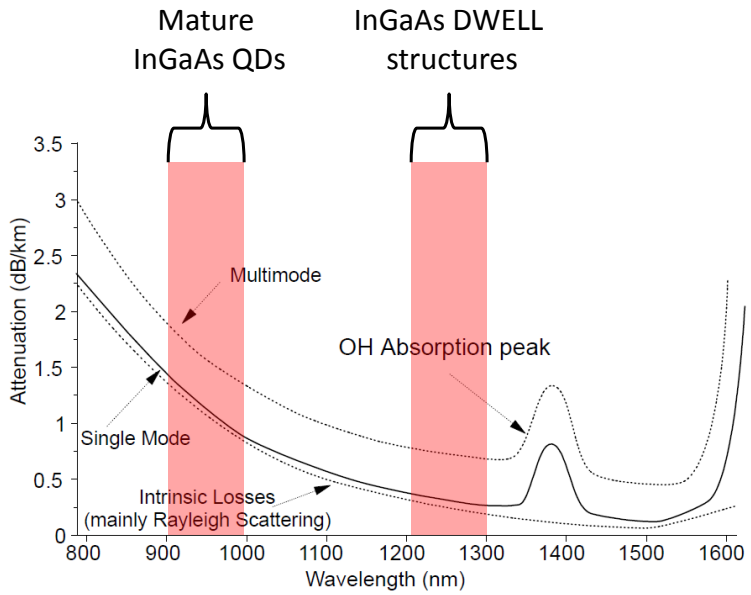

Figure 1.4: Plot of attenuation of light through optical fibres against wavelength. The wavelength range where mature QD optics research is carried out is not good for telecommunications purposes due to the increased signal attenuation over long distances. By comparison, the DWELL QDs used here emit in the 1300nm telecommunication band, making them good candidates as sources for long-range fibre-carried quantum communications.

Fabrication of low-density, long wavelength QD samples can be achieved by reducing the InAs deposition rate, allowing QDs to grow larger without forming a larger number of QDs, and to introduce a strain-relaxing layer of InGaAs to allow larger QDs to form without dislocations.[46, 47, 48]

1.2 Self-assembled quantum dots

One approach to fabricate semiconductor QDs is to use the lattice mismatch between the QD material and substrate to allow them to form on their own, producing so-called "self-assembled" QDs, via the Stranski-Krastanov process as shown in Fig. 1.5. InAs is deposited by molecular beam epitaxy (MBE) on the [001] surface of a GaAs substrate. InAs and GaAs have lattice constants that vary by 6.8% (6.06 and 5.65 Årespectively), so firstly a strained monolayer (the wetting layer) of InAs forms on the surface of the GaAs. As more InAs is deposited, the strain relaxes through the formation of InAs islands on the wetting layer. These islands will appear when approximately 1–2 monolayers have been deposited.[49]

If these islands are capped with GaAs to complete the vertical heterostructure and protect them form surface charges, their size will correspond to an emission wavelength in excess of 1000nm, where Si detectors start to lose efficiency.[49] Ideally,

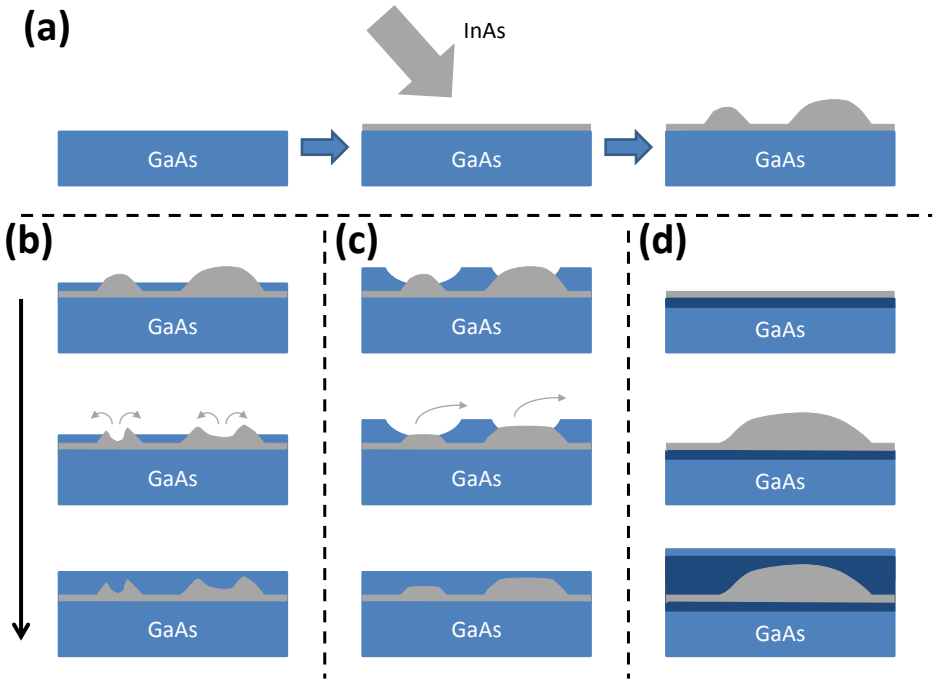

Figure 1.5: Sketch of QD growth via MBE. (a) InAs is deposited on a GaAs substrate. Once a particular thickness has been reached (approx 1-2 monolayers), the strain relaxes coherently via formation of InAs "islands". (b) for the production of partially-capped islands, the islands are capped with a thin layer of GaAs , and then annealed at the growth temperature. This causes redistribution of InAs into a "volcano" shape, and diffusion of GaAs into the island, reducing its effective dimensions. The island is then fully capped. (c) for the production of In-flush QDs, the islands are capped with a thicker layer of GaAs. The In at the top of the island migrates away from the island to the capping layer surface to minimize local strains, and the GaAs covers the island. The In on the surface is flushed away during the annealing step. (d) dots-in-a-well are grown slightly differently: an InGaAs layer (dark blue) is deposited on the GaAs substrate, onto which InAs is deposited. The InGaAs reduces the strain slightly, allowing the islands to become larger before crystal defects form. The island is then capped with InGaAs, then GaAs.

to take advantage of the high efficiency of Si detectors, the emission should be in the 950nm range. In order to do this, the QDs must be made smaller to increase the effect of confinement and thus raise the energy of emission. There are two methods of producing the required QD size I will describe: the "partially-capped island" (PCI) process and the "In-flush" process.

1.2.1 Partially-capped islands

PCI QDs are produced (Fig. 1.5 (b)), as their name suggests, by partially capping the InAs islands with a layer of GaAs smaller than their height, prior to annealing the QD at high temperature with an As_2 flux. This annealing has two effects: firstly, the In in the QD diffuses out into the surrounding GaAs, effectively reducing the size of the InAs island (and introducing an admixture of Ga into the InAs). Secondly, the exposed top of the island is partially eroded, resulting in a "volcano" shape and reducing the height of the QD (in cases where a very thin capping layer of GaAs is used, this process produces InAs "rings").[50] The QDs are then fully capped with GaAs. The PCI QD samples used later in this thesis were produced by B. D. Gerardot in the group of P. M. Petroff at UCSB in Santa Barbara, California, USA.

1.2.2 In-flush quantum dots

Much like PCI QDs, In-flush QDs are produced by almost completely capping the InAs island with GaAs (Fig. 1.5 (c)). In this situation, the lattice mismatch between the InAs and GaAs and the resultant strain on the In in the island mean that it is energetically favourable for the exposed "dome" of InAs to migrate on to the top of the GaAs to produce a partial wetting layer, leaving a truncated "disk" of InAs. This then allows the GaAs to overgrow the InAs disk, completely capping the InAs QD and leaving the partial InAs wetting layer on top. This is then flushed away during an annealing step at 610°C, which also serves to diffuse In and Ga, again reducing the effective size of the QD.[51] The QD can then be capped with a thicker layer of GaAs. The In-flush samples used later in this thesis were produced by Edmund Clarke at the National Centre for III-V Technologies in Sheffield, UK.

1.2.3 Quantum dots-in-a-well

As noted above, it is desirable to have light sources emitting at one of the telecommunications bands. In order to produce QDs emitting at this wavelength, they must be allowed to grow to a larger size without the QD density becoming too high to resolve single QDs, which is the usual problem when trying to increase QD size by simply depositing more InAs.

One way of doing this is to grow the QD in a strain-reducing layer, i.e. one where the lattice constant is closer to that of the QD. A thin layer of InGaAs is grown

on a GaAs substrate, onto which InAs islands are grown by the Stranski-Krastanov process (Fig. 1.5 (d)). The QDs are then capped with InGaAs followed by GaAs. The reduced band gap of the thin InGaAs layer compared to the GaAs means that the InAs QDs are embedded in an InGaAs quantum well, so these QDs are known as dot-in-a-well or "DWELL" QDs. [46, 47]

1.3 Properties of self-assembled QDs

As the growth process for self-assembled QDs is by nature non-deterministic, the major feature of a wafer containing self-assembled QDs is that no two QDs will be the same. Due to the randomness in the shape, size and In/Ga composition of these QDs, many of their properties (such as emission wavelength) will differ from QD to QD[41, 42]. While it is possible to affect the distribution of QD properties during the growth process, such as depositing less InAs to attempt to reduce overall dot size and thus dot wavelength, it is impossible to grow a self-assembled QD "to specification", i.e. to produce a QD that will emit at exactly 950nm.

The energies of the excitonic states in a QD depend on the quantisation the density of states for electrons and holes in the QD. As stated above, a self-assembled QD is a semiconductor heterostructure made up of a region of low band gap (InGaAs) embedded in a higher band gap material (GaAs). Due to the randomness of the QD composition, however, it is not known what the band gap of the QD will be, as it will be affected by the relative concentration of In to Ga. In addition, the actual charge confinement potentials are also determined by the size and shape of the QD, which varies from QD to QD. In general, though, the potential in self-assembled QDs is approximately parabolic, meaning that the QD potential can be modelled as a harmonic oscillator. This results in a 'ladder' of discrete electron and hole energies.

1.3.1 Excitons and selection rules

While single particle states exist in QDs, the major source of photons is scattering from or recombination of excitonic states. An exciton is a bound complex of electrons in the conduction band and holes in the valence band of a QD. The simplest of these is the neutral exciton X^0, consisting of one conduction electron and one hole. The single particles exist in the lowest energies in their bands, and there are four different spin states that the X^0 can exist in. The electron has spin $\pm 1/2$, and the hole (assumed to be a pure heavy hole in the ground state of a self-assembled QD) has spin $\pm 3/2$. As shown in Fig. 1.6 (a) and (b), there are two states with spin quantum number $M_S = \pm 1$ which can radiatively recombine via emission of a photon of spin ± 1 (the "bright" exciton states), and two states with spin $M_S = \pm 2$ spin whose radiative recombination is forbidden (the "dark" excitons). In addition,

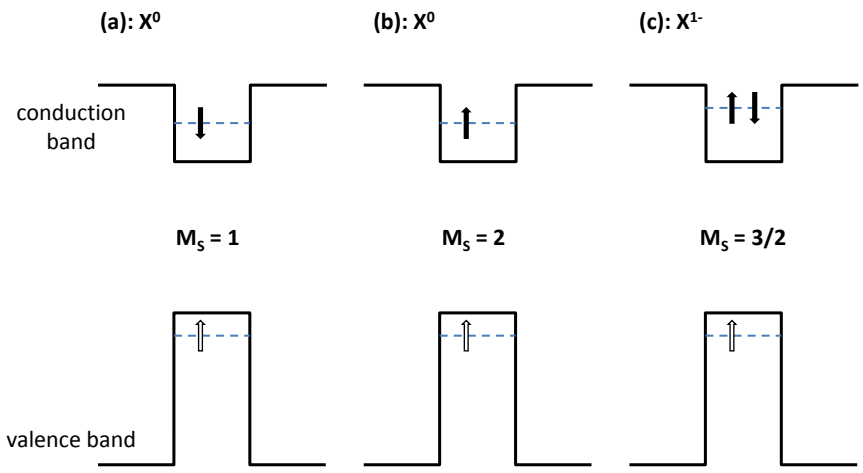

Figure 1.6: Band diagram of electron and holes in the QD for the "spin-up" versions of (a) bright X^0, (b) dark X^0 and (c) X^{1-}. Equivalent states exist by reversing the hole (open arrow) and electron (filled arrow) spins. The $M_S = \pm 2$ exciton (b) cannot recombine to the vacuum state by emission of a photon of spin ± 1, hence it is "dark". In the X^{1-}, the Coulomb interaction between the two electrons shifts the energy level of the electrons to a higher value, resulting in an increased photon energy from recombination for X^{1-}.

the two bright excitons will be degenerate in perfectly symmetric QDs (Fig. 1.7 (a)), but shape asymmetry and localised strains and defects in the QD's environment will break this symmetry, resulting in a splitting between the X^0 spin states, lifting the degeneracy. Because of this, the X^0 states couple to photons with linear polarisation aligned to the QD axis, and the photon energies are split by the fine-structure splitting (FSS, see Fig. 1.7 (b)).

The other major exciton state relevant to this thesis is the negatively-charged exciton or "trion" X^{1-} (Fig. 1.6 (c)). This consists of two electrons in the conduction band ground state and a single hole. Due to the Pauli exclusion principle, the two electrons must have opposite spins, so the spin state of the X^{1-} is given entirely by the hole, which is $\pm 3/2$ (again, assuming a pure heavy hole). This exciton recombines to a single electron ground state, so the X^{1-} recombination forms a 4-level system. The selection rules of this system rely heavily on the spin orientation of the electron. A heavy hole's spin in a self-assembled QD will be aligned in the growth direction because it is the $M_S = \pm 3/2$ state of the hole, but the electron is sensitive to external stimuli such as magnetic fields. To illustrate the selection rules for X^{1-}, it is worth considering two cases: one where there is an applied external magnetic field in the growth direction (the "Faraday geometry"), and one where there is an external magnetic field in the QD plane (the "Voigt geometry"). These cases are shown in Fig. 1.8.

Faraday geometry: In this case (Fig. 1.8 (a)), the electron spin aligns to the mag-

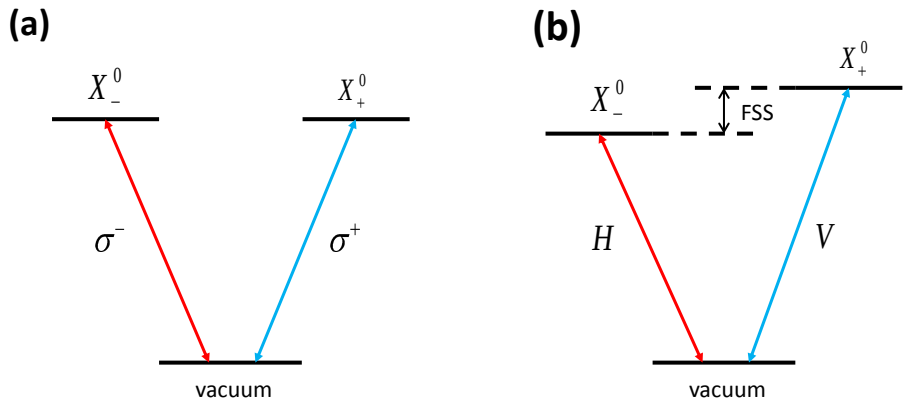

Figure 1.7: Diagram of energy levels for X^0 both (a) with and (b) without perfect symmetry.

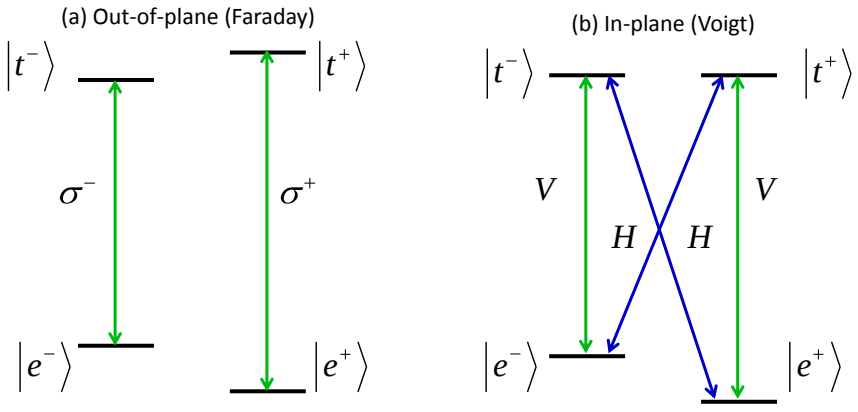

Figure 1.8: Diagram of levels and selection rules for X^{1-} in (a) Faraday and (b) Voigt geometry. $\langle t^{\pm}|$ is the $\pm 3/2$ spin X^{1-} state, and $\langle e^{\pm}|$ is the $\pm 1/2$ spin single electron state. $\sigma^{\pm}$ are the two opposite circularly polarisations, and H and V are the horizontal and vertical linear polarisations. The exciton and ground single electron states are split by the magnetic field due to the Zeeman effect.

netic field in the growth axis, and the selection rules allow only two transitions: the $\langle t^{\pm}| \rightarrow \langle e^{\pm}|$. In the ideal case (no light hole-heavy hole mixing, no magnetic field fluctuations), the X^{1-} emits only circularly polarised light from the two allowed transitions.

Voigt geometry: In this case (Fig. 1.8 (b)), the electron spin is aligned to the external magnetic field in the QD plane. The selection rules allow all 4 transitions between levels: the "vertical" (V) and "diagonal" (H) transitions emit orthogonal linearly polarised light. This geometry allows for a variety of processes, such as inelastic Raman scattering and optical spin pumping (OSP).

1.3.2 Exciton tuning

While excitonic energies are determined by the confinement potentials of electrons and holes, and thus by the size, shape and composition of the QD, there are techniques for tuning these energies via external stimuli. The methods I will describe are the techniques used in this thesis: charge tuning via the quantum confined Stark effect, magnetic field tuning, and uniaxial strain tuning.

Charge tuning

Charge tuning is performed by applying an electric field across the QD; in this thesis, the field is applied in the growth direction. This is facilitated by embedding the QD in an n-i-Schottky device structure[52], described in Chapter 2. The exciton, being made up of electrons and holes, is polarisable in that the electrons and holes can be pulled apart by an applied electric field. In addition, the inhomogeneity of the In composition in the QD results in the electron and hole wavefunctions being spatially separated, with a strong separation in the growth direction. This results in a large permanent dipole moment.[53] The quantum-confined Stark effect results in a shift to the emission energy of an exciton with applied electric field F:

$$E_X(F) = E_0 - pF + \beta F^2 \tag{1.6}$$

where E_X is the photon energy, E_0 is the photon energy at zero applied field, p is the permanent dipole moment and β is the polarisability of the exciton.

Magnetic field tuning

The application of a magnetic field to a QD results in a spin splitting due to the Zeeman effect, with an overall diamagnetic shift to the split levels. This shift for applied field B is given by:

$$E_X(B) = E_0 \pm g_X \mu_B B + \alpha B^2 \tag{1.7}$$

where E_0 is the photon energy at zero applied magnetic field, g_X is the Landé g-factor of the exciton (given by $g_e + g_h$, the sum of the g-factors for the electron and hole), μ_B is the Bohr magneton, and α is the diamagnetic coefficient.

Since the ground state after recombination of the X^0 is the vacuum, the Zeeman effect only affects the X^0 states, splitting the two orthogonally polarised components. As the ground state for the X^{1-} transition is the single electron state, the Zeeman effect causes a splitting of both the excited and ground states of the transition. The electron level is split according to the strength of the magnetic field and its g-factor as the Zeeman term of Eq. 1.7 regardless of the field's orientation. As the X^{1-} spin is determined entirely by that of the hole, and the pure heavy hole state has spin locked to the growth direction, the X^{1-} state is only split when the field is applied in the Faraday geometry (so that the field is parallel to the hole spin – see Fig. 1.8 (a)). If the field is applied in the Voigt geometry, the heavy hole spins are not split by the field but the electron spins are (Fig. 1.8 (b)). In reality, there will be a small amount of mixing between the $M_S = \pm 3/2$ heavy hole and $M_S = \pm 1/2$ light hole states, predominately due to lattice strain[54], which weakly allows the diagonal transition in the Faraday geometry, and introduces a Zeeman splitting of the X^{1-} state in the Voigt geometry.

Uniaxial strain tuning

Applying uniaxial strain to a QD shifts the energies of the conduction and valence bands, depending on the deformation potentials of the semiconductor. The influence of strain on holes in a self-assembled QD can be modelled via the Bir-Pikus Hamiltonian, whereas conduction band electrons are governed entirely by the effect of hydrostatic strain. Since Coulomb effects are not strongly affected by applied strain, the effect of uniaxial strain on an exciton energy is determined by the effect on the individual particles:[55]

$$\frac{dE_v}{dp} \approx -a_v(S_{11} + 2S_{12}) - \frac{1}{2}b_v(S_{11} - S_{12}) \tag{1.8}$$

$$\frac{dE_c}{dp} = -a_c(S_{11} + 2S_{12}) \tag{1.9}$$

$$\frac{dE_{X^0}}{dp} = \frac{dE_c}{dp} - \frac{dE_v}{dp} \tag{1.10}$$

where $dE_{v(c)}/dp$ is the rate of change of valence band (conduction band) energy with stress p, $a_{v(c)}$ is the hydrostatic deformation potential of the valence (conduction) band, b_v is the biaxial deformation potential for the valence band, and S_{ij} is the i, j component of the compliance matrix. The deformation potentials and compliance coefficients are known for bulk InAs and GaAs, but these values for self-assembled QDs will change from QD to QD.

1.4 Noise sources in QDs

As noted above, dephasing sources in QDs have a detrimental effect on the properties of the photons emitted, specifically the indistinguishability and coherence of the photons emitted. Dephasing is generally a result of noise sources in the QD. There are three major sources of noise in QDs: phonon interactions, which I will give a brief account of, and charge noise and nuclear spin fluctuations, which I will cover in more detail, as it is these sources of noise that I will investigate further in this thesis.

1.4.1 Phonon interactions

Phonons are quasiparticles resulting from the quantisation of vibrations in a crystal lattice. Excitonic states in a QD can interact with phonons through virtual transitions which do not change the exciton population: transitions from a given state back to that state. These contribute to the decoherence of the exciton but do not involve recombination of the electron or hole, so this effect is pure dephasing. Exciton states can also recombine via emission of both photons and phonons. These effects combined result in a broadening of the "zero phonon line" (ZPL), or the spectral line arising from exciton recombination with no emission of phonons, as the interaction with phonons in the lattice results in small random perturbations to the exciton energy. Additionally, the possibility of exciton recombination involving emission of both photons and phonons results in a broad "phonon sideband" in emission redshifted from the ZPL. The effect of phonons is highly dependent on temperature, with increased temperature increasing the linewidth of the ZPL and decreasing the relative intensity of the ZPL to the phonon sideband. As such, QD experiments are performed at cryogenic temperatures (< 5 K) to reduce the effect of phonon dephasing.

1.4.2 Charge noise

Charge noise in QDs is a result of a fluctuating charge environment. Crystal defects or atomic impurities in a semiconductor crystal can trap charges, and a large number of defects charging and uncharging results in a fluctuating electric field in the crystal. When a QD is present in this fluctuating field, the exciton states are subject to a Stark shift, as above. This causes the spectral peak to jump around in energy – this is known as "spectral diffusion". The field changes with a timescale of $\sim 10^0$ to 10^{-3} s, so for integration times of ~ 1 s, the spectral peak will be broadened.[56, 57]

In addition, charge noise provides particular problems for resonance fluorescence. As the exciton line is fluctuating in energy, it has a fluctuating detuning from the excitation laser. This detuning causes "blinking" of the RF signal as the exciton moves in and out of resonance with the laser. This reduces the overall count rate from

the QD, including the component arising from Rayleigh scattering, whose linewidth is not affected by spectral diffusion.

1.4.3 Nuclear spin noise

The nuclei in InGaAs all have non-zero spin: 9/2 for In and 3/2 for Ga and As. As such, they will interact with single electron and hole spins in a QD via the hyperfine interaction. The dominant interaction here is the contact hyperfine interaction between nuclear spins and electron spins. Hole states are predominantly made up of p-shell electron states in the valence band, which have a vanishing wavefunction at the nuclei in the crystal lattice, so their contact hyperfine interaction is reduced to zero. Both electron and holes have a dipole-dipole interaction with the nuclei, but this is around 10 times smaller than the contact hyperfine interaction, so is negligible when considering the electron spin.[58]

Due to the extent of the electron wavefunction in the QD, the electron spin interacts with around 10^5 nuclear spins. This is too large a number to consider them individually, but not large enough for their contributions to completely cancel out. As such, the effect of nuclear spins is modelled as a magnetic field called the Overhauser field. This field fluctuates over timescales $\sim 10^{-4}$ s, but the electron spin interacts much faster than the fluctuations, so the electron sees an effective Overhauser field on the order of 30 mT in a random direction. The precession of the electron spin around the field dephases the electron spin state, resulting in an decreased electron coherence time T_2, which reduces the electron spin's use as a spin qubit for quantum information processing. In addition, dephasing of the electron spin affects the linewidth of any Raman scattered photons from the exciton: the presence of an in-plane component of the Overhauser field splits the single electron state and allows Raman scattering from the X^{1-}. The photon coherence properties are dependent on the coherence of the single electron state.

1.5 Summary

The motivation behind using QDs as light sources in quantum technologies has been explained, with focus given to the potential for generation of indistinguishable and entangled photons. The state of the art for bright indistinguishable and entangled photon emission has been shown. Some detail into the different types of annealed QDs (PCI, In-flush, DWELL) has been given, along with the processes required to produce these. The physics of single particles and their bound states, excitons, has been covered, and methods of tuning their optical properties have been described. Three noise sources have been identified and described, and two of these, charge noise and nuclear spin noise, will be investigated further later in this thesis.

1.6 References

[1] Kok, P. *et al.* Linear optical quantum computing with photonic qubits. *Rev. Mod. Phys.* **79**, 135 (2007).

[2] Briegel, H.-J., Dr, W., Cirac, J. I. & Zoller, P. Quantum Repeaters: The Role of Imperfect Local Operations in Quantum Communication. *Phys. Rev. Lett.* **81**, 5932 (1998).

[3] Sangouard, N., Simon, C., de Riedmatten, H. & Gisin, N. Quantum repeaters based on atomic ensembles and linear optics. *Rev. Mod. Phys.* **83**, 33 (2011).

[4] Young, R. J. *et al.* Single electron-spin memory with a semiconductor quantum dot. *New J. Phys.* **9**, 365 (2007).

[5] Simon, C. *et al.* Quantum memories: A review based on the European integrated project Qubit Applications (QAP). *The European Physical Journal D* **58**, 1 (2010).

[6] Ma, Y., Kremer, P. E. & Gerardot, B. D. Efficient photon extraction from a quantum dot in a broad-band planar cavity antenna. *Journal of Applied Physics* **115**, 023106 (2014).

[7] Strauf, S. *et al.* High-frequency single-photon source with polarization control. *Nat Photon* **1**, 704 (2007).

[8] Madsen, K. H. *et al.* Efficient out-coupling of high-purity single photons from a coherent quantum dot in a photonic-crystal cavity. *Phys. Rev. B* **90**, 155303 (2014).

[9] Gazzano, O. *et al.* Entangling Quantum-Logic Gate Operated with an Ultrabright Semiconductor Single-Photon Source. *Phys. Rev. Lett.* **110**, 250501 (2013).

[10] Akopian, N. *et al.* Entangled Photon Pairs from Semiconductor Quantum Dots. *Phys. Rev. Lett.* **96**, 130501 (2006).

[11] Hafenbrak, R. *et al.* Triggered polarization-entangled photon pairs from a single quantum dot up to 30 K. *New J. Phys.* **9**, 315 (2007).

[12] Dousse, A. *et al.* Ultrabright source of entangled photon pairs. *Nature* **466**, 217 (2010).

[13] Claudon, J. *et al.* A highly efficient single-photon source based on a quantum dot in a photonic nanowire. *Nat Photon* **4**, 174 (2010).

[14] Kremer, P. E. *et al.* Strain-tunable quantum dot embedded in a nanowire antenna. *Phys. Rev. B* **90**, 201408 (2014).

[15] Davano, M. *et al.* Efficient quantum dot single photon extraction into an optical fiber using a nanophotonic directional coupler. *Applied Physics Letters* **99**, 121101 (2011).

[16] Hong, C. K., Ou, Z. Y. & Mandel, L. Measurement of subpicosecond time intervals between two photons by interference. *Phys. Rev. Lett.* **59**, 2044 (1987).

[17] Bylander, J., Robert-Philip, I. & Abram, I. Interference and correlation of two independent photons. *Eur. Phys. J. D* **22**, 295 (2003).

[18] Santori, C., Fattal, D., Vukovi, J., Solomon, G. S. & Yamamoto, Y. Indistinguishable photons from a single-photon device. *Nature* **419**, 594 (2002).

[19] Ates, S. *et al.* Post-Selected Indistinguishable Photons from the Resonance Fluorescence of a Single Quantum Dot in a Microcavity. *Phys. Rev. Lett.* **103**, 167402 (2009).

[20] Weiler, S., Stojanovic, D., Ulrich, S. M., Jetter, M. & Michler, P. Postselected indistinguishable single-photon emission from the Mollow triplet sidebands of a resonantly excited quantum dot. *Phys. Rev. B* **87**, 241302 (2013).

[21] He, Y.-M. *et al.* On-demand semiconductor single-photon source with near-unity indistinguishability. *Nat Nano* **8**, 213 (2013).

[22] Gao, W. B., Fallahi, P., Togan, E., Miguel-Sanchez, J. & Imamoglu, A. Observation of entanglement between a quantum dot spin and a single photon. *Nature* **491**, 426 (2012).

[23] Schaibley, J. R. *et al.* Demonstration of Quantum Entanglement between a Single Electron Spin Confined to an InAs Quantum Dot and a Photon. *Phys. Rev. Lett.* **110**, 167401 (2013).

[24] De Greve, K. *et al.* Quantum-dot spin-photon entanglement via frequency downconversion to telecom wavelength. *Nature* **491**, 421 (2012).

[25] Duan, L.-M., Lukin, M. D., Cirac, J. I. & Zoller, P. Long-distance quantum communication with atomic ensembles and linear optics. *Nature* **414**, 413 (2001).

[26] Flagg, E. B. *et al.* Interference of Single Photons from Two Separate Semiconductor Quantum Dots. *Phys. Rev. Lett.* **104**, 137401 (2010).

[27] Patel, R. B. *et al.* Two-photon interference of the emission from electrically tunable remote quantum dots. *Nat Photon* **4**, 632 (2010).

[28] Hudson, A. J. *et al.* Coherence of an Entangled Exciton-Photon State. *Phys. Rev. Lett.* **99**, 266802 (2007).

[29] Bennett, A. J. *et al.* Electric-field-induced coherent coupling of the exciton states in a single quantum dot. *Nat Phys* **6**, 947 (2010).

[30] Marcet, S., Ohtani, K. & Ohno, H. Vertical electric field tuning of the exciton fine structure splitting and photon correlation measurements of GaAs quantum dot. *Applied Physics Letters* **96**, 101117 (2010).

[31] Gerardot, B. D. *et al.* Manipulating exciton fine structure in quantum dots with a lateral electric field. *Applied Physics Letters* **90**, 041101 (2007).

[32] Kowalik, K. *et al.* Monitoring electrically driven cancellation of exciton fine structure in a semiconductor quantum dot by optical orientation. *Applied Physics Letters* **91**, 183104 (2007).

[33] Vogel, M. M. *et al.* Influence of lateral electric fields on multiexcitonic transitions and fine structure of single quantum dots. *Applied Physics Letters* **91**, 051904 (2007).

[34] Plumhof, J. D. *et al.* Strain-induced anticrossing of bright exciton levels in single self-assembled GaAs/$Al_xGa_{1-x}As$ and $In_xGa_{1-x}As$/GaAs quantum dots. *Phys. Rev. B* **83**, 121302 (2011).

[35] Sapienza, L. *et al.* Exciton fine-structure splitting of telecom-wavelength single quantum dots: Statistics and external strain tuning. *Phys. Rev. B* **88**, 155330 (2013).

[36] Singh, R. & Bester, G. Lower Bound for the Excitonic Fine Structure Splitting in Self-Assembled Quantum Dots. *Phys. Rev. Lett.* **104**, 196803 (2010).

[37] Wang, J., Gong, M., Guo, G.-C. & He, L. Eliminating the fine structure splitting of excitons in self-assembled InAs/GaAs quantum dots via combined stresses. *Applied Physics Letters* **101**, 063114 (2012).

[38] Trotta, R., Martn-Snchez, J., Ortix, C. & Rastelli, A. Energy-tunable sources of entangled photons: a realistic concept for solid-state quantum relays. *arXiv:1412.5954 [cond-mat]* (2014). ArXiv: 1412.5954.

[39] Trotta, R. *et al.* Universal Recovery of the Energy-Level Degeneracy of Bright Excitons in InGaAs Quantum Dots without a Structure Symmetry. *Phys. Rev. Lett.* **109**, 147401 (2012).

[40] Trotta, R., Wildmann, J. S., Zallo, E., Schmidt, O. G. & Rastelli, A. Highly Entangled Photons from Hybrid Piezoelectric-Semiconductor Quantum Dot Devices. *Nano Lett.* **14**, 3439 (2014).

[41] Kuklewicz, C. E., Malein, R. N. E., Petroff, P. M. & Gerardot, B. D. Electro-Elastic Tuning of Single Particles in Individual Self-Assembled Quantum Dots. *Nano Lett.* **12**, 3761 (2012).

[42] Jöns, K. D. *et al.* Dependence of the Redshifted and Blueshifted Photoluminescence Spectra of Single $In_xGa_{1-x}As$/GaAs Quantum Dots on the Applied Uniaxial Stress. *Phys. Rev. Lett.* **107**, 217402 (2011).

[43] Zinoni, C. *et al.* Time-resolved and antibunching experiments on single quantum dots at 1300nm. *Applied Physics Letters* **88**, 131102 (2006).

[44] Marsili, F. *et al.* Detecting single infrared photons with 93% system efficiency. *Nat Photon* **7**, 210 (2013).

[45] Zinoni, C. *et al.* Single-photon experiments at telecommunication wavelengths using nanowire superconducting detectors. *Applied Physics Letters* **91**, 031106 (2007).

[46] Nishi, K., Saito, H., Sugou, S. & Lee, J.-S. A narrow photoluminescence linewidth of 21 meV at 1.35 μm from strain-reduced InAs quantum dots covered by $In_{0.2}Ga_{0.8}As$ grown on GaAs substrates. *Applied Physics Letters* **74**, 1111 (1999).

[47] Liu, H. Y. *et al.* Optimizing the growth of 1.3 m InAs/InGaAs dots-in-a-well structure. *Journal of Applied Physics* **93**, 2931 (2003).

[48] Alloing, B. *et al.* Growth and characterization of single quantum dots emitting at 1300 nm. *Applied Physics Letters* **86**, 101908 (2005).

[49] Leonard, D., Krishnamurthy, M., Reaves, C. M., Denbaars, S. P. & Petroff, P. M. Direct formation of quantumsized dots from uniform coherent islands of InGaAs on GaAs surfaces. *Applied Physics Letters* **63**, 3203 (1993).

[50] Offermans, P. *et al.* Atomic-scale structure and formation of self-assembled In(Ga)As quantum rings. *Physica E: Low-dimensional Systems and Nanostructures* **32**, 41 (2006).

[51] Wasilewski, Z., Fafard, S. & McCaffrey, J. Size and shape engineering of vertically stacked self-assembled quantum dots. *Journal of Crystal Growth* **201-202**, 1131 (1999).

[52] Warburton, R. J. *et al.* Optical emission from a charge-tunable quantum ring. *Nature* **405**, 926 (2000).

[53] Warburton, R. J. *et al.* Giant permanent dipole moments of excitons in semiconductor nanostructures. *Phys. Rev. B* **65**, 113303 (2002).

[54] Belhadj, T. *et al.* Impact of heavy hole-light hole coupling on optical selection rules in GaAs quantum dots. *Applied Physics Letters* **97**, 051111 (2010).

[55] Wang, J., Guo, G.-C. & He, L. Theory of strain tuning exction coupling in self-assembled InAs/GaAs quantum dots. *arXiv:1401.2695 [cond-mat]* (2014). ArXiv: 1401.2695.

[56] Kuhlmann, A. V. *et al.* Charge noise and spin noise in a semiconductor quantum device. *Nat Phys* **9**, 570 (2013).

[57] Matthiesen, C., Stanley, M. J., Hugues, M., Clarke, E. & Atatre, M. Full counting statistics of quantum dot resonance fluorescence. *Sci. Rep.* **4**, 4911 (2014).

[58] Urbaszek, B. *et al.* Nuclear spin physics in quantum dots: An optical investigation. *Rev. Mod. Phys.* **85**, 79 (2013).

Chapter 2

Experimental set-up

2.1 Introduction

In this chapter I will describe the set-up for optical frequency- and time-domain spectroscopy with both resonant and non-resonant excitation. I will give details of the samples used in the various experiments, then cover the optics used to perform specific measurements. The system used is relatively "modular": the collection optics from the QD are coupled to a single mode fibre, which can then be plugged into a number of analysis optics assemblies. This allows a number of different types of measurement to be made on a single QD without the need for re-alignment of the excitation and collection optics, because once the microscope it set up, it is very stable if untouched over a timescale of weeks to months.

2.2 Quantum dot samples

While a number of different samples are used in various experiments, they all share some general characteristics. All samples contain one layer of QDs embedded in a GaAs wafer. The dots are inside a charge-tunable device, with a doped layer in the wafer as an ohmic contact and a deposited metal Schottky contact. This allows the deterministic loading and unloading of charge carriers (generally electrons) into the QDs, as demonstrated in Fig. 2.2.[1, 2] The application of an electric field also Stark shifts the excitonic lines in the QD's emission, allowing a small degree of charge tuning. An AlAs/GaAs superlattice between the QD layer and the Schottky contact prevents current leakage through the sample. Diagrams of the sample structures are shown in Fig. 2.1, and dimensions of the charge-tunable samples are given in Table 2.1.

Samples 050328C#2 and 050328C#8c were grown by Brian Gerardot at the University of California Santa Barbara, USA, samples VN2063, VN2209 and VN2455 were grown by Edmund Clarke at the University of Sheffield, UK, and sample KV14101 was grown by Jingdong Song at the Korea Institute of Science and Tech-

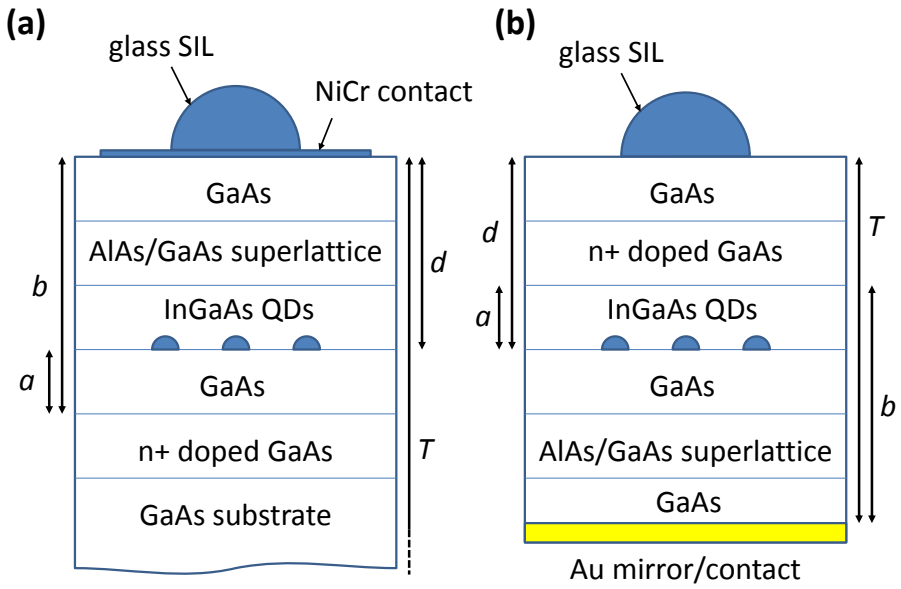

Figure 2.1: Diagrams of the two types of sample used. (a): "Bulk" sample, where the n-doped GaAs provides the back gate and the NiCr deposited on top provides the top Schottky contact. The n-i-Schottky device is directly on top of a thick ($\sim 0.5mm$) GaAs substrate. (b): "Membrane" sample, where the Au mirror also acts as a Schottky contact and the n-doped GaAs contact is above the QD layer. Further detail on sample dimensions is given in Table 2.1.

nology, South Korea.

2.2.1 Sample preparation

Performing spectroscopy on a single QD relies on being able to isolate its emission lines from any others surrounding it. For this reason, it is desirable to perform experiments on samples with a low density of QDs. During QD sample growth, the base and capping layers of GaAs are grown by molecular beam epitaxy (MBE) on a rotating substrate. For the QD layer, however, the rotation is halted and so the geometry of the MBE chamber results in a density gradient of In across the sample, and thus a density gradient of QD formation.[3]

Fig. 2.3 shows an example of a photoluminescence (PL) map from a wafer, showing regions where the wetting layer provides the brightest PL peak (blue) and where the QD PL dominates (green). Samples taken from the green/blue edge in the PL map will have lower QD densities and so will be more suitable for experiments on single QDs. The spectra in Fig. 2.3 also show an asymmetric QD emission peak with the peak towards higher wavelengths: this indicates that the distribution of QD wavelengths is skewed towards higher wavelengths. This means that even in a relatively high-density sample, it may still be feasible to take measurements from isolated low-wavelength QDs.

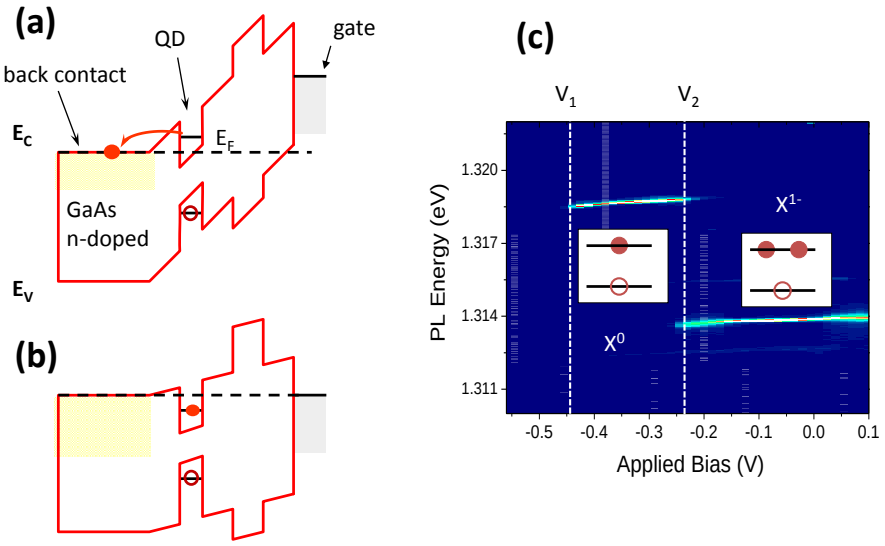

Figure 2.2: Example band structure showing charged-state selectivity, and typical PL map. (a) shows a representative band structure at a bias voltage $V_g < V_1$. In this case, the single conduction band electron energy level is above the Fermi level (dashed black line), so any electron promoted to the conduction band in the QD via optical pumping will rapidly tunnel out of the QD. (b) shows the case when the $V_g > V_1$: the band structure "tilts", dropping the single electron level below the Fermi level, allowing one electron to remain in the QD, resulting in the neutral exciton state X_0. Further increasing V_g to V_2 allows a single electron to tunnel into the QD from the doped layer, and remain in the QD when another electron is raised to the conduction band via optical pumping, causing the negatively charged exciton X^{1-} to form. (c) is a PL map for increasing V_g, showing the excitonic plateaus appearing and disappearing at V_1 and V_2.

"Bulk" samples

The majority of the samples used here are so-called "bulk" samples (to distinguish them from the $\sim$ micron thick "membrane" samples. These samples all share the same processing steps to produce a working device:

1. A sample is cleaved from the wafer along the [110] and [$\bar{1}$10] crystallographic axes. The samples are generally on the order of 1 cm $\times$ 1 cm.

2. Ohmic contacts to the doped layer are fabricated using indium or gold-germanium: either small pieces ($\sim$ 1 mm) of In are placed on the surface of the sample, close to the edge, or small (again $\sim$ 1mm) spots of AuGe are deposited in the sample using an electron-beam evaporator and shadow mask. The sample is then heated to 300°C for 90 minutes to allow the metal to diffuse down to the doped layer. Once this annealing is complete, the resistance between the back contacts is tested: ideally there should be a small resistance between any two

Sample name	T (μm)	a (nm)	b (nm)	l	d (nm)	λ (nm)
050328C#2	100	25	161.3	6.45	136.3	950
050328C#8c	500	25	161.3	6.45	136.3	950
VN2063	380	25	161.3	6.45	136.3	950
VN2209	380	15	400	26.7	385	1300
VN2455	0.6422	25	201.2	8.05	466	950
KV14101	0.3494	25	221.6	8.864	152.8	950

Table 2.1: Dimensions of the samples used in this thesis. T is the overall thickness of the sample, a is the distance from the doped contact to the QD, b is the distance between the contacts, $l = b/a$ is the lever arm of the device, used to determine the electric field at the QD layer for a given voltage across the device, d is the distance of the QD layer from the top surface of the wafer, and λ is the nominal QD emission wavelength. The 050328C samples were grown at the University of California Santa Barbara and contain partially-capped island QDs, VN2063 and VN2455 contain In-flush QDs, and VN2209 contains dots-in-a-well (see previous chapter for more details of QD types). The "VN" samples were grown at the University of Sheffield. Sample KV14101 was grown at the Korea Institute of Science and Technology.

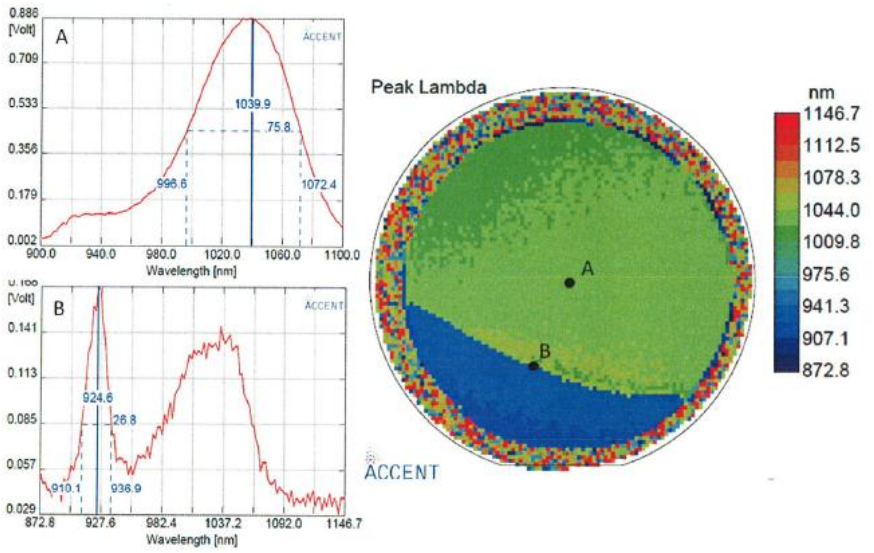

Figure 2.3: Room temperature PL map of In-flush (see chapter 1) QD sample VN2063, used in chapter 3. The PL maps shows the peak wavelength at that point on the wafer: blue (green) regions are where the wetting layer (QD emission) is brightest. Plots A and B show spectra taken at points A and B on the sample. B demonstrates much lower QD counts (higher wavelength peak) than A, indicating a lower density of QDs at this point. Measurements made by Edmund Clarke, Sheffield University, UK

back contacts.

3. The Schottky gate is fabricated using nickel-chrome: an electron beam evaporator is used to deposit a thin (< 5nm) layer of NiCr on the top surface of

the sample, with a shadow mask to mark out the gate shape. The top contact is usually keyhole-shaped, with a 2 mm diameter circular part that will be covered with a glass solid immersion lens (SIL) and a $\sim$ 1 mm $\times$ 1 mm tab that will be connected to external wires with conductive silver paint.

4. At this point, the sample is tested: firstly, there should be a large resistance $\sim$ 1MΩ between the top contact and back contact. Secondly, an oscillating voltage of frequency 130 Hz and peak-to-peak amplitude of 10 mV is applied between the top and back contacts. The current and phase are measured: the current 90° out of phase with the voltage is determined by the capacitance of the device:

$$I = 2\pi\nu V_{AC} C \tag{2.1}$$

$$C = \frac{\epsilon_0 \epsilon_r A}{d} \tag{2.2}$$

where ν and V_{AC} are the frequency and amplitude of the AC voltage, C is the capacitance of the device, ϵ_0 is the vacuum permittivity, $\epsilon_r = 12.9$ is the dielectric constant for GaAs, A is the Schottky gate area and d is the distance between gates. For typical values $A = 4$ mm^2, $d = 161.3$ mm, the out-of-phase current is 23 nA, which is a typical value recorded for a working sample. In the ideal case, the current has a phase $\sim 90°$ relative to the applied voltage. A low current suggests a loose contact or broken top contact, whereas a high current or low phase ($< 70°$) suggests current leakage between the top and back contacts. This test is done in the dark as there will be a small degree of photocurrent that will result in a lower than ideal phase.

Membrane sample

For some of the RF experiments, samples with significantly different structures were used: designed[4] and fabricated by Dr Yong Ma at Heriot Watt University, UK, and grown by Edmund Clarke at Sheffield University, UK, and Dr Jingdong Song at the Korea Institute of Science and Technology, South Korea. These samples are "membranes" in that they are significantly thinner than the bulk samples. The relative thinness of the sample is due to the inclusion of a planar cavity antenna: the thickness was chosen such that when the membrane is mounted on a gold mirror, it would act as a planar cavity. This increases the coupling out of sample from the $< 1\%$ expected from a bulk sample to $> 25\%$. The gold mirror acts as a Schottky contact. This is a further improvement to the bulk sample, as the NiCr top contact is only semi-transparent to IR, whereas the n+ doped layer is transparent, resulting in fewer losses.

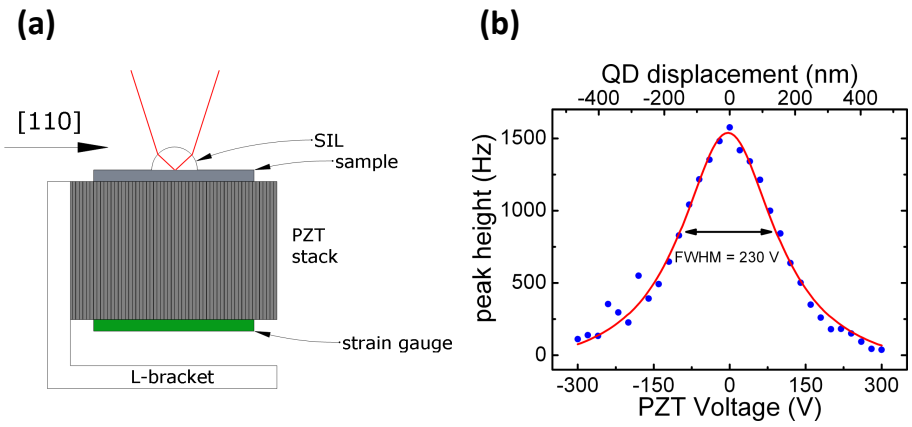

Figure 2.4: Diagram of the strain application set-up (a) and the intensity of a QD as the PZT voltage is tuned (b). The FWHM of the intensity profile corresponds directly to the focus spot diameter.

2.2.2 Sample mounting

Once a sample has been prepared and tested, it is mounted in one of two ways. In the case of a strain tuning experiment, the sample prepared in a configuration similar to Seidl *et al*[5]: it is glued onto the side of a lead zirconate titanate (PZT) piezoelectric stack using two-part epoxy with its [110] axis in the direction of expansion for the PZT. This allows the application of uniaxial strain to the QDs embedded in the sample along the [110] axis. A strain gauge is glued to the opposite side of the PZT to check that the PZT is operating properly. The PZT itself is glued by its bottom surface to a metal plate which attaches to an L-shaped bracket, allowing the strain assembly to be mounted with the sample facing upwards. The plate also has small solder pads glued on to secure the wires that go to the PZT, strain gauge and electrical contacts on the sample.

In this configuration, the amount of strain applied is calibrated using an optical method, which depends on the fact that the PZT is fixed at one end, and so the QD will move across the focus spot as the PZT expands and contracts. In addition, the distance a given QD moves is coincidentally on the order of the collection focus spot size. The spot is diffraction limited, so as a QD moves through the focus, the intensity of its photoluminescence against PZT voltage takes the form of the Airy disc, the centre of which can be approximated by a Gaussian peak (Fig. 2.4 (b). The FWHM of this Gaussian will be the focus spot diameter, which is given by[6]

$$\Delta x = \frac{0.52\lambda}{\mathrm{NA}_{obj} n} \tag{2.3}$$

where Δx is the focus spot diameter, λ is the light wavelength, NA_{obj} is the numerical aperture of the objective lens, and n is the refractive index of the SIL. For $\lambda = 950$

nm, $NA_{obj} = 0.68$ (for Thorlabs C390 TM-B aspheric lens) and $n = 1.99$ for an LASFN-35 glass hemispherical SIL, the spot diameter is 365 nm. From this, the strain per unit PZT voltage can be determined, as can the total strain difference available, given a maximum voltage range of 600 V on the PZT.

In the case where strain tuning is not used, the sample is simply attached to an Al "button" holder using varnish (Oxford Instruments GE Low Temperature Varnish: can be removed with a solvent such as acetone so that the sample and button can be re-used). This button again has solder pads attached to secure the connecting wires to the charge-tunable device.

Once the sample is placed and contacted, a glass SIL is placed on the top surface of the sample (over the top contact in bulk samples), using a small amount of vacuum grease to hold it in place. The sample and holder are then mounted on top of an XYZ nanopositioner stack (attocube systems ANP series) which is incorporated into a Thorlabs 30mm cage system. Above the sample a 0.68 NA objective lens is mounted so that the objective is more than its working distance away from the top of the SIL when the z-positioner is "parked" at its lowest extension. The sample is centred by using the XY positioners.

2.3 Cryostat

As the experiments to be performed are extremely sensitive to thermal effects such as inhomogeneous broadening of the QD emission due to phonon interactions, the sample must be cooled to cryogenic temperatures, so the sample is placed into a He cryostat. The microscope assembly is placed inside an aluminium tube, which is pumped to vacuum ($\sim 10^{-5}$ mbar). A small volume of helium is introduced into the tube as an exchange gas (to a pressure of ~ 25 mbar for the bare sample and $\sim 10^{-3}$ mbar for the strain-tunable sample, as the large voltages used to drive the PZT can result in spectacular plasma "fires" in even low concentrations of He at 4K). The tube has an AR-coated window at at the top end in line with the microscope assembly. It also incorporates several electronic feed-throughs to allow the components at the bottom of the microscope to be connected to the experimental instruments.

For experiments with strain-tuning, a helium bath-style cryostat is used: this is effectively a ~ 60 l Dewar flask of liquid helium at 4.2K that the tube is lowered into. This then remains at low temperatures until the helium boils off completely, and the tube and sample begin to warm up.

For resonance fluorescence experiments, a closed-cycle pulse-tube cryostat (attocube attoDRY1100) was used. This cycles helium using a compressor to keep the contents of the cryostat at or below liquid helium temperatures (in practice, a temperature of ~ 3.6 K is usual). An outer tube within the cryostat is flushed with He gas while the microscope tube is lowered into it to prevent any moisture condensing

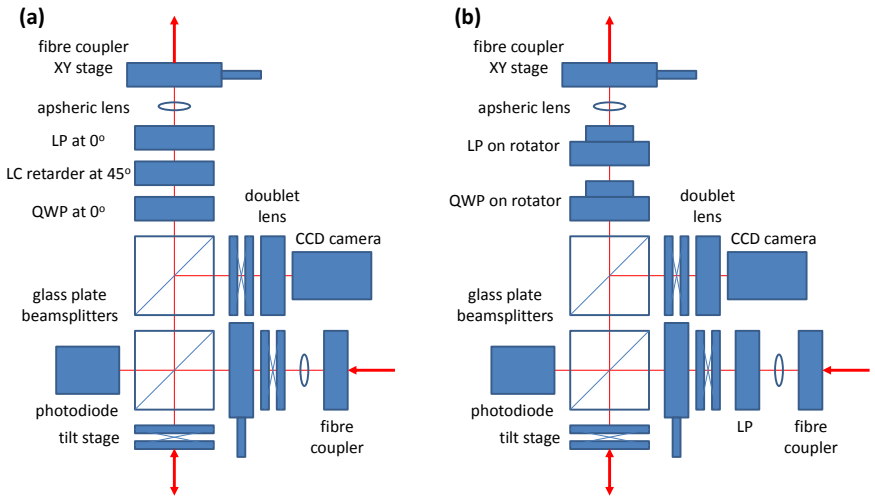

Figure 2.5: Diagrams of the two common microscope head configurations: (a) photoluminescence (PL) with polarisation rotation and (b) resonance fluorescence (RF). The polarisation optics in (a) are optional and used for polarisation rotation, with fast axis angles for the QWP and LC given relative to the linear polariser axis. LP: linear polariser, QWP: quarter wave plate, LC: liquid crystal, CCD: charge-coupled device.

on the walls of the outer tube, and the tube is then sealed and the sample allowed to cool down to operating temperatures.

The closed-cycle cryostat also incorporates a $\leq$ 9 T superconducting magnet which can be used to apply a magnetic field to the samples parallel to the growth axis (in the Faraday geometry), and so for this reason all of the components of the microscope and sample assembly are non-magnetic.

2.4 Optics

2.4.1 Collection optics

As previously noted, an objective lens is mounted at the bottom of the microscope, above the sample. On top of the microscope tube, above the AR-coated window, the microscope "head" is mounted. This is constructed primarily from Thorlabs 35mm cage system components and consists of a central block of beamsplitters with various "arms" mounted above and to the sides. Diagrams of the two common head configurations are given in Fig. 2.5.

The central block is a custom-made aluminium cage which contains two beamsplitters, which are thick glass plates mounted at 45° to the optical axis. These are set up such that there is one vertically-aligned collection arm and a possible 4 side arms. The central block rests on a tilt stage.

The top arm is the collection arm, and consists of a collimating lens on a z-translation stage and a fibre coupler on an xy-translation stage, with more optional

polarisation optics included before the lens. These include the polarisation rotation and polarisation cancellation set-ups, which will be explained in more detail below. The collection arm is aligned and collimated to the expected wavelength of the emission, and the tilt stage under the central block is used to centre the arm's optical axis along the microscope.

The usual layout is to mount on the sides of the central block an excitation arm, an alignment arm, and a photodiode opposite to the excitation arm to provide measurement of the excitation laser power, in addition to the vertically-mounted collection arm. The excitation arm is similar to the collection arm in that it includes a lens mount and collimating lens on translation stages, but it is attached to the central block via a reinforced tilt stage (Thorlabs with extra springs added to prevent "creep"). The excitation arm is collimated to the wavelength of the excitation: 830nm in the case of photoluminescence and the wavelength of collection for resonance fluorescence (RF). Once the collection arm is aligned to the sample, the tilt stage on the excitation arm is used to co-align it to the collection arm. For RF, the excitation arm also incorporates a linear polariser (LP) that is used for the polarisation cancellation set-up. The polarisation of the excitation laser and orientation of the excitation arm LP is chosen such that the largest possible fraction of incident light is reflected down to the sample, resulting in a reflection of $\sim 4\%$ and transmission of $\sim 96\%$.

The alignment arm is made up of a doublet lens and a CCD camera: this allows focus spots from the excitation and collection to be imaged on the sample and co-aligned.

Polarisation rotation

To perform polarisation-resolved photoluminescence, a polarisation rotator is included in the collection arm (Fig. 2.5 (a)). This is made up of a quarter wave plate (QWP), a liquid crystal variable retarder (Meadowlark Optics LVR-100) with its fast axis at 45° to that of the QWP, and an LP aligned to the QWP. This set-up takes the polarisation profile of collected light and rotates it before it passes through the LP. As such, by applying different signals to the retarder, the polarisation profile can be rotated to record the intensity of different angled components of the polarisation, and thus plot out the shape of the polarisation. It is clear to see how this will work with circularly polarised light: the light passes through the QWP and becomes linearly polarised at 45° to the QWP's fast axis, and so is aligned to the retarder's fast axis. Changing the signal to the retarder has no effect on the light as it does not see the changing birefringence. The signal thus does not change as the polarisation is rotated, resulting in a constant intensity for all angles, giving a circular pattern. This extends to all patterns of input polarisation. The rotator is calibrated by setting the retarder to a known voltage amplitude (the retarder oper-

ates with a square voltage wave as control), sending light through it backwards and through an LP (the analysis LP) mounted on a rotation stage, and rotating the LP until the signal through is maximised. The relative angle between the rotator LP and the analysis LP gives the angle of rotation for that voltage amplitude.

Polarisation cancellation

RF presents a challenge with this confocal set-up as the emission of the QD is at the same energy as the excitation laser and the QD signal and reflected laser signal are collected into the same optics. It is impossible to spectrally filter out the excitation and keep all of the information given by the QD spectrum (while the spontaneous emission of the QD is lifetime broadened compared to the laser, attempting to use a narrow filter to block out the central reflected peak also filters out the narrow peak from elastically Rayleigh-scattered photons in the QD spectrum, and this contribution is particularly important for high coherence and indistinguishable photons). As such, a polarisation cancellation scheme is used[7, 8, 9], as in Fig. 2.5 (b): the excitation arm contains an LP (Meadowlark custom Ultra High Extinction Ratio polariser, extinction ratio $> 10^8$) to ensure that the excitation light is highly linearly polarised, and the collection arm incorporates a QWP and LP on separate piezoelectric rotation stages (attocube systems ANR240, typical step size at 300 K $= 10^{-3\circ}$). Since the excitation radiation is highly linearly polarised but the emission from the QD is either circularly polarised for the case of the charged trion or two orthogonal linear components separated by the fine structure splitting (FSS) for the neutral exciton, it is possible to rotate the collection LP to cancel the reflected laser signal, while still admitting half of the QD signal. The QWP is included to compensate for any birefringence in the microscope optics. By measuring the intensity of incident light and the admitted light, an extinction ratio of up to 10^8 has been recorded, with a typical operation value of 10^7. The polarisation cancellation set-up is extremely stable over time, with an expected day-to-day extinction ratio loss of a factor of < 10.

2.5 Excitation optics

Four lasers are used for excitation, alignment or other applications in these experiments:

- A fixed laser diode at 830nm. This is used for non-resonant excitation of QDs.
- A Littrow-configuration external cavity diode laser (ECDL) (Toptica DLPro 940, wavelength range 910 nm – 985 nm). This is used as excitation for RF at around 950nm. The wavelength is finely tuned by tuning the voltage to a

piezoelectric element in the laser that changes the length of the cavity. There is an external coarse control for hand-tuning large distances.

- A motor-controlled tunable ECDL (Sacher Lasertechnik Motorized Lion Littman/Metcalf ECDL TEC-500-0960-030-M, wavelength range 920 nm – 985 nm). This is used mainly for alignment of microscope optics and as a reference laser in Fabry-Perot interferometry. It is generally not used as excitation as it is not as stable as the Toptica laser diode, but it is used for 2-laser excitation in RF with applied magnetic field. This has a piezo-controlled cavity for fine tuning and a motor for coarse tuning.

- A tunable ECDL (custom Sacher Lasertechnik Lion Littman/Metcalf ECDL TEC-500 model, wavelength range 1276 nm – 1322 nm). This is used exclusively for alignment of microscope optics at telecomms wavelengths.

Each laser has coupling optics which are made up of a fibre coupler and collimation lens on translation stages, along with QWP and half wave plate (HWP) on rotation mounts. These are used to maximise signal to the sample, and, specifically in RF, to align the polarisation of the laser light to the excitation arm LP. The laser optics also incorporate a variable attenuator to control the excitation power.

In addition, the 950nm lasers have optical isolators to prevent back-reflections that may destabilise the laser mode, and a beamsplitter to pick off a small fraction of the laser field and send it to a wavemeter via collimation lens, fibre coupler and single mode fibre. The wavemeter (High Finesse WS/7, measurement resolution 10 MHz) has an incorporated PID controller that can be used with both 950nm lasers to lock their wavelengths to a given value. The uncertainty in locking is on the order of 0.001 nm.

2.6 Optical characterisation

The collection arm of the microscope head couples into a single mode fibre. This fibre can then be used as input to a number of different analysis optics set-ups, dependent on what experiment is taking place. The general scheme is shown in Fig. 2.6.

2.6.1 Spectrometer

Spectrometers (Acton SpectraPro-500i) are used mainly for photoluminescence experiments. Two were used: one with a liquid N_2-cooled silicon CCD for 950nm samples and one with a liquid N_2-cooled InGaAs linear array for telecoms wavelength samples. The 950nm spectrometer has a turret with 3 available gratings: 300 g/mm, 1200 g/mm and 1800 g/mm. The 1800 g/mm grating, at around 950nm, results in a resolution of $\sim 35\mu$eV

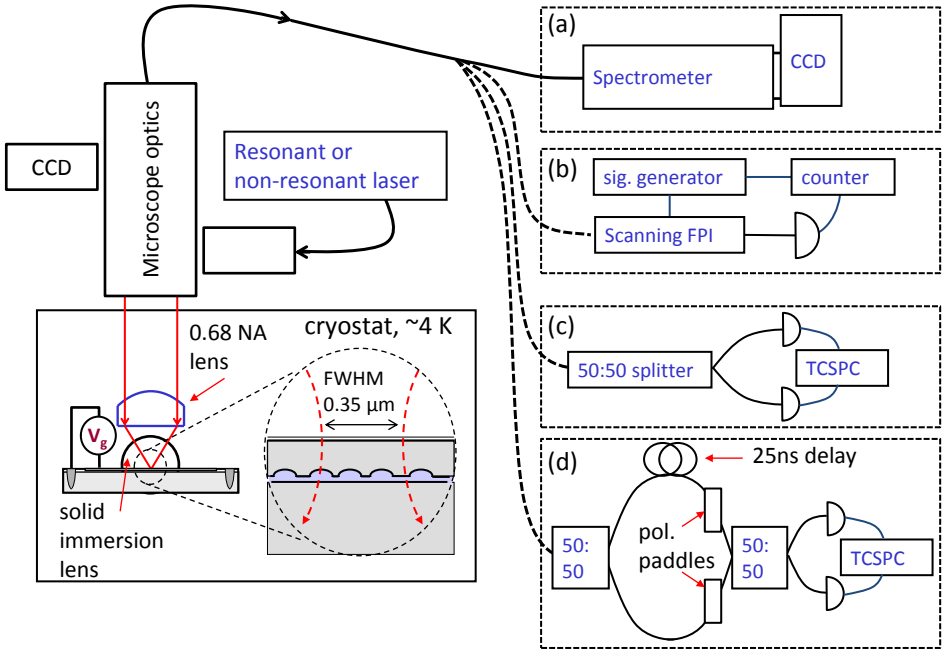

Figure 2.6: Diagram of the overall optical set-up for QD experiments. The microscope optics are either of the head configurations given in Fig. 2.5. (a): the spectrometer set-up. (b): the scanning Fabry-Pérot interferometer set-up: the signal generator auxiliary output is used to synchronise the data acquisition to the voltage sweeps. (c): the in-fibre Hanbury-Brown-Twiss interferometer for second-order correlation measurements. (d): the in-fibre Mach-Zehnder interferometer for indistinguishability measurements. The intermediate arms of the interferometer include a 25ns delay fibre in one and polarisation control paddles on both. TCSPC: time-correlated single photon counter.

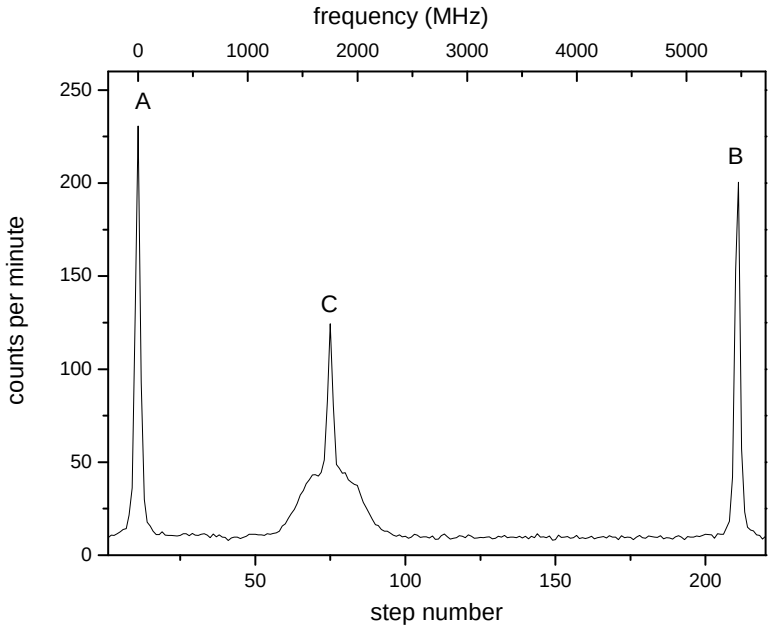

Figure 2.7: Example FPI spectrum. Peaks A and B are due to the reference laser and are separated by the FSR = 5.5 GHz. The number of data points between these peaks n is used to determine the step size $\delta\nu$ in MHz: $\delta\nu = 5500/n$. n is chosen to be close to the finesse = 200. The frequency range is shown on the top axis. Peak C is the QD spectrum.

2.6.2 Fabry-Pérot Interferometer

To take high resolution spectra of the RF signal, a scanning Fabry-Pérot interferometer (FPI, FFP-SI-950-27.5M0200-3.5-065 from Micron Optics) is used. The FPI is single-mode fibre-coupled, so the output fibre from the microscope head is mated directly to the input fibre for the FPI. The FPI takes a triangular wave voltage signal of maximum amplitude 12 V, supplied by an external signal generator. The output of the FPI is then sent to a single photon avalanche diode (SPAD – model number SPCM-AQRH-15-FC) to count the rate of photon transmission. The external TTL output of the signal generator is used to synchronise the counting electronics to the voltage sweeps. This allows a spectrum to be built up. The signal generator is set to operate at ~ 40 Hz, and the voltage is tuned until one sweep covers just over one free spectral range (FSR) of the FPI (in this case, 5.5 GHz). The gate frequency of the counting electronics (i.e. the rate at which photon rate readings are taken from the SPAD) is adjusted to set the measurement resolution, which should be set to close to the resolution of the FPI itself, given by FSR/finesse $= 5500/200 = 27.5$ MHz. The Sacher laser is used as a reference: the laser signal is combined with the QD signal in a 99:1 fibre splitter (FONTCanada) and it is detuned from the QD emission. The voltage amplitude is tuned so that two reference peaks appear in one sweep, and the gate frequency is adjusted so that the number of data points between the two peaks is close to 200. An example of an FPI spectrum is shown in Fig. 2.7.

The FPI undergoes some thermal drift on the minute timescale, resulting in shift of the peak positions over time. The bright reference laser peaks can be used to correct for this drift over time in analysis. There is also a birefringent peak shift in the FPI: a given wavelength peak will be split into two dependent on its polarisation, with a splitting of ~ 500 MHz. Polarisation control paddles are used on the input fibre to correct for this and ensure only one peak appears for the QD spectrum.

2.6.3 Photon coincidence measurement

Two different types of coincidence measurement are done using the QD signal: measurement of second-order correlations (measurement of $g^2(\tau)$) and measurement of two-photon interference (Hong-Ou-Mandel interference, or HOM). In these experiments, the signal from two SPADs is processed by a 2-channel PicoQuant PicoHarp 300 time-correlated single photon counting (TCSPC) system to produce a histogram of delays between photon arrivals.

Second order correlation

$g^2(\tau)$ is measured using a very simple Hanbury-Brown-Twiss interferometer (HBT), which consists entirely of a 50:50 single mode fibre splitter (FONTCanada). The output fibre from the microscope is mated with the input fibre to the 50:50 splitter, and the outputs go directly to two SPADs.

Two-photon interference

HOM interference is measured by using a fibre-based asymmetric Mach-Zehnder interferometer. This is composed of a 50:50 fibre splitter connected to a 2×2 50:50 fibre splitter. Due to the QD being a good single photon emitter, in order to have the chance of two photons meeting at the second splitter at the same time, a long delay fibre is put into one arm of the interferometer such that the delay is longer than the lifetime of the spontaneous emission (~ 1 ns). Since the HOM effect depends on the indistinguishability of the incident photons, including their relative polarisations, polarisation control paddles are used in the arms of the interferometer before the second fibre splitter. These allow the polarisation of the incident photons to be parallel to see the HOM effect, as well as crossed to provide a baseline signal to calculate the HOM visibility. Like the HBT set-up, the output from the second splitter is sent to two SPADs, and the signal is processed by the PicoHarp TCSPC system.

2.7 Summary

Quantum dot samples have been processed to produce charge- and strain-tunable devices with suitable QD densities to perform measurement on single QDs. A highly stable, diffraction limited cryogenic microscope set-up has been constructed and used to collect both photoluminescence and resonance fluorescence from the QDs. Measurements have been made on the outcoming light using four different measurement schemes: a spectrometer for PL measurements, a scanning Fabry-Pérot interferometer for high-resolution spectra of RF signals, a Hanbury-Brown-Twiss set-up for second-order correlations of RF, and a Mach-Zehnder for Hong-Ou-Mandel effect measurements of photon indistinguishability.

2.8 References

[1] Drexler, H., Leonard, D., Hansen, W., Kotthaus, J. P. & Petroff, P. M. Spectroscopy of Quantum Levels in Charge-Tunable InGaAs Quantum Dots. *Phys. Rev. Lett.* **73**, 2252 (1994).

[2] Warburton, R. J. *et al.* Optical emission from a charge-tunable quantum ring. *Nature* **405**, 926 (2000).

[3] Leonard, D., Pond, K. & Petroff, P. M. Critical layer thickness for self-assembled InAs islands on GaAs. *Phys. Rev. B* **50**, 11687 (1994).

[4] Ma, Y., Kremer, P. E. & Gerardot, B. D. Efficient photon extraction from a quantum dot in a broad-band planar cavity antenna. *Journal of Applied Physics* **115**, 023106 (2014).

[5] Seidl, S. *et al.* Effect of uniaxial stress on excitons in a self-assembled quantum dot. *Applied Physics Letters* **88**, 203113 (2006).

[6] Gerardot, B. D. *et al.* Contrast in transmission spectroscopy of a single quantum dot. *Applied Physics Letters* **90**, 221106 (2007).

[7] Matthiesen, C., Vamivakas, A. N. & Atatre, M. Subnatural Linewidth Single Photons from a Quantum Dot. *Phys. Rev. Lett.* **108**, 093602 (2012).

[8] Nick Vamivakas, A., Zhao, Y., Lu, C.-Y. & Atatre, M. Spin-resolved quantum-dot resonance fluorescence. *Nat Phys* **5**, 198 (2009).

[9] Kuhlmann, A. V. *et al.* A dark-field microscope for background-free detection of resonance fluorescence from single semiconductor quantum dots operating in a set-and-forget mode. *Review of Scientific Instruments* **84**, 073905 (2013).

Chapter 3

Strain tuning

3.1 Introduction

Much of the work in this chapter is presented in Refs. [1, 2]

In this chapter, I will cover the results of a number of experiments performed by applying uniaxial strain to the QD samples. Firstly, photoluminescence is carried out on many QDs from three different QD samples, each containing different types of QD: partially capped island (PCI), In-flush and dot-in-a-well (DWELL). Strain and electric fields are applied to the QDs, and from this it possible to obtain the dependence of photon energy as the applied strain is tuned for the neutral and negatively charged excitons, X^0 and X^{1-} respectively. We find that in a given sample, two adjacent QDs can have very different energy tuning slopes with strain, signifying that it is in principle possible to tune two adjacent (i.e. in the same focus spot) QDs into resonance with each other: a useful property for the generation of entanglement between spins in and photons from separated QDs.

From the PL of the QDs under strain and charge tuning, it is possible to model the behaviour of single particles in the QD using a perturbative Coulomb blockade model. In all cases, this yields the conclusion that while the photon energy tuning range with strain is smaller than 1 meV, the tuning ranges of the electrons and holes in the exciton are considerably larger: on the order of 10s of meV. An attempt is made to use the single particle and exciton tuning slopes in conjunction with the deformation potentials of InAs and GaAs to estimate the composition of QDs. The result of this is that simply using deformation potentials to investigate the composition is not enough: this model does not take into account factors such as size and shape of the QD.

I also investigate the effects that strain tuning has on the fine structure splitting (FSS) of the X^0 of different QDs. Polarisation-resolved PL is carried out on three samples: one containing PCI QDs with charge- and strain-tunability, and two containing DWELL QDs, with charge and strain tuning and one in bulk with no tuning. Measurements made on the DWELL samples with no tuning give statistics

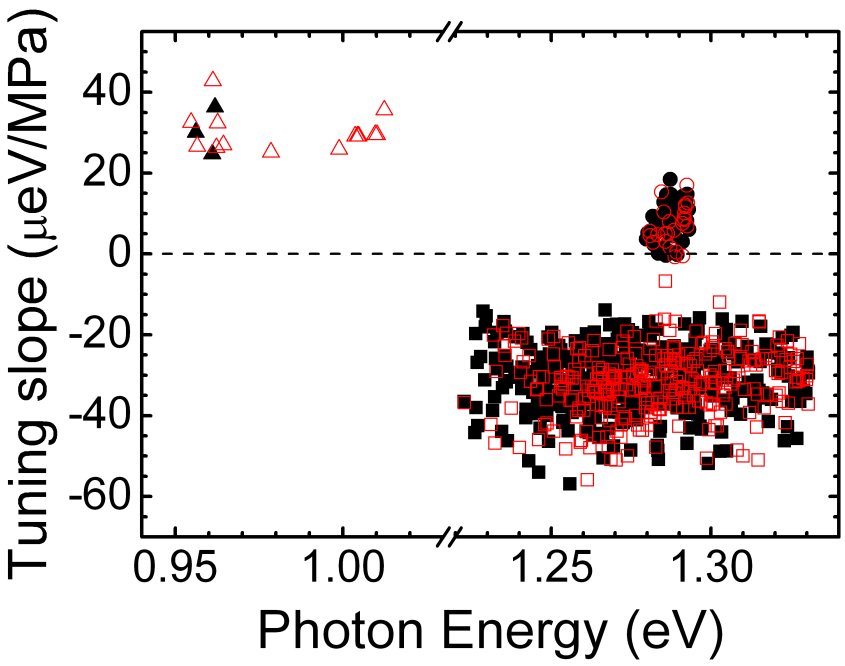

Figure 3.1: dE^{X^0}/dS (open red symbols) and $dE^{X^{1-}}/dS$ (filled black symbols) as a function of transition energy for several QDs in the samples studied. A positive (negative) tuning slope refers to a blue-(red-)shift under tensile stress. Circles: PCI, squares: In-flush and triangles: DWELL.

for nominal FSS for 1300nm QDs. Measurements of FSS tuning with strain were made on the tunable PCI and DWELL QDs. While significant FSS tuning is observed, it was not possible with these samples and this particular strain set-up to apply a large enough range of strain to eliminate the FSS.

3.2 Exciton tuning

In these experiments the focus is on two exciton states: X^0 and X^{1-}. The results of sweeping the PZT voltage (V_{PZT}) with a constant device bias voltage (V_{Gate}) clearly show that both X^0 and X^{1-} transition energies (E^{X^0} and $E^{X^{1-}}$, respectively) shift linearly with V_{PZT}, but different QDs exhibit widely variable tuning slopes. Statistics on the tuning slopes dE^{X^0}/dS and $dE^{X^{1-}}/dS$ as a function of nominal energy ($dS = 0$) are shown in Fig. 3.1 for 786 total transitions from 3 different samples. Differences in both dE^{X^0}/dS and $dE^{X^{1-}}/dS$ are observed within the same focus at all spatial positions examined, confirming the variable tuning behaviour is due to inherent differences in the QDs. Counter-intuitively, we do not observe a relationship between the transition energies and the tuning slopes. Such varied tuning behaviour is in qualitative agreement with other recent experimental results and theoretical predictions that a dot's response to uniaxial strain is highly dependent on its size, shape, and composition, which varies even for QDs with identical transition energies

[3, 4]. In addition, there are clear differences for the distributions of both dE^{X^0}/dS and $dE^{X^{1-}}/dS$ for the three different growth processes, which demonstrates that different growth processes result in overall differences in QD morphology.

It is possible to exploit the variable tuning slopes to reversibly and deterministically tune transitions in separate QDs through degeneracy. One such example is shown in Fig. 3.2 for the X^0 transitions from two QDs (labelled QD1 and QD2). At $V_{PZT} = +300$ V, the energy difference ($\Delta E^{X^0}_{1-2}$) between the two QDs is -190 µeV (where $E^{X^0}_1$ and $E^{X^0}_2$ are defined as the middle of the FSS). However, QD1 has a smaller tuning slope than QD2, so that $\Delta E^{X^0}_{1-2} = +67$ µeV at $V_{PZT} = -300$ V. Each transition from each dot becomes degenerate at a separate V_{PZT} value. For instance, at $V_{PZT} \approx$ -200 V, the y-polarized transition from QD1 crosses the x-polarized transition from QD2. This highlights the potential for a scalable approach to achieve indistinguishable photons from multiple independent QDs on the same chip and in the same cryostat.

3.3 Single particle tuning: Coulomb blockade model

To gain further insight into the response of the dot under uniaxial stress, we uncover the individual behaviour of the electrons and holes in individual QDs by investigating Coulomb blockade as a function of V_{PZT}. Fig. 3.5 displays the PL as a function of V_{Gate} for the X^0 and X^{1-} transitions of two QDs (labelled QD A and QD B) with similar transition energies at 3 different V_{PZT} values. Under tensile stress, we observe that all four transitions have positive but varied energy tuning slopes (see Table 1). Furthermore, for each dot, with increasing tensile strain the plateau positions shift to more negative V_{Gate} values, the permanent dipole moment increase, the FSS decreases, and the energy difference between X^0 and X^{1-} increases ($\Delta E^{X^0 \rightarrow X^{1-}}$ where they crossover at $V_{Gate} = V_2$). These results are shown in Fig. 3.6. We can use the PL energies and charging voltages to quantify with sub-meV accuracy [5] the relative effect of S on E_C and the Coulomb interaction energies E^{11}_{eh} and E^{21}_{ee} (using the notation $E^{\alpha\beta}_{ab}$ where ab identifies the type of Coulomb interaction, ee for electron-electron and eh for electron-hole, α refers to the number of electrons, and β the number of holes in the dot). We use the highly accurate values dE_C/dS, dE^{X^0}/dS, and dE^{11}_{eh}/dS to estimate dE_V/dS.

We assume the dot is in the strong confinement limit, e.g. the electron and hole wave functions are determined by the confining potential and only slightly perturbed by the Coulomb interactions, and use an established perturbative Coulomb-blockade model [6, 7, 5]. As shown in Fig. 3.3, the input parameters for the model include: the tunnel barrier thickness a; the back gate to surface Schottky gate distance, b; the built-in voltage of the Schottky contact, V_0 ($V_0 = 0.62$ V); the electrostatic energy due to an image charge in the back contact, E_i for one electron (which is dependent

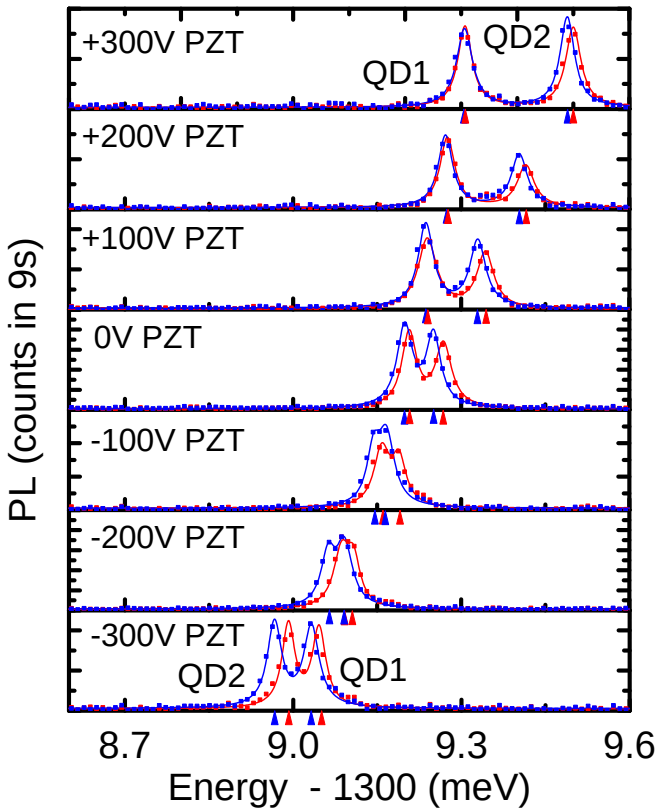

Figure 3.2: Strain tuning two QDs into resonance within the same focal position. QD2 exhibits a larger response to the strain than QD1 allowing tuning through degeneracy for each transition between the two QDs. E_x (blue) and E_y (red) show the data points and double-peak Lorentzian fits (solid lines) for the orthogonal polarizations in the basis of the FSS for both QDs. The triangles beneath the spectra identify the center peak positions from the fits. In addition to the center peak positions of QD1 and QD2, the FSS for each dot is affected by the uniaxial strain. Notably, for QD1 the FSS $< 10\mu$eV at $V_{PZT} = +300$ V and cannot be distinguished. [scale: minor tick marks = 200 counts]

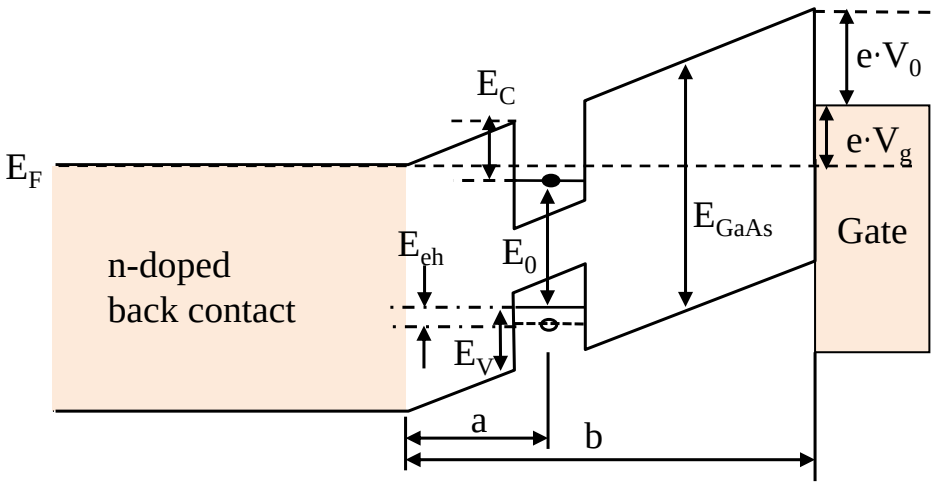

Figure 3.3: Simplified diagram of the band structure of a n-doped QD sample, with relevant Coulomb blockade energies labeled. This figure shows the energy levels of the electron and hole in X^0. Not shown is the image charge electrostatic energy E_i due to the electron proximity to the conductive n-doped layer. The lever arm λ is given by the ratio b/a.

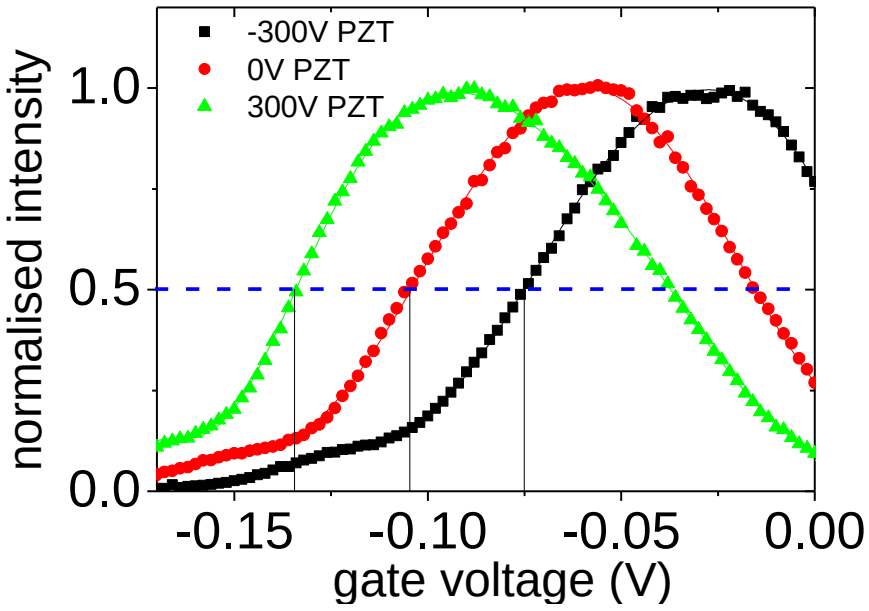

Figure 3.4: Plot of the X^0 plateau for -300, 0 and 300 V_{PZT}. V_1 is chosen as the point at which the plateau reaches half of its peak intensity (represented by the blue dashed line). V_2 is determined similarly for the high-voltage edge of the X^0 plateau.

on the tunnel barrier thickness for the sample: -1.1 meV for the PCI and In-flush samples, and -1.8 meV for the DWELL sample); the separation between E_C and E_V, E_0; the V_{Gate} at which a single electron tunnels into the dot (the left edge of the X^0 plateau), V_1; the V_{Gate} at which a second electron tunnels into the dot (the right edge of the X^0 plateau – see Fig. 3.4), V_2; the X^0 photon energy at V_1, E^{X^0}; and the difference in X^0 and X^{1-} photon energies at V_2, $\Delta E^{X^0 \to X^{1-}}$. The Fermi energy is set to 0 ($E_F \equiv 0$) so the potential at the dot is $e(V_0 - V_{gate})/\lambda$, where $\lambda = b/a = 6.45$ is the "lever arm" of the sample. Including Coulomb interactions, the relevant photon energies are:

$$E^{X^0} = E_0 - E_{eh}^{11} \text{ and} \tag{3.1}$$

$$E^{X^{1-}} = E_0 - 2E_{eh}^{11} + E_{ee}^{21} \tag{3.2}$$

and the gate voltage extent of the X^0 plateau is:

$$e(V_2 - V_1)/\lambda = E_{ee}^{21} - 2E_i \tag{3.3}$$

To obtain E_C, we first find E_{ee}^{21} from the experimentally determined values V_1 and V_2. E_{eh}^{11} can then be experimentally found from $\Delta E^{X^0 \to X^{1-}}$, which allows us to determine E_C based on the gate voltage at which a single electron tunnels into the dot (V_1). Unfortunately, the charging voltages V_1 and V_2 measured via PL are shifted together as V_{Gate} is intensity dependent down to extremely low excitation powers [5] because of a charge storage effect in the device. However, under constant excitation powers we can determine the *relative* changes in the charging voltages due to dS with very high accuracy. We note that the value dE_C/dS is the conduction band offset (CBO) of the single electron state in the dot including the change in the barrier offset due to dS. Finally, we can obtain the confinement energy for holes in the valence band: $E_V = E_{GaAs} - E_0 - E_C$, where E_{GaAs} is the GaAs band-gap, which we set to 1.5187 eV. We set E_{GaAs} to this constant value as the change in the valence band offset (VBO) of the barrier due to dS and the relative contributions of the conduction-band and valence band to dE_{GaAs}/dS are not established experimentally. Hence, the values we report for dE_C/dS are robust measurements including the change in $dCBO/dS$, whereas the value for dE_V/dS is an estimate which does not include $dVBO/dS$. Nevertheless, by combining the robust values of dE_C/dS, dE^{X^0}/dS, and $dE^{X^{1-}}/dS$, a complete understanding of the quantum dot's response to dS is obtained.

A key result revealed by the values for dE_C/dS and dE_V/dS for the two QD samples emitting around 950nm is that the single electron and hole states both red-shift significantly (≈ 0.22 meV/MPa), but $d\Delta E^{X^0 \to X^{1-}}/dS$ is small (≈ -0.44 μeV/MPa), indicating that the Coulomb interaction energies are modestly affected by dS. We note that values determined by the Coulomb-blockade model for dE_{eh}^{11}/dS and

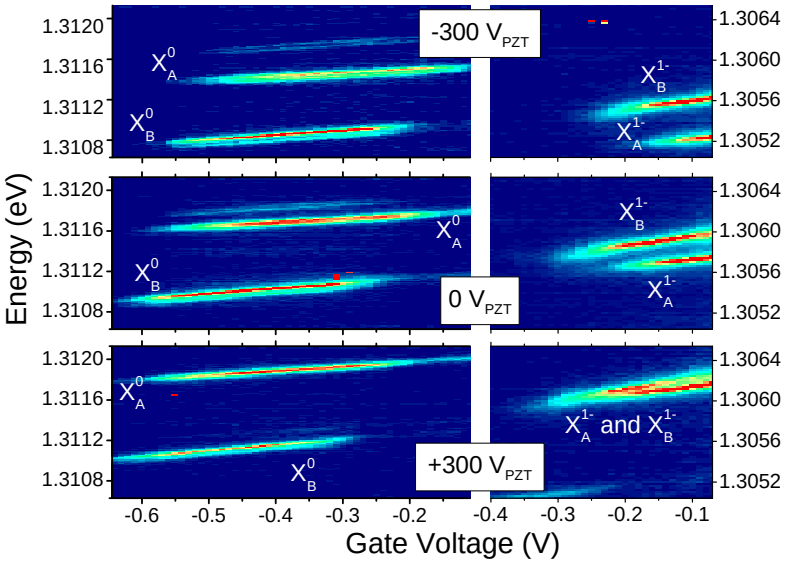

Figure 3.5: PL from QDs A and B as a function of sample gate bias for three different amounts of applied strain. As V_{PZT} = -300 V $\rightarrow$ V_{PZT} = +300 V each transition blue-shifts, V_{Gate} for the charge plateau decreases, and the Stark shift increases. Due to the different response of the two QDs to strain, X_A^{1-} and X_B^{1-} merge together at V_{PZT} = +300 V.

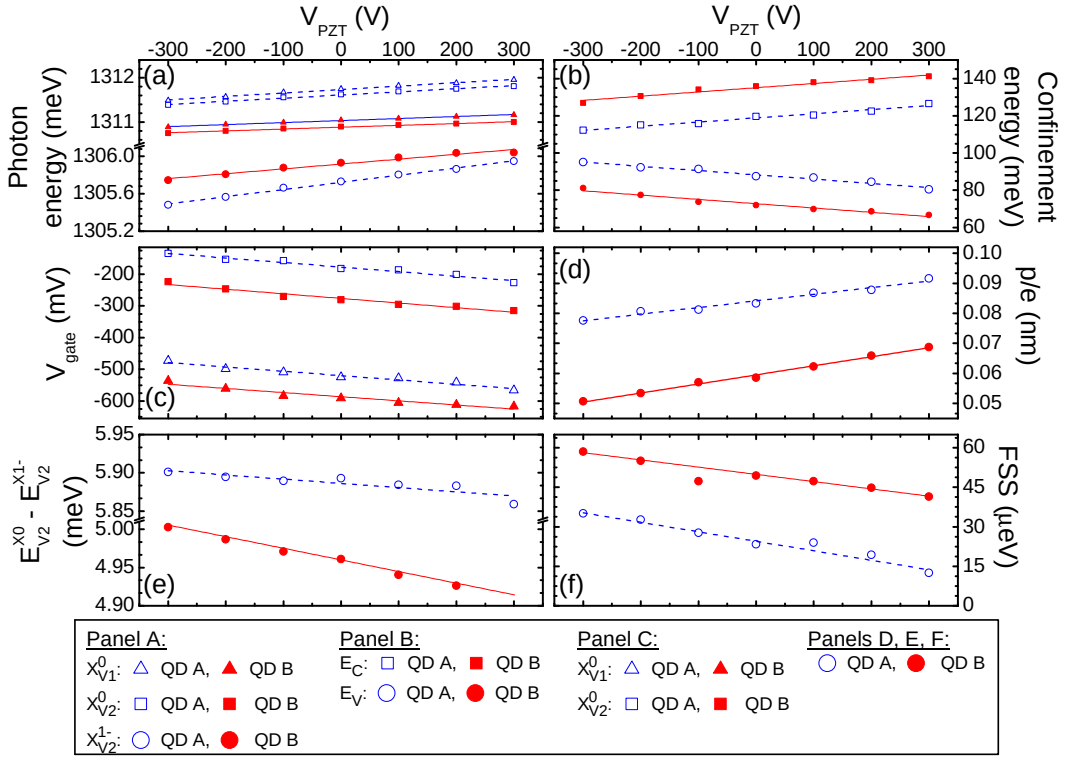

Figure 3.6: The response of QDs A and B as a function of uniaxial strain for several properties. V_1 refers to the most negative V_{Gate} edge of the X^0 plateaus and V_2 to the most positive (negative) V_{Gate} edge of the X^0 (X^{1-}) plateaus in Fig. 3.5

Table 3.1: Tuning slopes (in units µeV/MPa) for the exciton and single-particle energies for four different quantum dots from the three samples under tensile stress. 1: PCI, 2: In-flush and 3: DWELL

QD	dE^{X^0}/dS	$dE^{X^{1-}}/dS$	$d\Delta E^{X^0 \to X^{1-}}/dS$	dE_C/dS	dE_V/dS
1A	7.39	7.86	-0.48	203	-211
1B	7.20	8.63	-1.44	226	-233
1C	4.19	4.50	-0.32	230	-234
1D	7.01	7.89	-0.87	186	-193
2E	-30.8	-30.6	0.3	346	-315
2F	-24.0	-22.8	1.3	265	-241
2G	-37.4	-37.8	-0.4	394	-357
2H	-35.3	-33.7	1.5	395	-359
3I	49	39	9.9	-52	2.8
3J	29	25	4.6	-30	-0.3
3K	43	36	6.5	-44	1.2
3L	33	30	2.5	-40	7.1

dE_{ee}^{21}/dS are less than 18 µeV/MPa, the model's accuracy limit. Hence, dE^{X^0}/dS and $dE^{X^{1-}}/dS$ are determined predominantly by the considerable change in the single particle energies. The many-body effects are observed to be much weaker. Theoretical modelling [4, 3] of QDs with varying size, shape, and composition agree with the range of tuning slopes for exciton energies we observe. Combining the experimental and theoretical results yields a crucial insight: the precise balance of dE_C/dS and dE_V/dS determines the tuning of the exciton energies and is highly sensitive to the dot's inherent structural properties, not solely on the initial confinement potentials.

The change of the single exciton transition energy in response to a vertical electric field, i.e. the quantum confined Stark shift, also varies linearly with dS. The Stark effect is given by $E(F) = E_0 - p \cdot F + \beta \cdot F^2$, where F is the electric field, E_0 is the zero-field transition energy, p is the intrinsic vertical dipole moment which reflects the zero-field separation (p/e) of the electron and hole wave functions, and β is the polarizability. For X^0 and X^{1-} transitions in this field-effect structure, the quadratic term of the Stark effect is negligible and linear plateaus are generally observed. Fig. 3.6 (d) shows that p increases with increasing tensile stress, even though the change in confinement energies mostly cancel each other. Notably, the values for p/e at $V_{PZT} = 0$ V are less than previously reported, [8, 9] possibly due to pre-strain on the sample arising during sample cool-down.

Fig. 3.7 shows a plot of dE_C/dS against E_C for 18 QDs from the different samples. This displays an overall trend, with larger confinement energies giving smaller slopes. This makes intuitive sense as if a particle is more tightly confined, one would expect that an external perturbation would have a smaller effect on that particle. This in turn leads to a potential method of determining the composition of a given QD by considering the conduction band deformation potential a_c. Deformation potentials

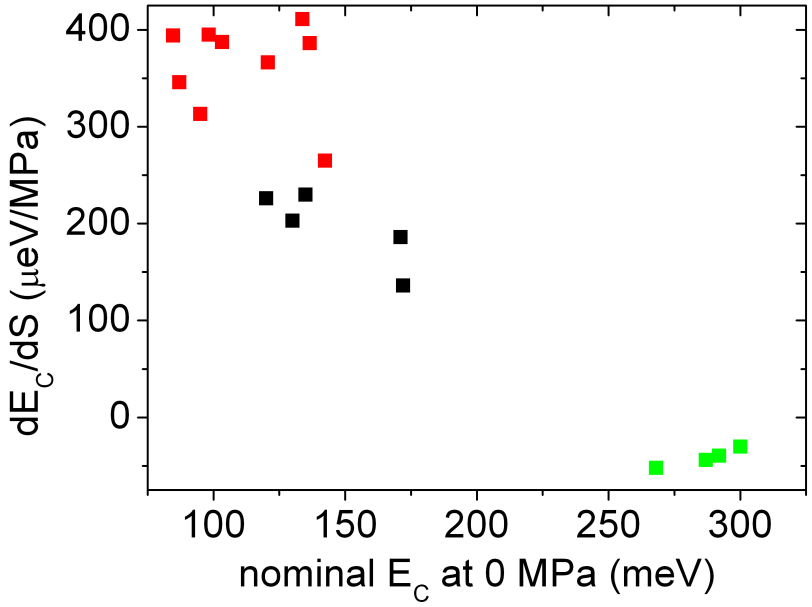

Figure 3.7: Plot of dE_C/dS vs nominal E_C (i.e. at 0 V_{PZT}) for PCI (black), In-flush (red) and DWELL (green) QDs.

describe how the energy of the conduction or valence band change as applied strain changes the lattice constant in the crystal.

3.4 Quantum dot composition

The tuning of conduction band electrons is dependent only on the hydrostatic strain:

$$\delta E_{CB} = -a_c(\Delta\epsilon_{xx} + \Delta\epsilon_{yy} + \Delta\epsilon_{zz}) \tag{3.4}$$

ϵ_{ij} is the i,j-th component of the strain tensor ϵ, which is related to the applied stress tensor σ by the relation $\epsilon = -s\sigma$, where s is the compliance tensor. This situation simplifies significantly in the case of uniaxial strain along [110]. Under application of stress p, the change in stress tensor components becomes:

$$\Delta\epsilon_{xx} = \Delta\epsilon_{yy} = -\frac{1}{2}(S_{11} + S_{12})p \tag{3.5}$$

$$\Delta\epsilon_{zz} = -2S_{12}p \tag{3.6}$$

where S_{ij} is the i,j-th component of the compliance tensor. Applying Eqs. 3.5 and 3.6 to Eq. 3.4 gives

$$\frac{dE_{CB}}{dp} = -a_c(S_{11} + 2S_{12}) \tag{3.7}$$

The tuning of the valence band with applied stress is more complicated and can be explained via the Bir-Pikus Hamiltonian: see Ref. [10] for more details of this treatment. The shift of the valence band relies on the isotropic and biaxial strain

Table 3.2: A table of the deformation potentials and compliance coefficients for InAs and GaAs. Deformation potentials from Ref. [11]. Compliance coefficients calculated as inverse of stiffness tensors from Ref. [12].

	InAs	GaAs
a_c (eV)	-5.08	-7.17
a_V (eV)	-1.16	-1.00
b_V (eV)	-2.0	-1.8
S_{11} $(\text{TPa})^{-1}$	19.5	11.7
S_{12} $(\text{TPa})^{-1}$	-6.88	-3.66

on the sample through the hydrostatic and biaxial deformation potentials a_v and b_v. For uniaxial strain along the [110] axis, this gives

$$\frac{dE_{VB}}{dp} = -a_v(S_{11} + 2S_{12}) - \frac{1}{2}b_v(S_{11} - S_{12}) \tag{3.8}$$

Combining Eqs. 3.7 and 3.8 gives a relationship for the exciton tuning slope due to band tuning:

$$\frac{dE_X}{dp} = -(a_c - a_v)(S_{11} + 2S_{12}) + \frac{1}{2}b_v(S_{11} - S_{12}) \tag{3.9}$$

The deformation potentials and compliance coefficients for bulk GaAs and InAs are known: see Table 3.2. Assuming that changing the composition of a QD results in a linear relationship between these values, an attempt at an estimate of the relative composition of a given QD can be made.

Using linear relationships of the form $x_{Ga} + (x_{In} - x_{Ga})r$, where $x_{In(Ga)}$ are the properties (deformation potentials or compliance constants) of InAs (GaAs) and r is the relative composition of the QD, values of this composition can be extracted from the exciton tuning slope data in Fig. 3.1.

In practice, this approach does not work. Since InGaAs QDs normally have a higher fraction of In to Ga, realistic results would be $0.5 \leq r \leq 1$ for all QDs, but this is not the case. While most of the tuning slope data for the PCI QDs fits within the "physically possible" allowed range $0 \leq r \leq 1$, a number of points fall outside this range, giving non-physical results: see Fig 3.8. In addition, all of the points for the In-flush and DWELL QDs fall outside this range. The simple band-tuning-only model does not capture the whole story for the exciton energy tuning.

A clear demonstration of this is that the range of values for conduction band tuning slope given by Eq. 3.7 is between 29.2 and 31.7 μeV/MPa, which is one order of magnitude smaller than the values reported for the electron confinement energy tuning of QDs emitting at 950 nm (Table 3.3), and this is before considering that the electron confinement tuning due to band tuning is given by the difference between conduction band tunings of the QD and the GaAs tunnel barrier (Fig. 3.9), which

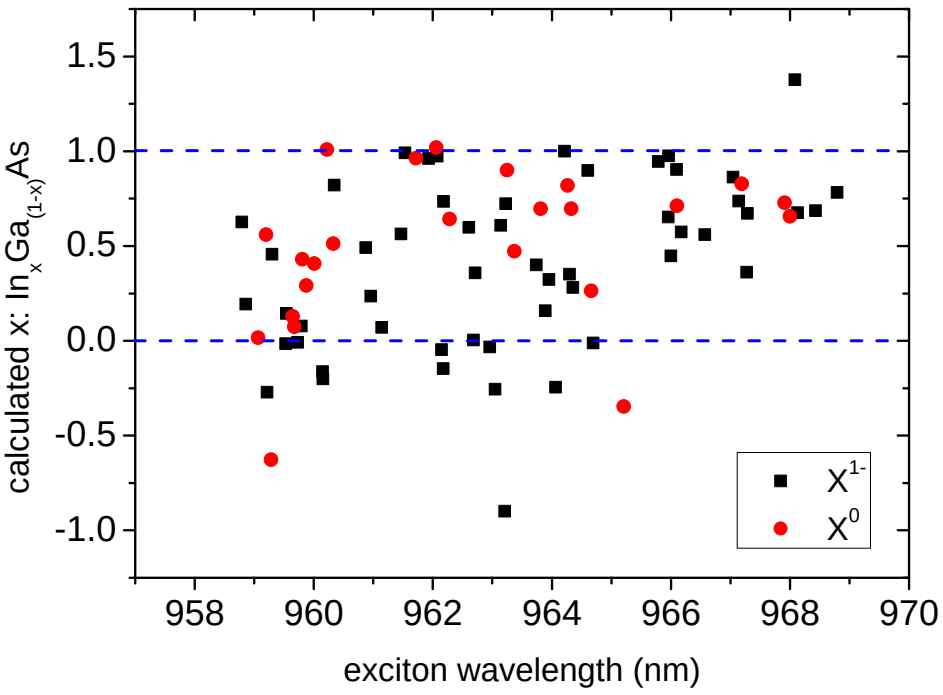

Figure 3.8: Plot of calculated compositions of 77 exciton lines from PCI QDs. The blue dashed lines mark the limits of allowed physical values. The existence of points outside these limits demonstrates the fact that this approach is too simplistic to account for the exciton tuning behaviour.

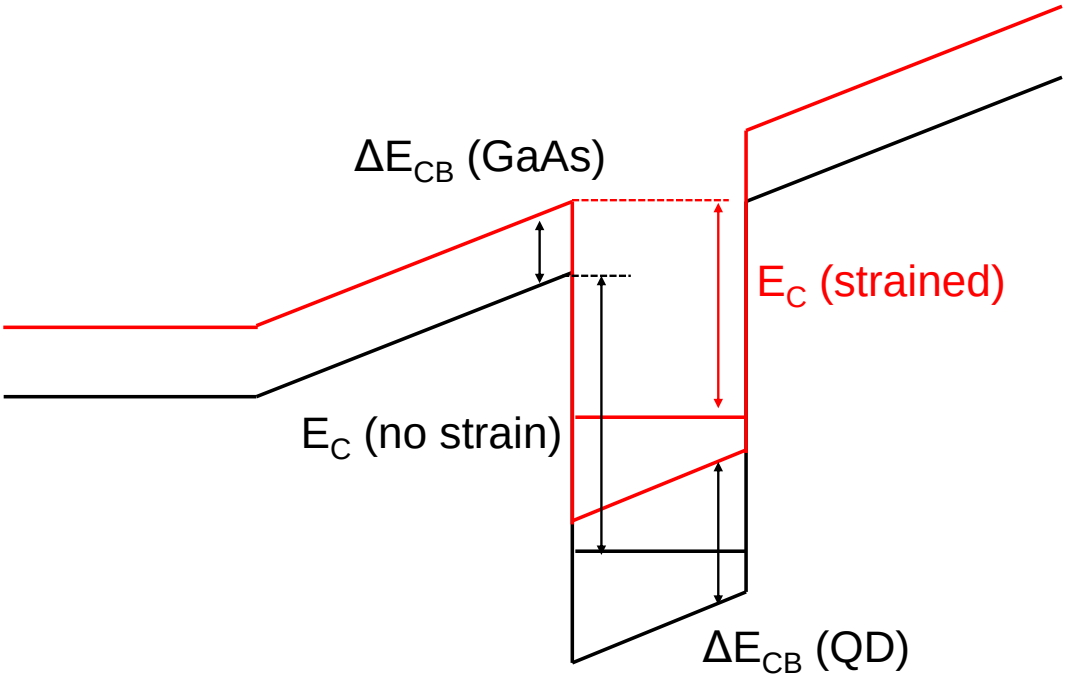

Figure 3.9: Conduction band diagram with zero applied strain (black) and applied strain (red). The effect of strain tuning the conduction band via deformation potentials on the electron confinement energy E_C is given by the difference of the QD and GaAs tunnel barrier conduction band shifts ΔE_{CB}, resulting in Eq. 3.10.

will only make these value smaller: since

$$dE_C/dp = (dE_{CB}/dp)_{QD} - (dE_{CB}/dp)_{GaAs} \tag{3.10}$$

where dE_C/dp is the electron confinement energy tuning, it is clear using values from Table 3.2 that $dE_C/dp \leq (dE_{CB}/dp)_{QD}$.

In reality, the tuning of confinement energies due to uniaxial stress depends on a number of effects resulting from the stress applied:[3]

Hydrostatic strain:

This affects electron and hole states, and is covered above.

Biaxial strain:

This affects predominately hole states, and is covered above.

Change of QD height:

Compressive (tensile) uniaxial stress applied to a QD will have a increase (decrease) the height of the QD, decreasing (increasing) the single particle confinement energies. As such, the single particle confinement and therefore exciton energies are strongly dependent on the initial shape of the QD. This

is not covered by this simple model, and goes some way to explaining the distinct difference between tuning behaviours for different types of QD shown in Fig. 3.1.

Shift of confinement potential:

The simple treatment above assumes that the confinement energies of the single particles will shift with the confining potential due to the band mismatch in the heterostructure: i.e. as the conduction band shifts with applied stress, the electron energy level will remain a fixed energy above the bottom of the conduction band. In reality, this is not the case, and the electron energy levels within the confining potential are dependent on the depth of the confining potential. This means that Eq. 3.10 is incomplete: in fact, according to Ref. [3], $E_C \propto V^2$, where V is the depth of the QD potential.

This all demonstrates that simply considering deformation potentials to estimate the composition of a QD does not work, and the model must be refined to take into account the third and fourth factors outlined above.

3.5 FSS tuning

The biexciton-exciton-ground cascade in QDs is a potential source of polarisation-entangled photons. The cascade can occur through two different paths: via two orthogonal X^0 states. If these intermediate X^0 states are degenerate, the cascade results in the emission of two circularly-polarised entangled photons in the state $1/\sqrt{2}\,(|R_1L_2\rangle + |L_1R_2\rangle)$, where R and L are right- and left-hand polarised photons respectively. However, the electron-hole exchange interaction in low-symmetry QDs splits the X^0 states into two non-degenerate states with different linear polarisations (Fig. 3.10 (a)). The energy difference between the two is the FSS. Using polarisation-resolved PL, it is possible to resolve the two peaks by an oscillation of the X^0 line in energy with polarisation angle, and thus determine the value of the FSS (example spectra in Fig.3.10 (a)).

Measurements of FSS were made on the two DWELL samples: one in bulk and one with strain and charge tuning. Combining the statistics of the measured FSS from both samples, we see a full range of FSS between 16 and 136 μeV for 76 measured QDs (Fig. 3.10 (b)). This range of FSS is considerably smaller than previous reports on FSS for QDs emitting at similar wavelengths [13, 14, 15], an important result as a smaller initial FSS requires more modest external fields for complete cancellation. We do not observe a clear correlation between the emission wavelength and the FSS as has been observed for both strained [16] and unstrained [17, 18, 19] QDs at shorter emission wavelengths. For unstrained QDs, increasing FSS was observed as the QD size increased and generally attributed to dot morphology as larger QDs have increased shape anisotropy. One signature of strong

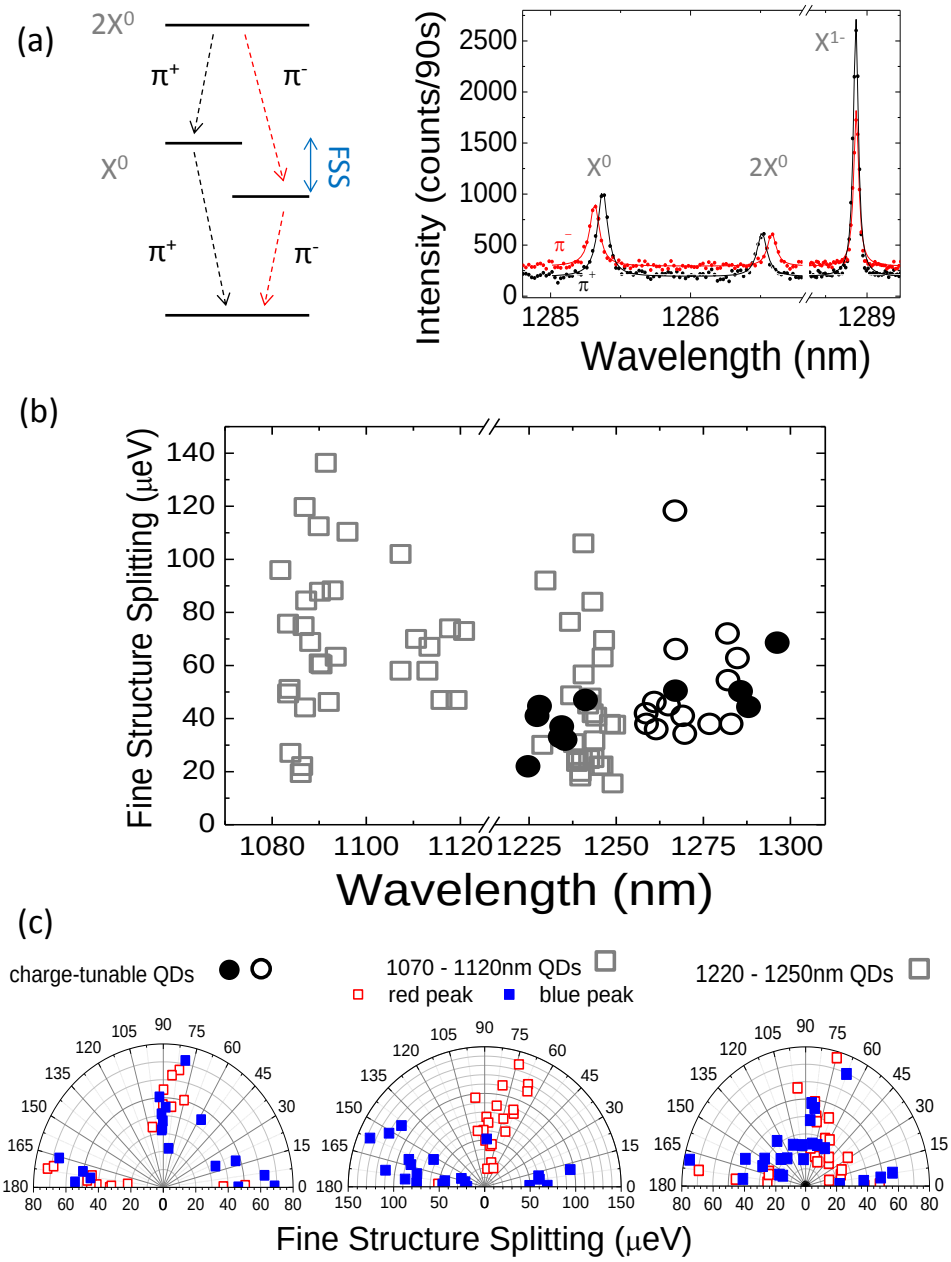

Figure 3.10: (a) Left: schematic of the biexciton (XX)-to-exciton (X^0)-to-vacuum state transitions and their respective polarisations (π^+ or π^-). Right: An example of PL spectra at orthogonal polarisations, showing the X^0, XX and X^{1-} emission lines (full symbols) and Lorentzian fits (solid lines). (b) FSS measured on single QDs with no applied external strain. Circles: charge tunable device (filled: 12 QDs in Table 3.3), open squares: DWELL QDs in bulk. (c) Polarisation angle of the short (blue) and long (red) wavelength peak with respect to the [110] crystallographic axis for X^0.

shape anisotropy is preferential alignment of the polarization axes of the FSS with a crystallographic direction. Therefore, in Fig. 3.10 (c) we present the polarization angles of the high and low-energy FSS peaks for the QDs we measured. We observe that QDs at all wavelengths in the charge tunable device and QDs at shorter wavelengths in the bulk sample tend to align along the crystallographic axes, whereas longer wavelength QDs in the bulk sample display more random FSS polarization orientations.

We next apply an external uniaxial strain and find that the FSS can be manipulated in a reversible way and that significant reductions of the FSS can be achieved (see Figs. 3.6 (f) and 3.11). For the PCI QDs, the rate of FSS tuning with strain $d\text{FSS}/dS$ quantitatively agrees with theoretical predictions. [20] The maximum FSS tuning range observed for QDs investigated in our experimental setup is $\approx$ 28 µeV and we can observe QDs for which the FSS vanishes within the resolution limit (e.g. QD 1 at $V_{PZT} = +300$ V in Fig. 3.2).

FSS tuning was investigated in more detail on the DWELL QDs. Table 3.3 summarizes the results from 12 single DWELL QDs. We observe tuning ranges (Δ FSS) from 8.3 to 46.4 μeV, slopes ranging from -0.074 to 0.077 $\mu\text{eV}/\text{V}_{PZT}$, and blueshifts of the emission energy ΔE of $\sim$ 1 meV for increasing tensile strain. In Fig. 3.11 (a), we show a polar plot for the two orthogonally polarized exciton lines for QD10. As shown, going from -300 to +300 V_{PZT}, the alignment of the polarization angle θ with respect to the [110] axis only varies by a few degrees, a typical result in experiments on DWELL QDs. While most of the QDs under study show a linear dependence of the FSS as a function of the applied strain (see Fig. 3.11 (b) left panel), for QD2 we observe a parabolic modification of the FSS which reaches a minimum (FSS_{min}^{exp}) of 22.4 $\pm$ 2.2 μeV (see Fig. 3.11 (b) right panel).

The application of uniaxial strain is expected to modify the FSS in a quadratic way, with the minimum of the parabola representing the minimal FSS that is reachable for a specific QD [21, 22]. The critical stress required to reach the minimum FSS depends on the shape and composition of each specific QD [4, 20]. If p_c is not experimentally reachable, one observes a linear response with either positive or negative tuning slopes, depending on which arm of the parabola is probed (see Fig. 3.11 (b)). The realization of a larger strain range would enable the minimum of the parabola to be reached for each dot.

The FSS is a result of the asymmetric confining potential of the carriers trapped within the quantum dot. This symmetry lowering can be attributed to different factors: shape anisotropy, the presence of piezoelectric fields (due to strain from the different lattice constants of the materials composing the QD structure that separates negative and positive charge centers), and different interface potentials (due to differences in the interfaces at the atomistic level). This last effect is related to the position of the atoms in the nanostructure and, therefore, is the most sensitive

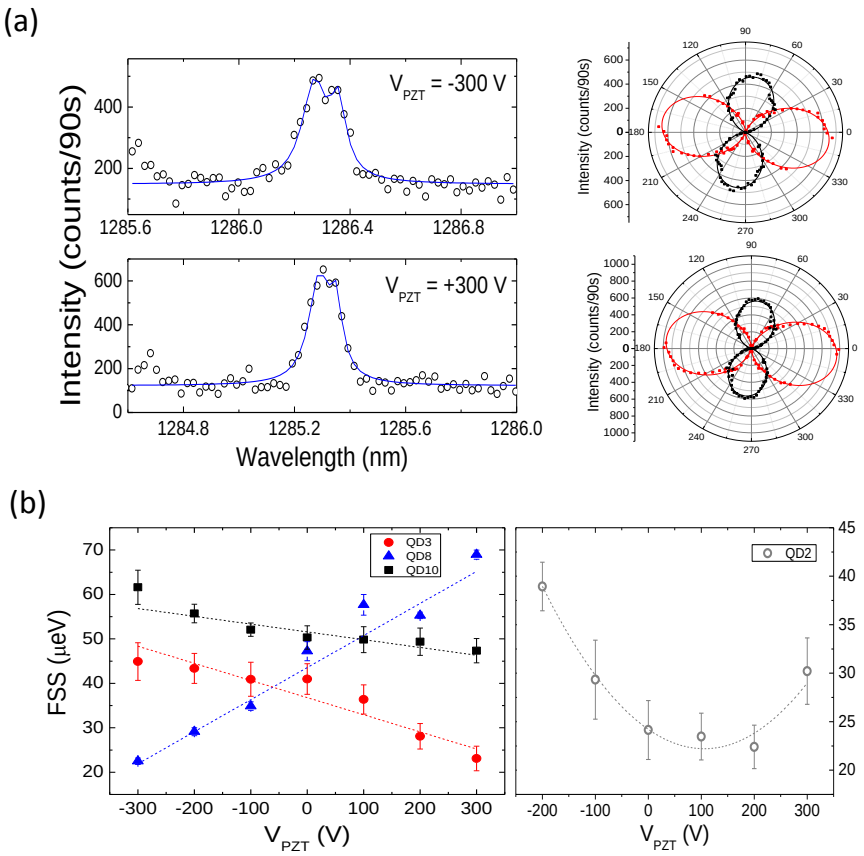

Figure 3.11: (a) Left panel: Example results of the manipulation of the X^0 FSS (from 61.6 to 47.3 μeV) of QD10 with uniaxial strain. The solid lines are double Lorentzian fits to the data, collected at a polarisation angle of $\sim$45° (open circles). Right panel: Two examples of polar plots for the two orthogonal exciton lines at V_{PZT} = -300, +300 V. The solid lines are fits to the data. (b) FSS as a function of applied voltage on the PZT stack for four different single QDs. The error bars are the standard deviation from the mean value of the FSS, obtained from 43 fits to the experimental spectra collected as a function of polarisation angle ranging between 0° and 140°. The dashed lines in the left (right) panel are linear (quadratic) fits to the data.

Table 3.3: Strain tuning of single QDs. The FSS slope is the result of a linear fit of the FSS splitting in the full V_{PZT} range, except for QDs 2, 9, 12 where only the points in the linear regime were fitted (see Fig. 3.11). The angle θ represents the polarization angle of the low energy peak with respect to the [110] crystallographic axis. FSS_{min}^{exp} is the minimal value of FSS that we measure in our experiments. $2|\delta|$ and $2|\kappa|$ refer to the diagonal and off-diagonal lower bounds for FSS, respectively. (Note that 1 V_{PZT} = 46 KPa.)

QD (#)	$FSS_{V_{PZT}=0}$ (μeV)	FSS slope (μeV/V_{PZT})	Δ FSS (μeV)	FSS_{min}^{exp} (μeV)	$\theta_{V_{PZT}=0}$ (°)	$2\|\delta\|$ (μeV)	$2\|\kappa\|$ (μeV)
1	45.2±2.1	0.015	8.3	35.7±0.8	83.6	44.1±2.3	10.0±0.5
2	23.5±2.4	-0.074	15.1	20.1±1.1	-5.0	23.1±2.3	4.1±0.5
3	41.0±3.4	-0.036	21.8	23.1±1.4	-2.3	40.9±3.4	3.3±0.3
4	46.0±5.9	-0.022	12.4	37.5±2.6	-2.9	45.8±5.9	4.6±0.6
5	39.5±1.1	0.026	15.6	28.9±0.6	-0.1	39.5±1.1	0.1±0.0
6	34.4±0.9	0.024	13.0	29.3±0.6	0.8	34.4±0.9	1.0±0.0
7	32.2±0.7	0.022	13.8	21.5±0.6	-1.5	32.2±4.7	1.7 ±0.0
8	47.2±2.1	0.077	46.4	22.5±0.4	-4.7	46.6±2.1	7.7±0.1
9	49.7±5.1	0.051	19.9	49.0±2.6	1.3	49.6±5.1	2.3±0.2
10	50.3±2.6	-0.021	14.2	47.3±1.4	75.2	43.7±2.6	24.8±0.3
11	47.2±1.2	-0.017	10.3	39.1±1.0	-8.6	45.1±1.1	14.0±0.4
12	68.6±2.5	-0.024	11.1	63.3±1.7	-9.9	64.5±2.4	23.2±0.8

to applied strain. As shown in Refs. [4] and [20], the application of external strain does not change the macroscopic shape of the quantum dot considerably (less than 0.2%). Also, piezoelectricity seems to have a marginal effect in the theoretical evaluation of the FSS under strain [20]. Hence, we conclude that the experimental results revealing very different dependencies for the FSS on the applied strain for each dot are caused by uniqueness at the atomistic level. The fact that FSS_{min}^{exp} agrees with the results of the model of Ref. [20] (see Table 3.3 and discussion below) further supports these conclusions.

The behavior of the FSS under uni-axial strain can be understood using the basic picture presented in Ref. [20]. Using the same notation, the effective bright exciton Hamiltonian reads $H = (\delta + \alpha p/2)\sigma_z + (\kappa + \beta p)\sigma_x$, where p is the external stress, α, β, κ and δ are empirical parameters that depend strongly on the microscopic structure of the QDs, and σ_x,σ_z are the Pauli matrices. The FSS then reads as

$$\Delta = \sqrt{4(\beta p + \kappa)^2 + (\alpha p + 2\delta)^2} \tag{3.11}$$

Generally, for stress along either [110] or [1$\bar{1}$0] direction, $\alpha \neq 0$ and $\beta = 0$ (see Table 1 in Ref. [20]) and the lower bound of FSS can be reached when the diagonal elements are removed, i.e., $\delta + \alpha p/2 = 0$. We call this lower bound $\Delta_{min} = 2|\kappa|$ the "off-diagonal lower bound". For stress along [100] or [010] direction, the lower bound of FSS can be reached when the off-diagonal elements are removed, $\kappa + \beta p = 0$, and

we call this lower bound $\Delta_{min} = 2|\delta|$ the "diagonal lower bound". The lower bound of FSS can thus be predicted using the FSS Δ (labeled $\mathrm{FSS}_{V_{PZT}=0}$ in Table 3.3) and polarization angle θ at zero bias using

$$\delta = \Delta \cos(2\theta)/2, \quad \kappa = -\Delta \sin(2\theta)/2 \tag{3.12}$$

Here we compare our results to this phenomenological model. FSS_{min}^{exp} and the predicted diagonal ($2|\kappa|$) and off-diagonal ($2|\delta|$) lower bounds are presented in Table 3.3. Note that the minimum of the parabola is reached for QD2 only, therefore the other values reported do not represent the minimal achievable FSS for the QDs under study, but the minimal FSS achieved under the current experimental conditions. In general, we find $\mathrm{FSS}_{min}^{exp} > 2|\kappa|$ as expected due to $|p_c|$ exceeding maximum range of the experimentally applied stress (Fig. 3.12). Additionally, there might be a non-uniformity of the external stress in the experiment that results in the applied strain not exactly oriented along the [110] or [1$\bar{1}$0]. In this scenario, $\alpha \neq 0$ and $\beta \neq 0$ and one expects $2|\delta| > \mathrm{FSS}_{min}^{exp} > 2|\kappa|$. Notably, applying additional stress along [100] components can further reduce the FSS and the application of two independent external stress is expected to cancel the FSS [23].

QDs with θ aligned along the [110] or [100] directions are expected to reach the smallest FSS when an external stress is applied [20]. In contrast to shorter wavelength ($\sim$ 950 nm) smaller QDs whose alignment is more random [24], we observe that the long wavelength charge-tunable QDs measured here are well aligned with the [110] axis (see Fig. 3.10 (c) and Table 3.3). No post selection has been done to select QDs better aligned to the crystallographic axis. In fact, for QDs 5 and 6 in Table 3.3, $2|\kappa| \leq 1\mu$eV, the typical transform limited linewidth for self-assembled QDs (see also Fig. 3.12). This is significant: with a larger strain tuning range, entangled photon pair generation at telecom wavelength should be possible. For QDs in which $2|\kappa| > 1$ μeV, a second external field will allow complete cancellation of the FSS [22, 23]. The small rotations of θ shown in Fig. 3.11 (a) are expected when the FSS varies linearly with the applied strain. We also note that for QD2 the rotation of θ is still limited to $\sim 5°$, even though the minimal FSS is reached. Polarization rotations smaller than the ones reported in References [21] and [22] have been predicted for QDs with different shapes and composition [20, 4]. One possible explanation for the experimental observation of limited θ rotation for QD2 is that the deep confinement potential of the telecom wavelength QDs reduces penetration of the carrier wavefunctions into the barrier material, leading to reduced sensitivity to the QD environment (e.g. alloy disorder at the interface) [25, 26] and, therefore, less pronounced rotations of θ. Further investigation is required to correlate the dot's morphology with the FSS and θ. One promising approach based on the statistical trends of an ensemble of dots has recently been developed and applied to shorter wavelength QDs [27].

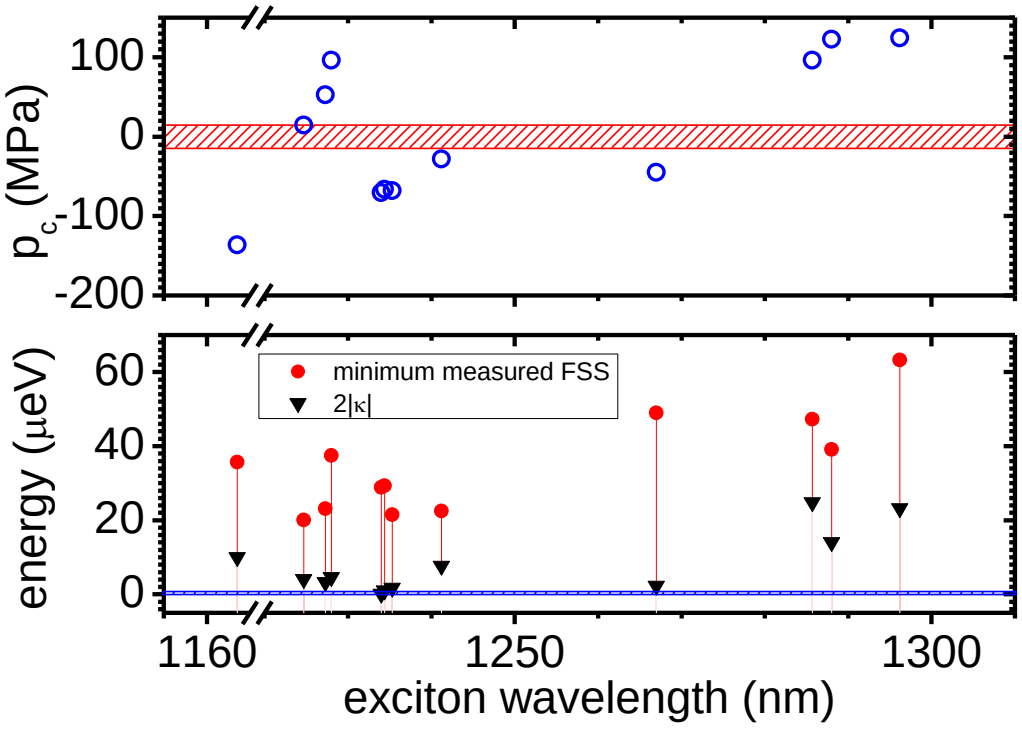

Figure 3.12: Top: plot of critical stress calculated for the 12 QDs in Table 1.3. The red shaded region is the available range of uniaxial strain in this set-up. Most QD lie outside this range, but one is within, representing the one QD whose FSS tunes to a minimum. Bottom: plot of minimum measured FSS (red circles) and $2|\kappa|$ for the same 12 QDs. The blue region is the region in which the FSS can be considered "cancelled", determined by the linewidth. 2 QDs show values of $2|\kappa|$ within this region, and thus could be tuned to zero FSS given a larger strain range. The other QDs require a second tuning method.

3.6 Summary

In summary, strain tuning was used in conjunction with charge tunability to reversibly tune the energies of excitons, single particles and FSS in self-assembled QDs at around 950nm and 1300nm. Firstly, strain is shown to affect the energies of excitonic transitions in a way that is highly dependent on the microscopic properties of the individual QD. While different QD growth processes will result in very different overall properties of the ensemble of QDs, these properties will still vary to a large extent within the same sample, due to the Stranski-Krastinov process resulting in randomly distributed sizes, shapes and compositions. This difference in behaviour between QDs on the same chip could be used to tune adjacent QDs in the same focus spot into resonance, potentially allowing generation of indistinguishable photons to generate entangled photons or spins [28], and allowing the investigation of superradiance from adjacent emitters.

Secondly, by probing the behaviour of single particles in QDs via a perturbative Coulomb blockade model, the effect of strain on single particle energies is shown to be ~ 50 times larger than its effect on the exciton energies. The effect on excitons is a result of a near-cancellation of the tuning of electrons and holes in the QD due to the opposite response of the single electron and hole states, explaining why the resulting exciton behaviour varies substantially within the dot population: the relative magnitudes of the strain tuning of single electrons and holes (and hence the exciton) are determined by each individual dot's inherent size, shape, and composition. Information about the electron confinement energy with strain in conjunction with knowledge of the deformation potentials for the conduction band in InAs and GaAs is not sufficient to make a non-destructive estimate of the In/Ga composition of a given QD. The QD's size and shape have to be taken into account. If these could be incorporated into a refined model involving deformation potentials, it would have the potential to be an extremely useful tool in probing and designing quantum structures. [29, 30]

Thirdly, polarisation-resolved PL allows the FSS of the neutral exciton of a QD and its tuning with strain to be measured. The DWELL QDs emitting in the 1100-1300nm regime show a lower mean and minimum nominal FSS than previously measured in the literature: nominal FSS of neutral exciton lines down to 16 μeV are observed, which is a good starting point for strain tuning to zero FSS. Both DWELL QDs and PCI QDs emitting at 950nm show a predominately linear tuning with strain, with one PCI QD shown with vanishing FSS and on DWELL QD coming to a minimum. Again this tuning is highly dependent on the morphology of the QD, so each QD measured behaves slightly different under strain. However, it is apparent that the scheme used to apply strain to the QDs is not sufficient to be able to tune all QDs to zero: while almost all QDs measured have p_c outside the available range, so that the FSS can be effectively cancelled for some QDs investigated here assuming

a larger strain range, thus enabling deterministic entangled photon pair generation at telecom wavelengths, most will also need another "dimension" of tuning to be completely cancelled rather than come to a non-zero minimum, whether through a larger external electric field than can be applied in this set-up, or via strain applied in a second direction.

3.7 References

[1] Kuklewicz, C. E., Malein, R. N. E., Petroff, P. M. & Gerardot, B. D. Electro-Elastic Tuning of Single Particles in Individual Self-Assembled Quantum Dots. *Nano Lett.* **12**, 3761 (2012).

[2] Sapienza, L. *et al.* Exciton fine-structure splitting of telecom-wavelength single quantum dots: Statistics and external strain tuning. *Phys. Rev. B* **88**, 155330 (2013).

[3] Jöns, K. D. *et al.* Dependence of the Redshifted and Blueshifted Photoluminescence Spectra of Single $In_xGa_{1-x}As$/GaAs Quantum Dots on the Applied Uniaxial Stress. *Phys. Rev. Lett.* **107**, 217402 (2011).

[4] Singh, R. & Bester, G. Lower Bound for the Excitonic Fine Structure Splitting in Self-Assembled Quantum Dots. *Phys. Rev. Lett.* **104**, 196803 (2010).

[5] Seidl, S. *et al.* Absorption and photoluminescence spectroscopy on a single self-assembled charge-tunable quantum dot. *Phys. Rev. B* **72**, 195339 (2005).

[6] Warburton, R. J. *et al.* Coulomb interactions in small charge-tunable quantum dots: A simple model. *Phys. Rev. B* **58**, 16221 (1998).

[7] Dalgarno, P. A. *et al.* Coulomb interactions in single charged self-assembled quantum dots: Radiative lifetime and recombination energy. *Phys. Rev. B* **77**, 245311 (2008).

[8] Fry, P. W. *et al.* Inverted Electron-Hole Alignment in InAs-GaAs Self-Assembled Quantum Dots. *Phys. Rev. Lett.* **84**, 733 (2000).

[9] Warburton, R. J. *et al.* Giant permanent dipole moments of excitons in semiconductor nanostructures. *Phys. Rev. B* **65**, 113303 (2002).

[10] Wang, J., Guo, G.-C. & He, L. Theory of strain tuning fine structure splitting in self-assembled InAs/GaAs quantum dots. *J. Phys.: Condens. Matter* **26**, 475301 (2014).

[11] Vurgaftman, I., Meyer, J. R. & Ram-Mohan, L. R. Band parameters for IIIV compound semiconductors and their alloys. *Journal of Applied Physics* **89**, 5815 (2001).

[12] Zhou, S., Liu, Y., Lu, P., Han, L. & Yu, Z. The Formation Site of Noninterfacial Misfit Dislocations in InAs/GaAs Quantum Dots. *Journal of Nanomaterials* **2014**, 103640 (2014).

[13] Cade, N. I., Gotoh, H., Kamada, H., Nakano, H. & Okamoto, H. Fine structure and magneto-optics of exciton, trion, and charged biexciton states in single InAs quantum dots emitting at 1.3 μm. *Phys. Rev. B* **73**, 115322 (2006).

[14] Ward, M. B. *et al.* Biexciton cascade in telecommunication wavelength quantum dots. *J. Phys.: Conf. Ser.* **210**, 012036 (2010).

[15] Tartakovskii, A. I. *et al.* Exciton fine structure splitting in dot-in-a-well structures. *Applied Physics Letters* **88**, 131115 (2006).

[16] Seguin, R. *et al.* Size-Dependent Fine-Structure Splitting in Self-Organized InAa/GaAs Quantum Dots. *Phys. Rev. Lett.* **95**, 257402 (2005).

[17] Abbarchi, M. *et al.* Exciton fine structure in strain-free GaAs/$Al_{0.3}Ga_{0.7}$As quantum dots: Extrinsic effects. *Phys. Rev. B* **78**, 125321 (2008).

[18] Abbarchi, M. *et al.* Fine structure splitting of quantum dot excitons: Role of geometry and environment. *Physica E: Low-dimensional Systems and Nanostructures* **42**, 881 (2010).

[19] Plumhof, J. D. *et al.* Experimental investigation and modeling of the fine structure splitting of neutral excitons in strain-free GaAs/Al_xGa_{1-x}As quantum dots. *Phys. Rev. B* **81**, 121309 (2010).

[20] Gong, M., Zhang, W., Guo, G.-C. & He, L. Exciton Polarization, Fine-Structure Splitting, and the Asymmetry of Quantum Dots under Uniaxial Stress. *Phys. Rev. Lett.* **106**, 227401 (2011).

[21] Bennett, A. J. *et al.* Electric-field-induced coherent coupling of the exciton states in a single quantum dot. *Nat Phys* **6**, 947 (2010).

[22] Trotta, R. *et al.* Universal Recovery of the Energy-Level Degeneracy of Bright Excitons in InGaAs Quantum Dots without a Structure Symmetry. *Phys. Rev. Lett.* **109**, 147401 (2012).

[23] Wang, J., Gong, M., Guo, G.-C. & He, L. Eliminating the fine structure splitting of excitons in self-assembled InAs/GaAs quantum dots via combined stresses. *Applied Physics Letters* **101**, 063114 (2012).

[24] Seidl, S. *et al.* Statistics of quantum dot exciton fine structure splittings and their polarization orientations. *Physica E: Low-dimensional Systems and Nanostructures* **40**, 2153 (2008).

[25] Mlinar, V. & Zunger, A. Effect of atomic-scale randomness on the optical polarization of semiconductor quantum dots. *Phys. Rev. B* **79**, 115416 (2009).

[26] Luo, J.-W., Singh, R., Zunger, A. & Bester, G. Influence of the atomic-scale structure on the exciton fine-structure splitting in InGaAs and GaAs quantum dots in a vertical electric field. *Phys. Rev. B* **86**, 161302 (2012).

[27] Gong, M. *et al.* Statistical properties of exciton fine structure splitting and polarization angles in quantum dot ensembles. *Phys. Rev. B* **89**, 205312 (2014).

[28] Patel, R. B. *et al.* Two-photon interference of the emission from electrically tunable remote quantum dots. *Nat Photon* **4**, 632 (2010).

[29] Mlinar, V. *et al.* Structure of quantum dots as seen by excitonic spectroscopy versus structural characterization: Using theory to close the loop. *Phys. Rev. B* **80**, 165425 (2009).

[30] Chekhovich, E. A. *et al.* Structural analysis of strained quantum dots using nuclear magnetic resonance. *Nat Nano* **7**, 646 (2012).

Chapter 4

Resonance fluorescence

4.1 Introduction

In this chapter, I will cover the results of resonance fluorescence (RF) experiments carried out on InGaAs QDs emitting in the 950nm region. First, I will give the motivation for carrying out RF with these QDs followed by a summary of the Mollow model that arises from a two-level system interacting with a strong light field, with special regard given to the relationship between elastically and inelastically scattered light. I will then experimentally investigate the elastically and inelastically scattered spectra from QDs under various conditions to characterise the dephasing caused by environmental noise due to two factors: a fluctuating charge environment and nuclear spins. Examples of FPI spectra showing the effects of these noise sources are shown in Fig. 4.1.

I will show that the fluctuating magnetic field due to nuclear spins (the Overhauser field) in the QD results in inelastic Raman scattering that is broadened over experimental timescales with an ensemble dephasing lifetime T_{2S}^{*}, which reduces the ratio of elastic to inelastic scattering.

Charge noise has a much larger effect on fluorescence than it does on elastic Rayleigh scattering, so it has a negligible effect well below saturation. Above saturation it leads to spectral diffusion over experimental timescales, broadening the inelastic fluorescence component of the spectrum with an ensemble dephasing lifetime T_{2C}^{*}.

Hong-Ou-Mandel (HOM) measurements were made to measure the indistinguishability of photons emitted from the QD. To obtain high visibility of the HOM effect, measurements are taken below saturation power to ensure a high elastic to inelastic ratio. Above saturation, charge noise increases the ratio of elastic to inelastic scattering but in this power regime indistinguishability has been ruined by the appearance of the Mollow triplet. Below saturation, charge noise has little effect on indistinguishability. Nuclear spin noise becomes the limiting factor, and this can be mitigated by applying an external magnetic field which is strong relative to the

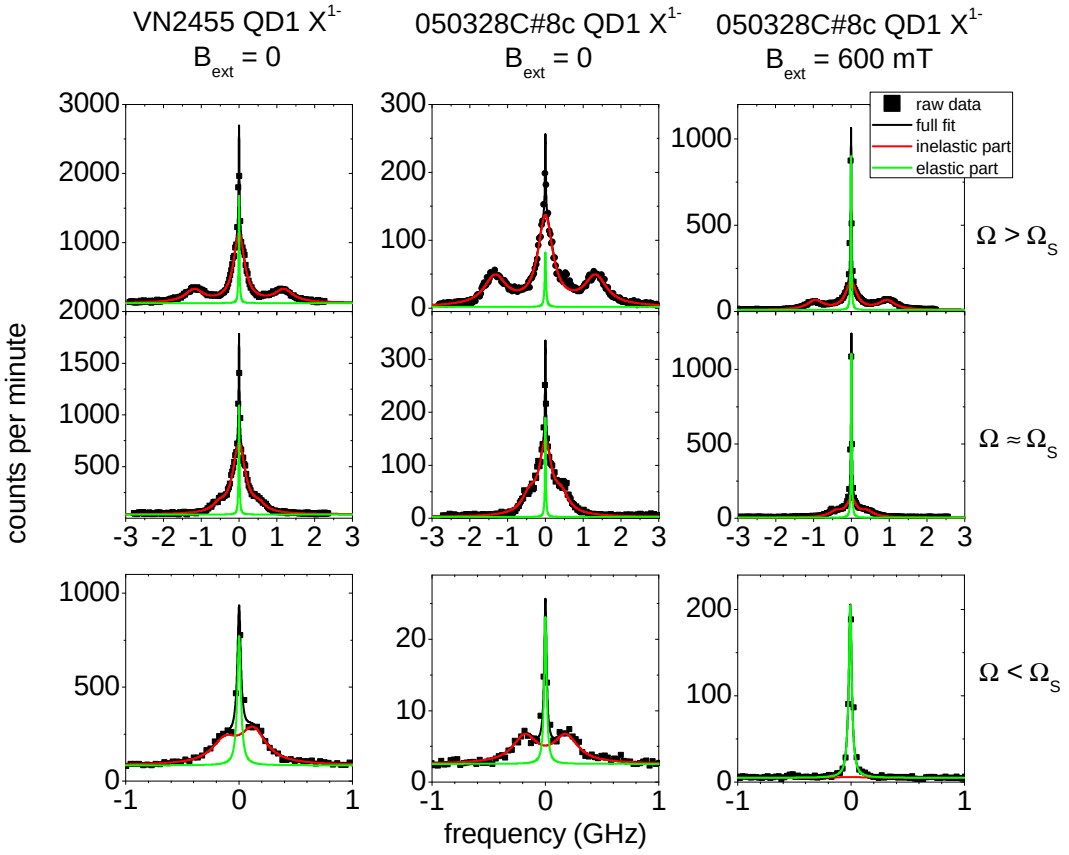

Figure 4.1: Examples of Fabry-Perot interferometer spectra for X^{1-} from QDs from samples 050328C#8c and VN2455 and X^0 from sample 050328C#8c, above, around and below saturation Rabi frequency Ω_S. These spectra demonstrate some of the noise effects that I will be covering in this chapter, such as the smeared-out Mollow sidebands for the planar cavity sample due to charge noise, the low power doublet arising from the effects of fluctuating nuclear spins in the X^{1-} spectra, and the increased contribution of elastic scattering in the X^0 spectra where charge noise is increased and nuclear spin fluctuations do not affect the low power spectrum.

nuclear spin Overhauser field in the Faraday geometry. This drastically reduces the amount of Raman scattering, improving the indistinguishability.

4.2 Background and Motivation

4.2.1 Resonance fluorescence

RF allows the direct excitation of the desired state in a QD, and can thus be used for spin initialisation[1, 2], manipulation or read-out[3]. In addition, RF can be used to generate highly coherent single, indistinguishable photons[4, 5]. It is better to use RF to generate indistinguishable photons than using non-resonant photoluminescence (PL), as in PL, the electron-hole pair that is generated by the incoming photon is prepared in an excited state, and must non-radiatively decay to a ground state before recombining to emit a photon. The ratio of this finite lifetime of the non-radiative decay to the radiative lifetime of the exciton limits the indistinguishability of the photons emitted.[6]. In addition, a large degree of highly coherent elastically scattered photons can be produced through RF, which is not possible via PL.

If a QD is modelled as a 2-level system, when excited by a resonant laser, light from the QD can be emitted via one of two mechanisms: in one, fluorescence, the QD absorbs the photon, raising the QD from the ground state to the excited state, which then decays with its characteristic lifetime T_1 to emit a photon. In this case, the emission time is determined by the lifetime of the QD state T_1, pure dephasing (loss of coherence without recombination) in the exciton (with associated lifetime T_2^*), and the excitation power (represented by the Rabi frequency of the transition $\Omega = \vec{\mu} \cdot \vec{E}/\hbar$, where $\vec{\mu}$ is the transition dipole moment and $\vec{E}$ is the electric field vector). The linewidth of the emission is broadened:

$$\text{FWHM} = 2\frac{1}{T_2}\sqrt{1 + \frac{T_1}{T_2}\Omega^2} \tag{4.1}$$

$$\frac{1}{T_2} = \frac{1}{2T_1} + \frac{1}{T_2^*} \tag{4.2}$$

The other emission mechanism is elastic Rayleigh scattering, which is where a photon close to resonance with a transition is scattered by the transition with no change in its energy or coherence. The emitted photon keeps the characteristics of the excitation laser, such as wavelength and coherence time. While the linewidth of the scattered photon is inherited from the laser photon and is thus generally much smaller than the linewidth of the incoherent fluorescence (ignoring dephasing for simplicity, $1/T_1$), this scattering is still a fluorescence lifetime-limited process, as second order coherence $g^2(t)$ of Rayleigh scattering from an excitonic transition shows an antibunching dip at $t = 0$ with a width on the order of $1/T_1$. [7]

Above saturation power, the states in a two-level systems like the excitons in a

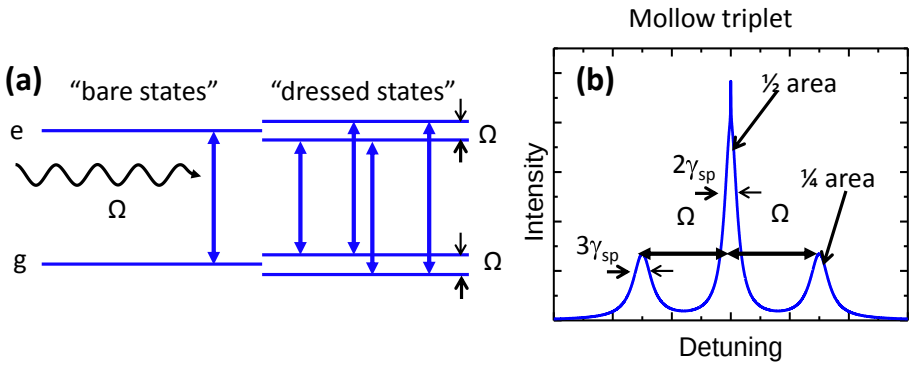

Figure 4.2: (a) Energy level diagram showing hybridisation of a "bare" two level system $g \leftrightarrow e$ with a strong laser field of Rabi frequency Ω, producing "dressed" states separated by Ω. (b) spectrum of the Mollow triplet produced from the 4 transitions between dressed states, with proportional linewidths and peak areas. The Rayleigh scattering peak is not shown here.

QD hybridise with the light field to form "dressed states" as in Fig. 4.2 (a). This results in 4 possible radiative transitions, two of which are degenerate. According to Mollow's theory[8], the spectrum is composed of the narrow Rayleigh peak, along with the incoherent Mollow triplet of one tall central peak with two sidebands split from the central peak by the Rabi energy – three Lorentzian peaks whose heights, full widths at half maximum (FWHM) and areas have strict ratios, as in Fig. 4.2 (b): the central peak height is three times that of the sidebands, its FWHM is 2/3 that of the sidebands, resulting in the central peak area being twice that of one sideband peak, and so half of the total incoherent emission is in the central peak. Mollow gives a formula[8] for the resonant spectrum of a two-level system under strong excitation (i.e. Rabi frequency greater than linewidth):

$$\begin{aligned} S(\nu, \Delta\nu, \Omega) = {} & 2\pi|\alpha_\infty|^2\delta(\omega-\nu-\Delta\nu) \\ & + \frac{n_\infty \kappa \Omega^2}{\Omega'^4}\left(\frac{\frac{1}{2}\Omega^2}{(\omega-\nu-\Delta\nu)^2+s_0}\right. \\ & + \left(\frac{3}{8}\Omega^2+\frac{1}{4}(\Delta\nu)^2\right) \\ & \left.\times\left(\frac{1}{(\omega-\nu-\Omega')^2+\sigma^2}+\frac{1}{(\omega-\nu+\Omega')^2+\sigma^2}\right)\right) \end{aligned} \tag{4.3}$$

where

$$|\alpha_\infty|^2 = \frac{\frac{1}{4}\Omega^2\left(\frac{1}{4}\kappa^2 + (\Delta\nu)^2\right)}{\left(\frac{1}{2}\Omega^2 + (\Delta\nu)^2 + \frac{1}{4}\kappa^2\right)^2} \tag{4.4}$$

$$n_\infty = \frac{\frac{1}{4}\Omega^2}{\frac{1}{2}\Omega^2 + (\Delta\nu)^2 + \frac{1}{4}\kappa^2} \tag{4.5}$$

$$s_0 = -\frac{1}{2}\frac{\Omega^2 + 2(\Delta\nu)^2}{\Omega^2 + (\Delta\nu)^2} \tag{4.6}$$

$$\sigma = -\kappa\frac{\frac{3}{4}\Omega^2 + \frac{1}{2}(\Delta\nu)^2}{\Omega^2 + (\Delta\nu)^2} \tag{4.7}$$

$$\Omega' = \sqrt{\Omega^2 + (\Delta\nu)^2} \tag{4.8}$$

ω is the resonance position of the exciton line, $\Delta\nu$ is the detuning of the laser from resonance, κ is the linewidth of the inelastic transition and Ω is the Rabi frequency. Note that this model does not take into account pure dephasing: $1/T_2^* = 0$, so $\kappa = 2/T_2 = 1/T_1$.

Since the Mollow sidebands shift outwards from the central emission peak with increased Rabi frequency, it is clear that in order to generate highly indistinguishable photons, the excitation power must be kept below saturation. Keeping the excitation power low also has the effect of increasing the ratio of elastically scattered photons to total emitted photons (known hereafter as the "elastic ratio" or ER)[7].

Taking into account pure dephasing ($1/T_2^* \neq 0$, $T_2 < 2T_1$), the coherence term α_∞ and upper state population n_∞ (given above by Eqs. 4.4 and 4.5) can be written in terms of T_1 and T_2 [9]:

$$|\alpha_\infty|^2 = \frac{\frac{1}{4}\Omega^2\left(\frac{1}{T_2^2} + (\Delta\nu)^2\right)}{\left(\frac{T_1}{T_2}\Omega^2 + (\Delta\nu)^2 + \frac{1}{T_2^2}\right)^2} n_\infty \qquad = \frac{\frac{T_1}{2T_2}\Omega^2}{\frac{T_1}{T_2}\Omega^2 + (\Delta\nu)^2 + \frac{1}{T_2^2}} \tag{4.9}$$

The ER is given by the ratio of these two terms: [8]

$$\mathrm{ER} = \frac{|\alpha_\infty|^2}{n_\infty} \tag{4.10}$$

$$= \frac{T_2}{2T_1}\frac{1 + (\Delta\nu)^2 T_2^2}{(1 + \Omega^2 T_1 T_2 + (\Delta\nu)^2 T_2^2)} \tag{4.11}$$

On resonance ($\Delta\nu = 0$), the ER goes to a maximum value $T_2/2T_1$ at the limit of very low power[10]. As such, an interesting prospect for a highly coherent source of indistinguishable photons is a QD driven at relatively low Ω. An important measure is the saturation Rabi frequency Ω_S, given by $\Omega_S = 1/\sqrt{T_1 T_2}$, at which the on-resonance ER = 1/2, and so the low power limit is when $\Omega \ll \Omega_S$.

4.2.2 Samples used

All samples used in these experiments have identical electrical device designs, both being n-i-Schottky structures. The significant differences are in their optical structures.

The first sample used in these experiments, 050328C#8c, is a wafer of GaAs approximately 500 microns thick. The QDs are partially-capped islands (PCI) 25nm above an n+doped layer that acts as the back gate. The QDS are themselves 136nm below the top surface of the sample, with a 100 nm AlAs/GaAs superlattice above the QDs. The Schottky contact of the n-i-Schottky is a semitransparent layer of 5nm thick nickel-chrome on the top surface of the sample. This sample exhibits a much smaller degree of charge noise than VN2455, so it is better for examining the effects of spin noise.

The second sample, VN2455, was designed specifically (by Dr Y. Ma) to increase the coupling of light out of the sample into the collection optics. The In-flush QDs are embedded in a 5th-order planar cavity made by depositing a gold mirror on the bottom surface of a GaAs membrane – the cavity is 642nm thick, with the QD layer 466 nm below the sample surface. There is a AlAs/GaAs superlattice 30nm below the QD layer to prevent current leakage, and the gold mirror on the bottom surface acts as a Schottky contact. 25nm above the QD layer is an n-doped GaAs layer which acts as the second contact of the n-i-Schottky device structure, which allows charge tuning of the QDs. This sample has a large degree of charge noise as shown in Fig. 4.3, and so spectra from this sample will be compared to the results of my charge noise simulation.

The third sample, KV14101, follows a similar design to VN2455. Whereas VN2455 forms a 5th-order planar cavity, KV14101 has the QDs embedded in a 4th-order planar cavity with a 3-pair AlAs/GaAs distributed Bragg reflector (DBR) above the QD and n-doped layers, just below the processed sample surface. This sample represents and improvement over VN2455 due to its increased coupling of light out of the sample (measured as 46.1%), with a much smaller degree of charge noise. This sample was predominately used in coincidence measurements, as its relative lack of charge noise makes its optical behaviour very similar to 050328C#8c, but its improvement in coupling efficiency significantly decreases the time taken in second order coherence and two-photon interference measurements.

4.3 Spin noise

Nuclear spin noise arises from the large number ($\sim 10^5$) of fluctuating nuclear spins that electron (and to a smaller extent hole) spins interact with. In InGaAs, each of the nuclei have non-zero spins (9/2 for In, 3/2 for Ga and As), so these will interact with the single particle spins in the semiconductor via the nuclear hyperfine

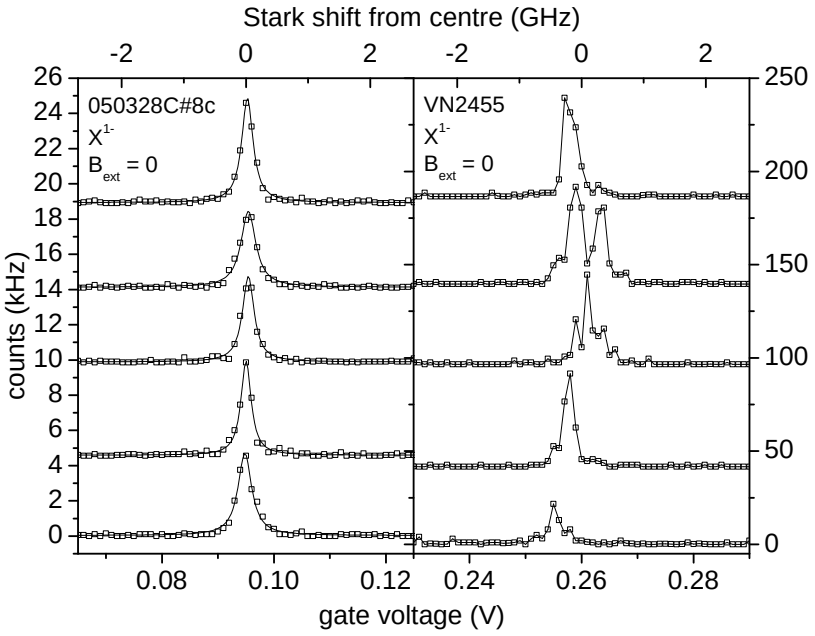

Figure 4.3: Left: plot of 5 consecutive voltage sweeps across X^{1-} resonance for the PCI bulk sample 050328C#8c. Lines are Lorentzian fits to data points. Right: plot of 5 consecutive voltage sweeps across X^{1-} resonance for the In-flush planar cavity sample VN2455. The resultant Stark shifts are plotted on the top axis. Clearly the sample VN2455 exhibits a higher degree of charge noise. Note the approximately tenfold increase in count rates from 050328C#8c and VN2455: this is due to the planar cavity structure in VN2455 resulting in increased coupling of light into the collection optics. For both samples, $\Omega \ll \Omega_S$, integration time for each point = 10 ms.

interaction. This effect is much greater in QDs than in bulk semiconductors as the confinement of the electron spin wavefunction within a small volume means that the spin sees the contribution of a smaller number of nuclear spins: in general, $\sim 10^5$. This number is too small to allow efficient cancellation of the total nuclear spin by averaging, but is also too large to treat the nuclear spins individually. The electron spin will thus be affected by a fluctuating effective field B_n. The nuclear spins have, in the absence of dynamic spin polarisation, randomly fluctuating orientations with a timescale $\sim 10^{-4}$s. While the time averaged field $\langle B_n \rangle$ is equal to zero, the electron spin will interact with a field (the Overhauser field) with a magnitude $\delta B_n = \sqrt{\langle B_n^2 \rangle - \langle B_n \rangle^2}$. This is known as the *frozen fluctuation model.*[11, 12]

For the negatively charged exciton in an InGaAs QD, at low Rabi frequency, δB_n generally takes a value given by $B_{max}/\sqrt{N}$, where B_{max} is the maximum nuclear magnetic field given by all of the nuclear spins aligned in one direction, and $N \sim 10^5$ is the number of nuclear spins that the electron spin interacts with. For a self-assembled InGaAs QD, $\delta B_n = 20 - 40$ mT. This effective field results in a small Zeeman splitting to the ground single electron state due to the significant contact hyperfine interaction between the electron and the nuclear spins, as in Fig. 4.4 (in holes, this interaction is very small due to valence states being made up of

atomic p-orbital states, whose wavefunctions are approximately zero at the position of the nucleus—the remaining dipole-dipole interaction is also much smaller than the contact hyperfine interaction between nuclear spins and electrons, so is neglected in this discussion). The fluctuating Overhauser field affects the selection rules for the system. If the magnetic field is in the growth direction, or Faraday geometry, as in Fig. 4.4 (b), the spin selection rules mean "vertical" transitions are allowed, via emission or absorption of a circularly polarised photon ($\Delta s = \pm 1$), whereas the "diagonal" transitions have $\Delta s = \pm 2$, so they are forbidden. If the magnetic field is in the plane (i.e. in the Voigt geometry, or perpendicular to the direction of light emission), the alignment of electron spins to the applied field allows the diagonal transitions via the emission or absorption of linearly polarised light. In this case, in addition to elastic Rayleigh-scattered photons, inelastically-scattered Raman photons are emitted, resulting in narrow linewidth peaks red- and blue-shifted from the elastic peak. Each individual Raman photon has a coherence time determined by the dephasing rate for the Raman-scattering final single electron state to the Rayleigh scattering ground state.

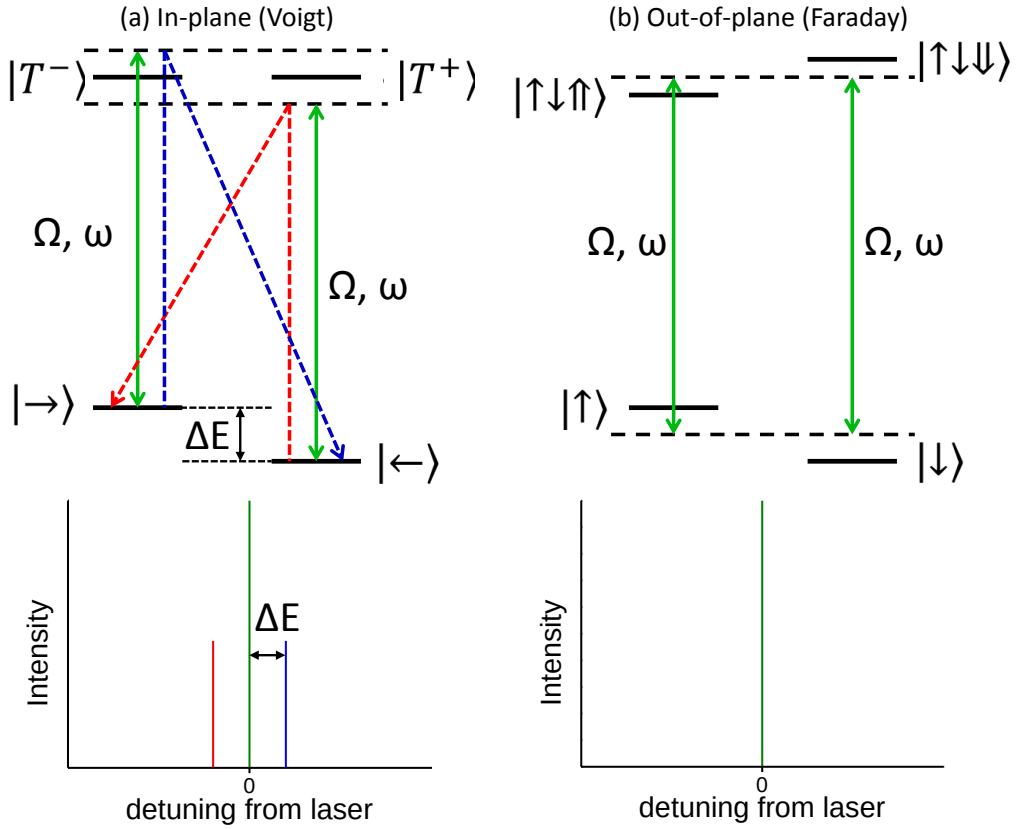

Figure 4.4: Level diagram at low power $\Omega < \Omega_S$ showing two different regimes of magnetic field: Voigt (a) and Faraday (b) geometry. In the Voigt geometry, the diagonal transitions $|T^-\rangle \rightarrow |\leftarrow\rangle$ and $|T^+\rangle \rightarrow |\rightarrow\rangle$ are allowed, resulting in inelastic Raman scattering (blue and red) detuned by ΔE from the elastic Rayleigh scattering (green). In the Faraday geometry, the diagonal transitions are forbidden, resulting in only elastic Rayleigh scattering.

This splitting in the single electron state has two effects relevant to this discussion. First, dephasing between these two levels due to the random orientation of the Overhauser field over experimental timescales reduces the coherence time of the electron state and thus the ensemble dephasing time T_2^*—the fact that the electron dynamics are determined by different frozen fluctuations for each repeat of the scattering process means that while each individual instance of the electron spin precesses coherently around the frozen Overhauser field with Larmor frequency $\omega = g_e \mu_B \delta B_n / \hbar$, where g_e is the electron g-factor and μ_B is the Bohr magneton, the time-averaged state of the electron dephases with lifetime T_2^*.[11, 12]

Second, the Raman-scattered photons allowed by the in-plane component of the Overhauser field result in optical spin pumping (OSP): if the excitation laser is resonant with one transition, for example $|\leftarrow\rangle \rightarrow |T^{1-}\rangle$, the hyperfine interaction with the Overhauser field allows a diagonal transition to the exciton ground state $|\rightarrow\rangle$ via Raman scattering. This exciton transition is not being excited, so the electron is effectively "shelved" in the $|\rightarrow\rangle$ state until the dephasing effect of the nuclear spins or cotunnelling into the Fermi sea in the back contact allows the electron spin to flip to the bright exciton ground state $|\leftarrow\rangle$.[1, 2]

4.3.1 Magnetic field tuning of negatively charged excitons

Through a combination of laser and electric field tuning at different external magnetic fields B_{ext}^Z, it is possible to determine the electric field dependence of each Zeeman-split line and thus for a given electric field plot the magnetic field shift to the exciton lines to determine the exciton g-factor. The overall effect is a combination of a linear Zeeman shift and a quadratic diamagnetic shift:

$$\Delta E(B_{ext}^Z) = \pm g_X \mu_B B_{ext}^Z + \alpha {B_{ext}^Z}^2 \tag{4.12}$$

where g_X is the exciton g-factor, μ_B is the Bohr magneton and α is the diamagnetic coefficient.

Since the Zeeman shifts for the two transitions are equal and opposite, the diamagnetic shift is simply the mean of the total shifts, and can thus be subtracted to give the pure Zeeman shift (Fig. 4.5). For this QD, the diamagnetic coefficient is extracted from a fit to the mean shift with B_{ext}^Z, which comes to $9.40\,\mu\text{eV T}^{-2}$. The Zeeman shift slopes are then $\pm 49.2\,\mu\text{eV T}^{-1}$, which results in an exciton g-factor of $|g_X| = 0.85$. The electron and hole g-factors are given by $g_e + g_h = g_X$, but since these measurements were done in the Faraday geometry, where applied magnetic field affects both the electron and hole spin, it is not possible to separate these from the exciton g-factor.[13]

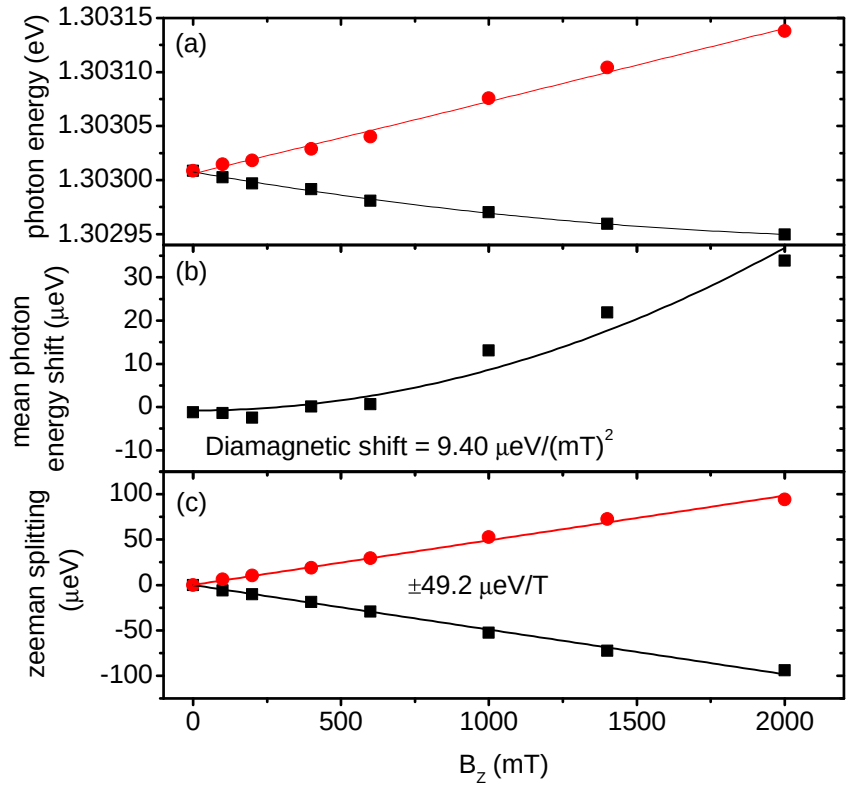

Figure 4.5: Plots of the effect of external magnetic field in the Faraday geometry B_{ext}^Z on the emission energy of the X^{1-} line. (a) shows the actual energy positions of the two Zeeman split lines with applied B_{ext}^Z, with lines fit using Eq. 4.12. (b) shows the diamagnetic shift given by the midpoint of the peak positions. (c) shows the peak positions with the diamagnetic shift subtracted, to give the Zeeman splitting of the exciton by applied magnetic field. Data taken from sample 050328C#8c.

4.3.2 High resolution FPI spectra

FPI spectra were taken at zero and 600mT external magnetic field B_{ext}^Z for a range of Rabi frequencies Ω above and below saturation Ω_S (Fig.4.1). Ω is calculated as a function of laser power by finding the splitting of the Mollow triplet at a number of high excitation powers, and then fitting using the relation $\Omega \propto \sqrt{P}$ where P is excitation power to find Ω at powers below saturation. At low powers with zero B_{ext}^Z, where the effect of the Overhauser field dominates, the spectra take the form of the central narrow elastic Rayleigh peak, with two inelastic peaks either side of the central peak. This doublet is due to Raman-scattered photons. Because the Overhauser field fluctuates in direction and magnitude with a timescale of ~ 1 ms and measurements are taken over minute timescales, the positions of these Raman peaks jump around $\sim 10^5$ times in one measurement, resulting in two 'smeared-out' peaks either side of the narrow Rayleigh peak with the width determined by the variance in B_n.

The proof that this doublet is the result of fluctuating energy Raman photons

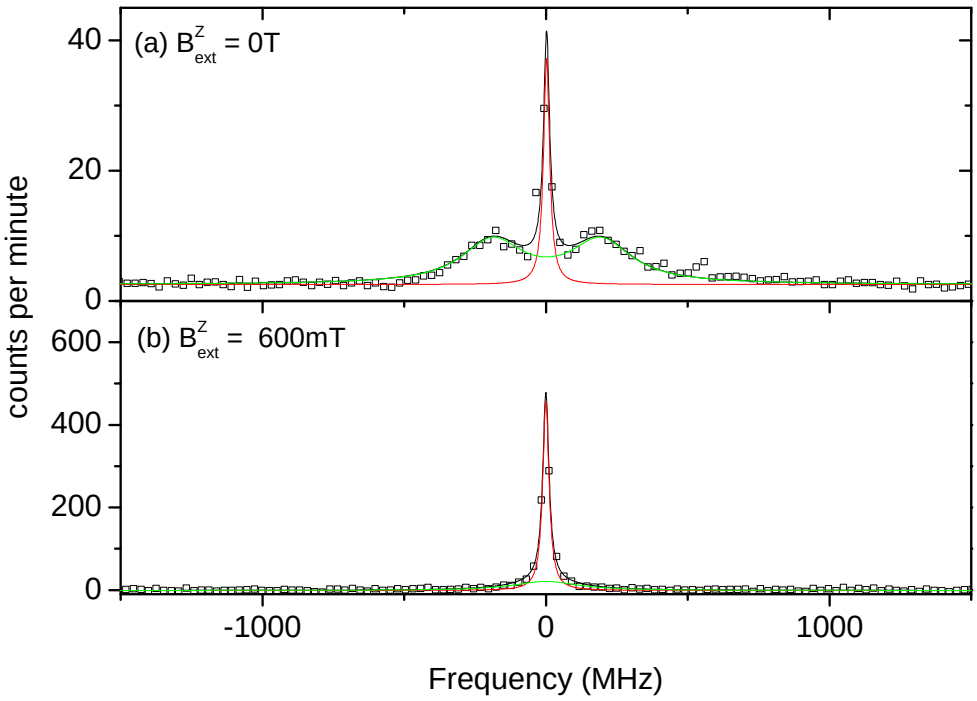

Figure 4.6: Low power ($\Omega = 100$ MHz $\ll \Omega_S$) high-resolution FPI spectra at $B^Z_{ext} = 0$ (a) and $B^Z_{ext} = 600$ mT (b). Black squares are raw data, lines are Lorentzian fits to the Rayleigh peak (red), doublet (green) and full spectrum (black). Note the wide doublet in (a), caused by Raman-scattered photons, with a fluctuating Overhauser field shifting the single electron energies. The splitting and linewidth of the doublet is as expected from the variance of the Overhauser field and the extracted g-factor. This agrees with modelling done by Mr T. Santana: model not shown here. Data taken from sample 050328C#8c.

is in FPI spectra taken by detuning the excitation laser from resonance with the transition (data taken by Dr J. Zajac, Fig. 4.7). If the doublet were an incoherent spontaneous emission process from the exciton to the single electron, the peaks would have linewidths determined by the lifetime of the exciton and their energy would be independent of the energy of the excitation laser, i.e. detuning the laser would move the Rayleigh peak but not the incoherent doublet. What we see instead is that detuning the laser moves the Rayleigh peak and the doublet, with no change to the width or spitting of the doublet. This could only be true if the situation is as in Fig. 4.4 (a), where the energy of the laser (in conjunction with the distribution of single electron splittings due to the Overhauser field) determines the energy of the Raman photons.

Fitting with Lorentzians, it is possible to determine the fraction of photons emitted elastically and inelastically for a range of excitation powers. A fit of the elastic ratio can be made with the following formula:

$$\frac{I_e}{I} = \frac{T_2^*}{2T_1} \frac{1}{1 + (\Omega/\Omega_S)^2} \tag{4.13}$$

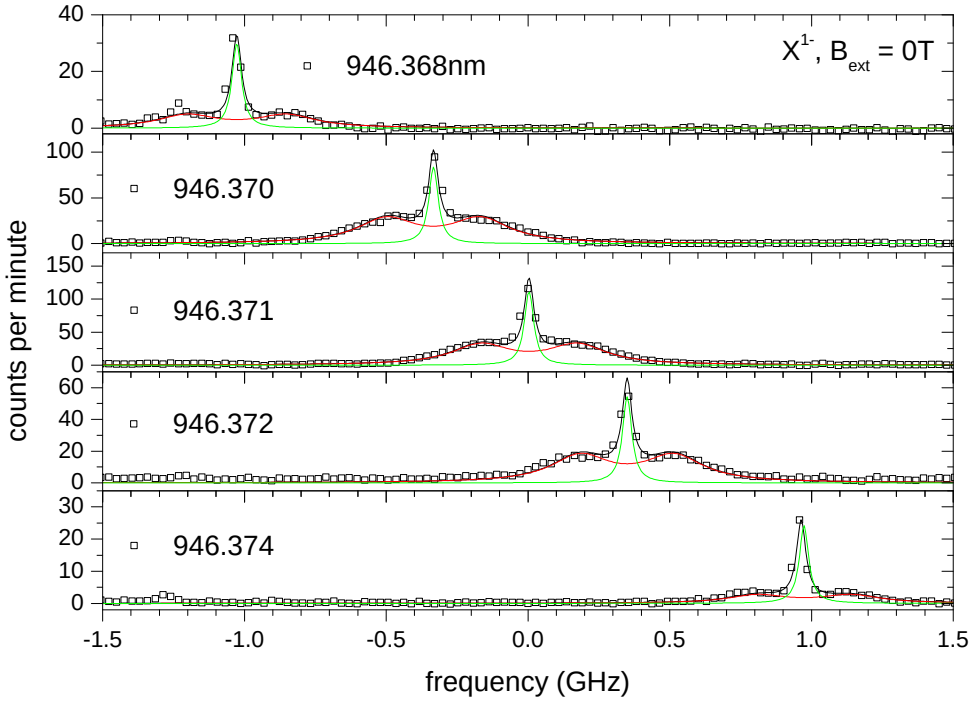

Figure 4.7: High resolution FPI spectra with detuning of laser from transition resonance at 947.371 nm. While the number of photon counts drops as the laser is detuned, the doublet moves with the Rayleigh peak, and there is no change in the doublet splitting or linewidth. This clearly shows that the doublet is made up of Raman photons. Data taken from sample 050328C#8c.

where Ω is the Rabi frequency and Ω_S is the saturation Rabi frequency. T_2^* is used here rather than T_2 because the inelastic contribution to this ratio is made up of Raman photons, which on their own are coherent, but due to the fluctuating Overhauser field δB_n over experimental timescales, the time-averaged photon coherence is dephased. As such, the limit at very low power $\Omega \ll \Omega_S$ the elastic ratio directly gives the ratio of $T_2/2T_1$, with a maximum value of 1. It is also clear that in the ideal case, all of the emission at low powers will be elastically scattered light.

At $B_{ext}^Z = 0$, the low-power limit of elastic ratio is much less than 1. When elastic ratio vs Rabi frequency is fit to the formula, a value of 0.26 ± 0.01 is obtained (Fig. 4.9). This demonstrates that there is significant ensemble dephasing from the Overhauser field with no applied magnetic field. B_{ext}^Z was increased to 600 mT, which strongly aligns the electron spins in the Z-direction. This screens the electrons from the in-plane contributions of the Overhauser field $\delta B_n^{x,y}$, resulting in a smaller probability of Raman scattering. The FPI spectra from this set-up follow the textbook explanation: the elastically scattered light comes to a maximum at around the saturation Rabi frequency and starts to decrease with increasing power whereas the inelastically scattered light increases to a saturation point at high powers (Fig. 4.8 (b)). The elastic ratio shows that this case is very close to the ideal: the

low Rabi limit is 0.97 ± 0.03, giving $T_2 = (1.94 \pm 0.06)T_1$ (Fig. 4.9). This only screens the electron spin from $\delta B_n^{x,y}$, however: it does not screen it from the Overhauser fluctuations in the Z-direction δB_n^Z; it still dephases the electron spin.

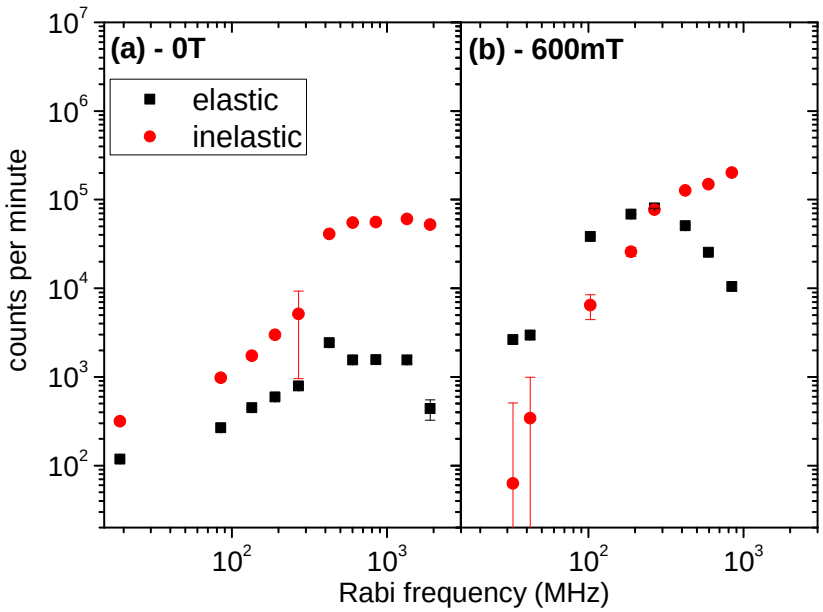

Figure 4.8: Plot of elastic and inelastic counts for the QD with an applied magnetic field of (a) 0T and (b) 600mT. Note that the elastic counts at 600mT are higher than those at 0T and cross over at the saturation Rabi frequency 295 MHz. Data taken from sample 050328C#8c.

4.3.3 Optical spin pumping in second order correlations

Second-order correlation measurements were taken to determine the photon anti-bunching in the emission from the samples, and to extract the fluorescence lifetime T_1 by using a fit to the dip using an exponential peak function

$$g^2(\tau) = 1 - ae^{-|\tau|/(T_1)} \tag{4.14}$$

where a takes into account deviation from perfect antibunching due to background and dark counts and time jitter in the detectors. This is then deconvolved with the IRF to derive the "true" $g^2(\tau)$. The data was taken at below saturation ($\Omega \ll \Omega_S$) to eliminate Rabi oscillations in $g^2(\tau)$, which artificially narrow the antibunching dip, making it difficult to resolve with the time jitter of the detectors.

The $g^2(\tau)$ for $X^{1-}$with no external field shows a definite dip to $\sim 20\%$ in the raw data, which reduces to 0 after deconvolution (Fig. 4.10 (a)). At zero external magnetic field, T_1 comes to 775 ± 77 ps. For X^{1-} for the same QD with $B_{ext}^Z = 600$ mT, $T_1 = 696 \pm 55$ ps. The low power limit elastic ratios (Fig. 4.9) then give decoherence times $T_2(B_{ext}^Z = 0) = 403 \pm 41$ ps and $T_2(B_{ext}^Z = 600$ mT$) = 1350 \pm 115$

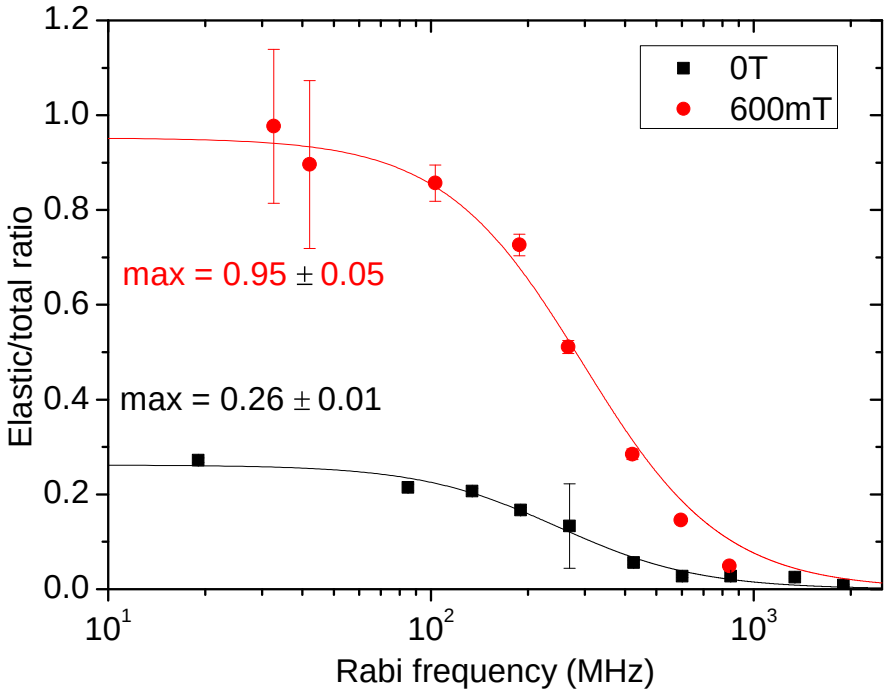

Figure 4.9: A plot of elastic ratio for no applied B field (black) and 600mT applied B field (red). Data taken from sample 050328C#8c.

ps.

However, we also see bunching either side of the antibunching dip, which is not seen in $g^2(\tau)$ from the X^0. The bunching decays with a time scale on the order of 10s of nanoseconds (for this QD, 9.98ns), which is much longer than T_1. This bunching is a result of optical spin pumping (OSP) of the ground states: see Fig. 4.10. At $B^Z_{ext} = 0, \Omega \ll \Omega_S$, $\delta B^{x,y}_n$ allows Raman scattering from the resonant transition ground state $|e_i\rangle$ to the off-resonance ground state $|e_f\rangle$ in addition to Rayleigh scattering from $|e_i\rangle$ to $|e_i\rangle$. If a photon is detected, and another photon detected after a delay $\delta\tau$ such that $T_1 \lesssim \delta\tau < T_{fi}$, where T_{fi} is the lifetime for the dephasing of $|e_f\rangle$ to $|e_i\rangle$, it is likely that the first photon is a result of Rayleigh scattering, because this quickly returns the electron to $|e_i\rangle$, ready for another photon scattering event. If $\delta\tau \gtrsim T_{fi}$, it is likely that the first photon was a Raman photon, shelving the electron in $|e_f\rangle$ for on average T_{fi}. This prevents a second scattering event quickly after the first photon, which reduces the rate at which photons are detected after $\delta\tau \geqslant T_{fi}$, resulting in an exponential peak in $g^2(\tau)$ with decay time T_{fi}. When considered over a very large number of time delay measurements, this means that as the time between photon detection events on the two channels increases, there is a greater chance that OSP has occurred, resulting in a decrease in the count rate for long delay. Increasing B^Z_{ext} to 600mT increases T_{fi} (Fig. 4.11 (a), red line), while having no effect on the antibunching: this is because a magnetic field applied in the Faraday geometry reduces the transfer rate from $|e_f\rangle$ to $|e_f\rangle$.[14] In the absence

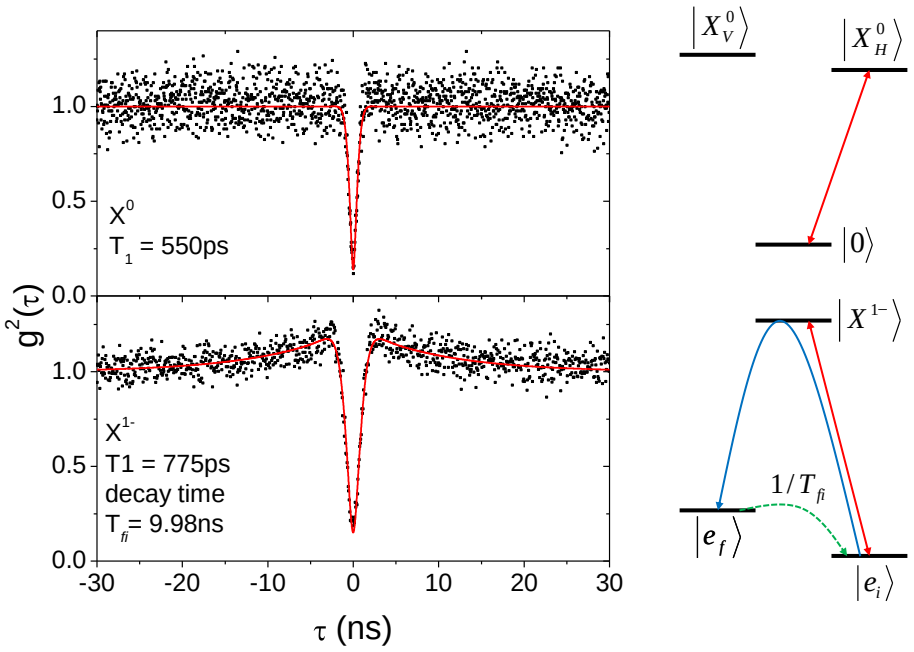

Figure 4.10: Left: $g^2(\tau)$ plots for (top) X^0 and (bottom) X^{1-} at $B^Z_{ext} = 0$. Note the bunching decay in X^{1-} with lifetime $T_{fi} = 9.98$ns. Right: level diagrams for scattering at $\Omega \ll \Omega_S$: for X^0 (top), there is only Rayleigh scattering (red arrows) from each of the orthogonal X^0 states. For X^{1-}, there is a combination of Rayleigh and Raman (blue arrow) scattering due to $\delta B^{x,y}_n$. After Raman scattering the electron is shelved in state $|e_f\rangle$, so it has to decay to state $|e_i\rangle$ (green dashed arrow) with lifetime T_{fi} to allow further photon scattering. Data taken from sample 050328C#8c.

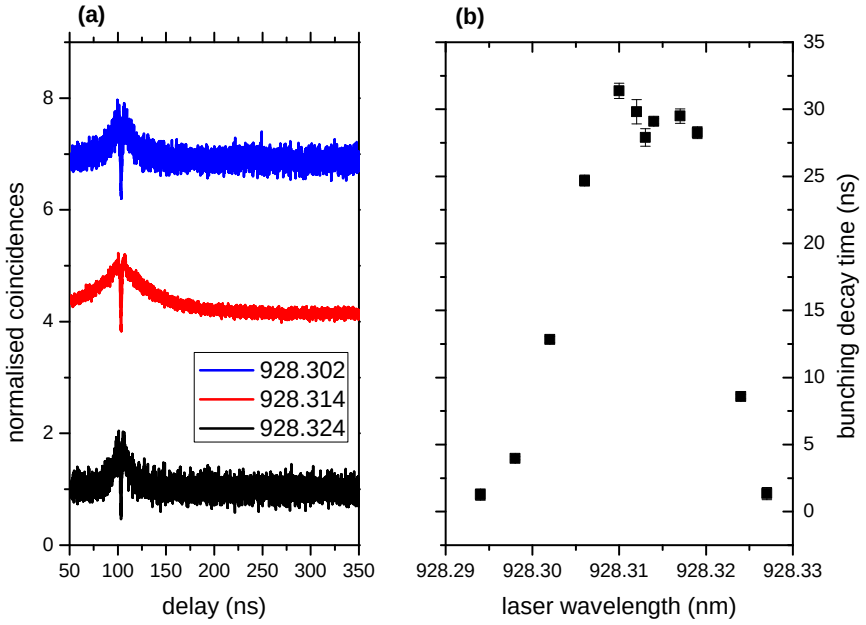

Figure 4.11: (a) plot of second order correlation at 3 points along the X^{1-} plateau at 600mT. These are fit with the $g^2(\tau)$ function Eq. 4.14 with an additional exponential decay peak, and the decay time for these bunching peaks are plotted in (b). The bunching time comes to a maximum in the centre of the plateau where there is negligible cotunnelling. The red dashed line is a guide to the eye. Data taken from sample 050328C#8c.

of cotunnelling (i.e. in the centre of the exciton plateau), T_{fi} is the electron spin dephasing rate due to the hyperfine interaction t_{sp}[15]:

$$1/T_{fi} = 1/t_{sp} + 1/t_{co} \tag{4.15}$$

where t_{co} is the cotunnelling rate, which is dependent on the voltage position on the plateau. This is demonstrated by measuring the second-order correlation at a number of points across the plateau, as in Fig. 4.11 (a) (data taken by Dr J. Zajac). The bunching decay comes to a maximum at the centre of the plateau at about 928.310 nm, and by fitting with an exponential decay the bunching lifetime can be determined (Fig. 4.11 (b)). At the maximum, this comes to 31.4 ± 6 ns. This shows good qualitative agreement to the timescale of 40 ns observed by Hansom *et al.* [16] Using the count rate of the X^{1-} at points along the plateau, it is possible to obtain t_{co} and its dependence on plateau position,[13] and then determine the real value of t_{sp} via Eq. 4.15. This has not been done here.

2-laser excitation

The $g^2(\tau)$ measurements were repeated at 600mT, but using 2 lasers to resonantly excite each of the Zeeman-split transitions at the same time. When excited individually, as in Fig. 4.12 (a) and (b), the transitions both displayed bunching around the

antibunching dip with similar bunching lifetimes ($\sim$ 20ns). When both transitions were excited, however, the bunching essentially disappears, as shown in Fig. 4.12 (c). This proves that the bunching is an effect of OSP, as "repumping" the second transition frustrates OSP.[2]

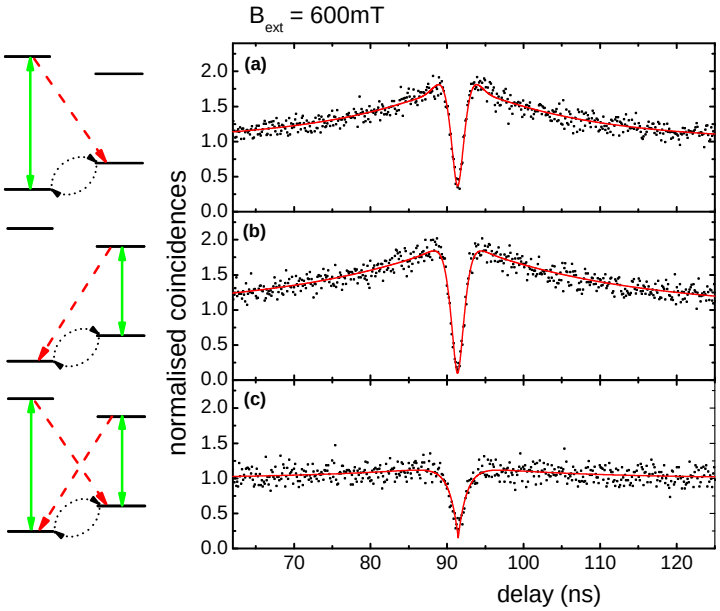

Figure 4.12: Second order correlation plots for 2-laser excitation with level diagrams (left) showing the transition being excited (green arrow) and the relevant Raman scattering (red dashed arrow) and ground state spin flip process (black dotted arrow). (a) and (b) show the high energy and low energy excitons being excited individually, and clearly show long bunching decays of 15.9 and 20.8 ns respectively, and high bunching amplitudes. (c) shows the second order correlation when both transitions are excited. In this case the bunching disappears as repumping the second excitonic transition frustrates the OSP. Data taken from sample 050328C#8c.

4.3.4 Hong-Ou-Mandel interference: indistinguishability

In order to measure the indistinguishability of the photons emitted by the quantum dot, a fibre-based Hong-Ou-Mandel (HOM) interferometer is used, and coincidences from the output are measured. This data is shown in Fig. 4.13. In the case of the X^0, where there is no Raman scattering due to nuclear spins, the visibility is close to the ideal, with deconvolved (raw) visibility of 100$\pm$6% (63$\pm$4%). With zero applied field, the deconvolved (raw) visibility of the X^{1-} HOM signal is 81$\pm$8% (50$\pm$5%), whereas with an external field of 600mT, the deconvolved (raw) visibility increases to 99$\pm$9% (64$\pm$6%). The visibility depends on the indistinguishability of the photons meeting at the second beamsplitter. Applying a large field compared to the Overhauser field screens the single electron spin from the nuclear spins, reducing the probability of

inelastic Raman scattering, and thus improving the indistinguishability of emitted photons.

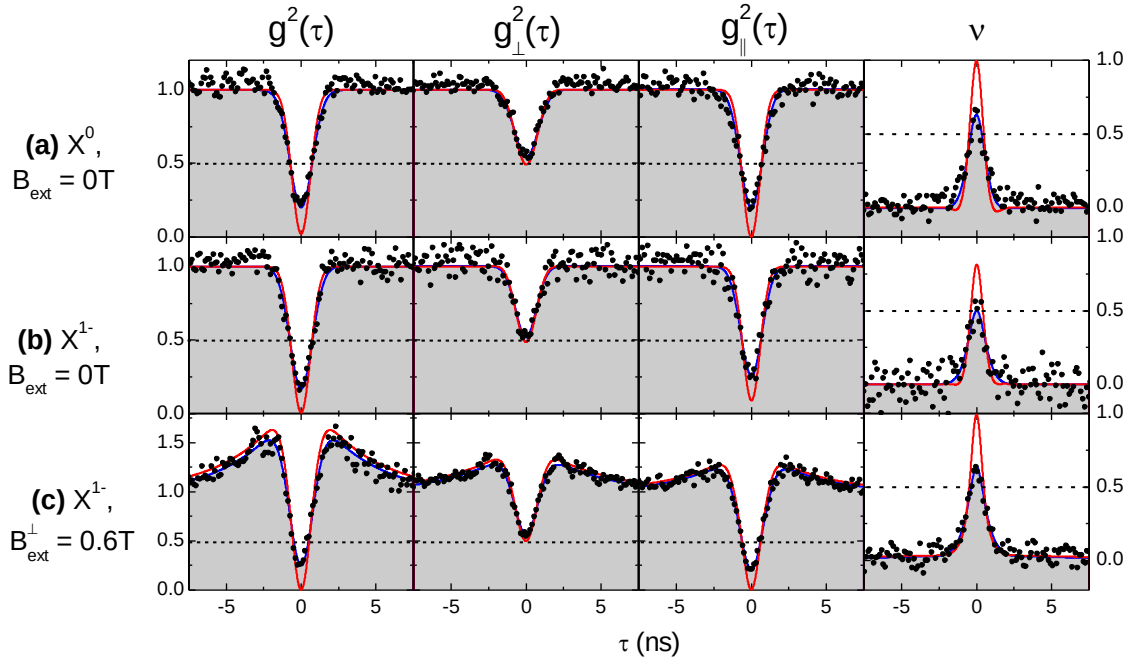

Figure 4.13: Plot of $g^2(\tau)$ and HOM measurements done on X^0 (a), and X^{1-} at zero magnetic field (b) and 600mT (b) from sample KV14101. Blue lines are fits to the data, and red lines are fits deconvolved with the IRF.

4.4 Charge noise

Charge noise is the result of the QD being located in a fluctuating charge environment, for example due to atomic impurities or crystal defects in the sample charging and uncharging over time. These fluctuating charges cause a fluctuating Stark shift of the fundamental transition energy in the QD, in turn causing shifts to the emission wavelength of the exciton. Over time, this results in broadening of the excitonic emission that can be approximated with a Gaussian distribution.[17]

Another factor to consider, especially in the context of charge noise, is the effect of a detuning of the laser wavelength from the QD resonance frequency. As would be expected, the overall emission from the QD is reduced with increasing detuning, but the spectral properties of Rayleigh scattering are unaffected by this detuning. This means that the ER is increased at intermediate and high powers (i.e. $\Omega \geqslant \Omega_S$) with increased detuning, as shown by Eq. 4.11. Another effect of detuning is that the Mollow sidebands move outwards from the centre peak with detuning as the effective Rabi frequency Ω' increases (see Eq. 4.8 and Ref. [8]).

An important distinction to make between charge and nuclear spin noise is how different parts of the inelastic fluorescence spectrum for X^{1-} are sensitive to different sources of noise. Since the Overhauser field splits the single electron ground states

in the QD in energy, it results in the spectrum being made up of two superimposed inelastic contributions with different resonance energies, averaged over time with fluctuations of the Overhauser field: this lowers the time-averaged peak value, so the peak of the spectrum is most sensitive to nuclear spin noise. On the other hand, charge noise results in spectral diffusion: the spectrum is made up of an average of a large number of contributions with a Gaussian distribution of centre energies around some central resonance. This strongly affects the overall linewidth of the the spectrum, so the edges of the peak are most sensitive to charge noise. [18, 19]

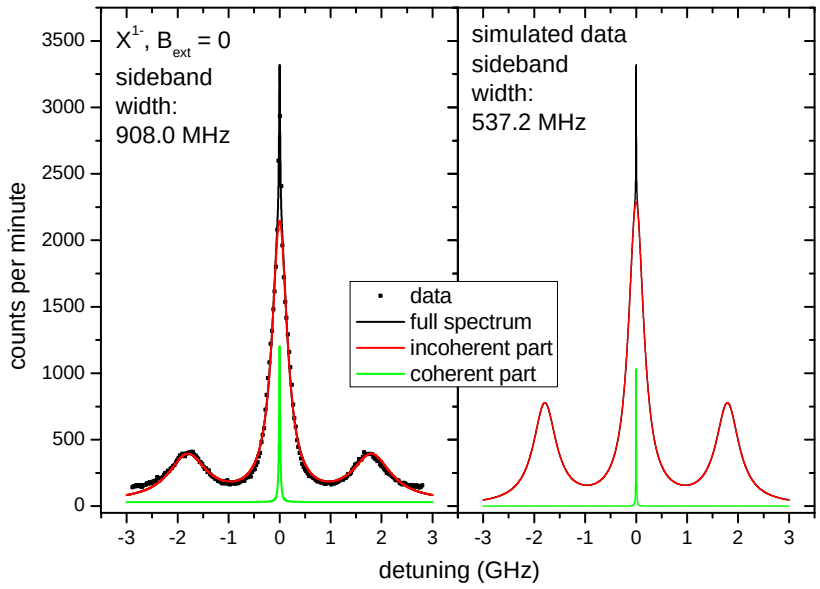

Figure 4.14: A comparison of the X^{1-} spectrum obtained from experiment at $B_{ext} = 0$ (left) and a spectrum generated using the Mollow theory with zero charge noise (right), at equal Rabi frequencies $\Omega = 1792$ MHz $\gg \Omega_S$ and linewidths $\Gamma = 358.1$ MHz. The real spectrum has been fit with a combination of four Lorentzian peaks. Note that the real data has much shorter and wider sidebands than the simulation: this is an effect of charge noise smearing out the sidebands.

As discussed above, in order to maximise the ER and thus indistinguishability of photons scattered from a QD, it is desirable to excite the QD with low Ω. In this regime, the effect of charge noise on the shape of the spectrum is smaller than at high Ω. At $\Omega \gg \Omega_S$, we expect to see spectral fluctuations of the incoherent fluorescence part of the spectrum, and increased splitting of the Mollow sidebands, as demonstrated by Eq. 4.8, both of which would reduce indistinguishability. At $\Omega \ll \Omega_S$, the spectrum is made up of three parts: the elastic Rayleigh scattering peak, a small incoherent fluorescence peak due to dephasing if $T_2 < 2T_1$ with linewidth $2/T_2$, and the Raman scattering doublet due to nuclear spin fluctuations. The Rayleigh and Raman peaks are always centred around the laser wavelength regardless of detuning from resonance, as demonstrated by Fig. 4.7. Charge noise will Stark shift the fluorescence peak, resulting in inhomogeneous broadening. Additionally,

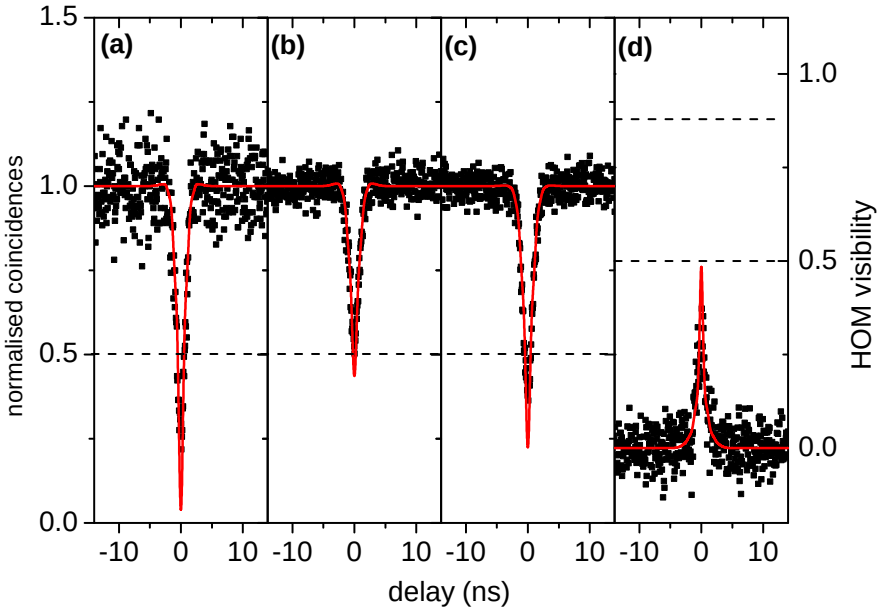

Figure 4.15: Plot of $g^2(\tau)$ and Hong-Ou-Mandel measurements done on sample VN2455 with $B_{ext} = 0$. (a) $g^2(\tau)$ shows a deconvolved dip to 4%, demonstrating that even with a high degree of charge noise, the QD remains a good single photon emitter. Plots of coincidences at crossed (b) and parallel (c) polarisations show dip depths similar to sample 050328C#8c at $B_{ext} = 0$. The visibility (d) comes to a deconvolved peak value of 0.48 at zero delay.

as the detuning between laser and resonance increases, the counts due to the three scattering or emission mechanisms will decrease. The fluorescence counts fall off much faster with detuning, so increased detuning will in fact increase the ER, as demonstrated in Eq. 4.11. While the ER is still limited by the value $T_2/2T_1$ as $\Omega \to 0$, detuning will increase the ER towards this limit as Ω increases. This effectively increases the saturation Rabi frequency where the ER drops to 1/2 of its initial value from $\Omega_S = 1/\sqrt{T_1 T_2}$ to

$$\Omega'_S = \sqrt{\frac{1 + (\Delta\nu)^2 T_2^2}{T_1 T_2}} \tag{4.16}$$

The result of this is that detuning, while decreasing the number of photons scattered from the QD, actually increases the proportion of coherently scattered photons: this means that it is possible to operate at increased Ω without sacrificing elastically scattered photons. However, overall count rates will be significantly reduced with increased detuning. Charge noise causes "flickering" of the QD signal as the exciton moves in and out of resonance, reducing the overall count rate.

It is therefore expected that at low power, charge noise will not have a strong effect on the HOM visibility, because (as seen in Fig. 4.1), at $B_{ext} = 0$, the low Ω spectrum is dominated by Rayleigh and Raman scattered photons, which are

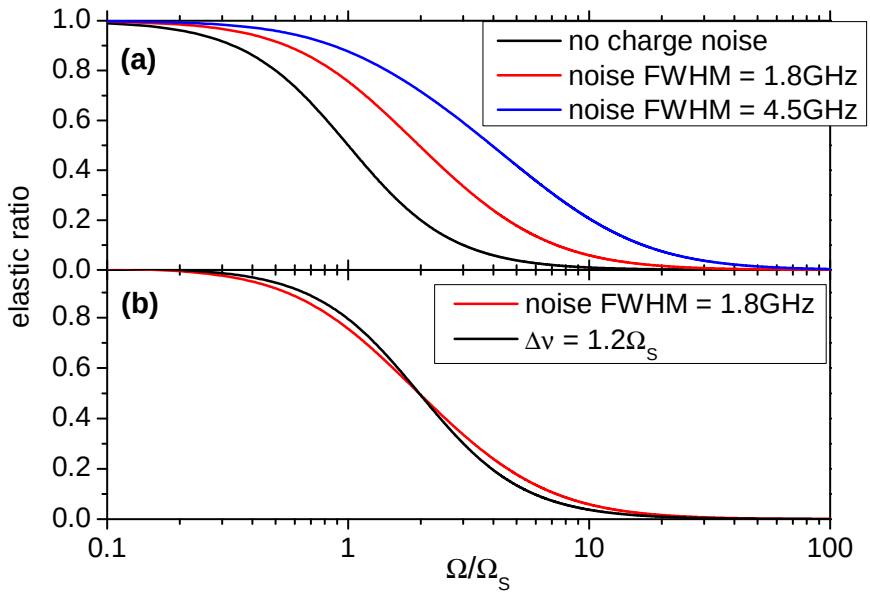

Figure 4.16: Simulated plots of ER for different degrees of detuning or charge noise: in all cases, $T_2 = 2T_1$. (a): ER for no charge noise, FWHM = 1.8GHz Gaussian charge noise, and FWHM = 4.5GHz Gaussian charge noise. While the low (high) Ω limit is still $T_2/2T_1$ (0), the charge noise shifts the effective saturation Rabi frequency to higher values. (b): a comparison between ER with a fixed detuning and charge noise, with detuning chosen to give the same effective saturation Rabi frequency. While increasing charge noise and fixed detuning both result in increased effective saturation Rabi frequencies, charge noise also changes the shape of the curve to give higher ER at higher Ω. Ω_S: saturation Rabi frequency at zero noise and detuning.

affected by detuning from resonance more weakly than fluorescence (see Fig. 4.7). Demonstration of this is provided by Fig. 4.15, which shows a similar level of indistinguishability to sample KV14101 at zero applied magnetic field (Fig. 4.13).

In order to investigate the effect of charge noise on the ER, we can model the charge noise as a time-average of random detunings: if we integrate Eq. 4.11 over a Gaussian distribution of $\Delta\nu$, we have an expression that should model the effect of charge noise[17]. A Gaussian distribution of detuning is a reasonable assumption as the Stark shift is in the linear regime, the electric field fluctuations arise due to a large number of electric field sources, and the integration time is 60 s, compared to reported charge noise rates of 10^0to10^3 Hz, i.e. timescales of 1 s to 1 ms.[18, 20] Looking at voltage sweeps through resonance for the X^{1-} line at $B_{ext} = 0$ in sample VN2455 (Fig. 4.3, right panel), the gate voltage FWHM of the peak position is around 0.2 V. Using the Stark shift of the exciton plateau, this results in a detuning FWHM of around 1.8 GHz due to charge noise. This can then be used in the Gaussian distribution of detunings to generate data from this model.

Fig. 4.16 demonstrates the effect of charge noise on the elastic ratio. Increasing FWHM of the Gaussian distribution of the charge noise increases the effective

saturation Rabi frequency, i.e. the Rabi frequency at which the ER falls to half its maximum. This increases the range of excitation powers that can be used to still generate high degrees of elastically scattered photons. Eq. 4.16 shows that the same is true of fixed detuning, but Fig. 4.16 (b) shows that charge noise also changes the shape of the ER slope, reducing the effect of increasing power and increasing the ER at higher Ω. Fixed detuning also decreases the overall count rate from the QD, while charge noise means that the exciton transition is spending some time on or close to resonance with the excitation laser, increasing count rates from the QD. Both of these cases result in fewer scattered photons than the on-resonance case. There is scope for further work to be done to investigate this.

4.5 Summary

Two sources of noise in QDs have been identified and their effects of the emission of indistinguishable photons have been investigated. Of these, noise due to fluctuating nuclear spins is the most important. The in-plane component of the Overhauser field results in inelastically scattered Raman photons which, at low powers, give rise to a doublet of peaks in the spectrum, negatively affecting indistinguishability. The peaks are broadened due to the fluctuations in the Overhauser field over experimental timescales. Applying a relatively large external magnetic field in the Faraday geometry aligns the single electron spins in the QD in the growth direction, screening them from the in-plane Overhauser field, reducing the probability of Raman scattering and increasing photon indistinguishability to a value close to 1.

This Raman scattering also gives rise to OSP, observed as bunching in second-order correlation measurements for photons scattered from the X^{1-}. The decay time of the bunching is determined by the electron spin-flip time, which is increased by going to higher magnetic fields. The fact that the bunching is due to OSP is established by performing two-laser excitation of the Zeeman split X^{1-} state, which frustrates spin pumping and reduces the bunching effect.

Charge noise does not negatively affect the indistinguishability of photons scattered from a QD at the low Ω limit, where the dominant scattering mechanisms are elastic Rayleigh scattering and inelastic Raman scattering in the presence of an in-plane magnetic field, and fluorescence is negligible. In fact, charge noise serves to increase the fraction of elastic to total scattered photons at Ω close to Ω_S. This is because charge noise is effectively a randomly (Gaussian) distributed detuning between the laser and exciton energy due to the Stark shift from a fluctuating charge environment. While detuning negatively affects all emission and scattering mechanisms, fluorescence falls off faster with detuning, resulting in a greater proportion of elastically scattered photons at powers where fluorescence would ordinarily be a contributing factor.

4.6 References

[1] Atatre, M. *et al.* Quantum-Dot Spin-State Preparation with Near-Unity Fidelity. *Science* **312**, 551 (2006).

[2] Gerardot, B. D. *et al.* Optical pumping of a single hole spin in a quantum dot. *Nature* **451**, 441 (2008).

[3] Berezovsky, J. *et al.* Nondestructive Optical Measurements of a Single Electron Spin in a Quantum Dot. *Science* **314**, 1916 (2006).

[4] Matthiesen, C., Vamivakas, A. N. & Atatre, M. Subnatural Linewidth Single Photons from a Quantum Dot. *Phys. Rev. Lett.* **108**, 093602 (2012).

[5] Ates, S. *et al.* Post-Selected Indistinguishable Photons from the Resonance Fluorescence of a Single Quantum Dot in a Microcavity. *Phys. Rev. Lett.* **103**, 167402 (2009).

[6] Santori, C., Fattal, D., Vukovi, J., Solomon, G. S. & Yamamoto, Y. Indistinguishable photons from a single-photon device. *Nature* **419**, 594 (2002).

[7] Loudon, R. *The Quantum Theory of Light* (Oxford University Press, Oxford, 2000), third edition edn.

[8] Mollow, B. R. Power Spectrum of Light Scattered by Two-Level Systems. *Phys. Rev.* **188**, 1969 (1969).

[9] Muller, A. *et al.* Resonance Fluorescence from a Coherently Driven Semiconductor Quantum Dot in a Cavity. *Phys. Rev. Lett.* **99**, 187402 (2007).

[10] Proux, R. *et al.* Measuring the Photon Coalescence Time Window in the Continuous-Wave Regime for Resonantly Driven Semiconductor Quantum Dots. *Phys. Rev. Lett.* **114**, 067401 (2015).

[11] Urbaszek, B. *et al.* Nuclear spin physics in quantum dots: An optical investigation. *Rev. Mod. Phys.* **85**, 79 (2013).

[12] Merkulov, I. A., Efros, A. L. & Rosen, M. Electron spin relaxation by nuclei in semiconductor quantum dots. *Phys. Rev. B* **65**, 205309 (2002).

[13] Kroner, M. *et al.* Resonant two-color high-resolution spectroscopy of a negatively charged exciton in a self-assembled quantum dot. *Phys. Rev. B* **78**, 075429 (2008).

[14] Dreiser, J. *et al.* Optical investigations of quantum dot spin dynamics as a function of external electric and magnetic fields. *Phys. Rev. B* **77**, 075317 (2008).

[15] Smith, J. M. *et al.* Voltage Control of the Spin Dynamics of an Exciton in a Semiconductor Quantum Dot. *Phys. Rev. Lett.* **94**, 197402 (2005).

[16] Hansom, J. *et al.* Environment-assisted quantum control of a solid-state spin via coherent dark states. *Nat Phys* **10**, 725 (2014).

[17] Konthasinghe, K. *et al.* Coherent versus incoherent light scattering from a quantum dot. *Phys. Rev. B* **85**, 235315 (2012).

[18] Kuhlmann, A. V. *et al.* Charge noise and spin noise in a semiconductor quantum device. *Nat Phys* **9**, 570 (2013).

[19] Stanley, M. J. *et al.* Dynamics of a mesoscopic nuclear spin ensemble interacting with an optically driven electron spin. *Phys. Rev. B* **90**, 195305 (2014).

[20] Matthiesen, C., Stanley, M. J., Hugues, M., Clarke, E. & Atatre, M. Full counting statistics of quantum dot resonance fluorescence. *Sci. Rep.* **4**, 4911 (2014).

Chapter 5

Conclusions

In this thesis, a confocal microscope set-up was used to perform photoluminescence (PL) and resonant fluorescence (RF) experiments on self-assembled InGaAs quantum dots (QDs) - details of this set-up are given in chapter 2. A number of different types of QDs (i.e. QDs grown via different processes) were used: partially-capped islands (PCI) and In-flush QDs emitting around 950nm, and dots-in-a-well (DWELL) emitting around 1300nm. The goal of these experiments was the engineering of the emission characteristics of the QDs to develop high-quality photon sources for quantum information applications. Particular regard was given to good single photon statistics (antibunching), indistinguishability, and sources of photon entanglement. Towards this end, strain was applied to charge-tunable QDs to first characterise their single-particle behaviour under strain via a Coulomb blockade model. The feasibility of cancelling the fine structure splitting (FSS) of the neutral exciton X^0 in 1300nm-emitting DWELL QDs was investigated via polarisation-resolved PL, with the aim of producing a source of polarisation-entangled telecommunications-wavelength photon pairs via the biexciton-exciton-vacuum cascade (chapter 3).

RF was used to examine the properties of QDs as high-efficiency coherent emitters of single indistinguishable photons (chapter 4). High-resolution spectra were obtained through the use of a scanning Fabry-Pérot interferometer (FPI). Second-order correlations were measured using a Hanbury-Brown-Twiss interferometer, and photon indistinguishability was examined using the Hong-Ou-Mandel effect.

5.1 Chapter 3 - Strain tuning

The major novel result from the strain tuning experiments here is the further analysis of the effects of external uniaxial strain on the single particle energies in the quantum dot. Firstly, it is clear that the relatively small shift in photon energy due to strain is the result of the large degree of cancellation between the electron and hole tuning rates. This small difference is the result of the specific QD properties, such as size, shape and composition, and so QDs in the same wafer can have very different photon

tuning behaviours – this finding is in line with results in the literature. In addition, the tuning slope of the electron confinement energy dE_C/dp is dependent on the nominal value of E_C: as E_C increases, dE_C/dp decreases. As noted, this makes some intuitive sense, as a large confinement of the electron wavefunction will reduce the effects of an external perturbation on the behaviour of the electron.

Since the tuning of E_C with applied uniaxial strain depends at least in part on the composition of the QD via the change in deformation potential due to the degree of InAs to GaAs, it would seem to be a good idea to attempt to extract the InGaAs conduction band deformation a_c potential from the tuning slope of the electron confinement energy and so extract an estimate of the composition, assuming a linear relationship between percentage composition and a_c. However, the values extracted were unphysical, demonstrating that such a simple model does not capture the whole story, and indeed it is true that the single particle confinement tuning behaviour depends on a number of factors in addition to the deformation potential, such as the height of the QD and the actual shape of the confinement potential itself.

In addition, the fine structure splitting (FSS) of the X^0 in telecom-wavelength QDs was tuned via applied strain along the [110] axis. Firstly, it is found that the distribution of FSS for many dot-in-a-well (DWELL) QDs shows smaller average values for the untuned FSS that had previously been recorded, which is a good starting point for potential cancellation of FSS to generate entangled photons. In spite of this, of the QDs examined under strain tuning, none showed a complete cancellation of the FSS, and only one showed a tuning through a minimum, at around 25 μeV. Further analysis of FSS values and polarisation angles, however, allows the calculation of the "critical stress" p_c at which the FSS will come to a minimum, and this minimum value of FSS due to strain tuning. For all but one of the QDs examined, p_c lies outside the available range of stress $|p| \leq p_{max}$. However, 2 of the QDs measured have a minimum FSS below 1 μeV, obtainable with $|p_c| > p_{max}$, demonstrating the potential, with a larger p_{max}, for efficient cancellation of FSS with strain tuning alone.

5.2 Chapter 4 - Resonance fluorescence

The results of RF experiments give some insight into how spin and charge noise affect the quality of photons emitted or scattered from a QD. The most relevant results come from the scattering of photons at low excitation power and therefore low Rabi frequency $\Omega < \Omega_S$. In this regime, for a ideal X^{1-} 2-level system, the signal is dominated by Rayleigh scattered photons, which inherit the coherence and linewidth of the laser. In reality, though, the hyperfine interaction between the single electron spin and the $\sim 10^5$ nuclear spins splits the system into a 4-level

system. Since resultant Overhauser field fluctuates in magnitude and direction, any in-plane component allows Raman scattering, destroying indistinguishability of scattered photons. The fluctuations of the Overhauser field over experimental timescales result in a broadened doublet in the spectrum around the central Rayleigh scattering peak. This explanation is further supported by the fact that the doublet tunes with the elastic peak as the excitation laser is detuned from resonance: if it were due to an incoherent process, the elastic peak would become detuned relative the broad inelastic peak.

Further, it is established that applying a magnetic field B_{ext}^{Z} in the Faraday geometry that is large compared to the average magnitude of the Overhauser field eliminates the inelastic doublet: this field aligns the electron spin in the z-direction, effectively screening it from any in-plane Overhauser component. Raman scattering is suppressed, leaving highly indistinguishable Rayleigh-scattered photons.

Charge noise, on the other hand, has very little effect on the indistinguishability of the Rayleigh-scattered photons. Charge noise effectively results in a random fluctuation of the detuning of the laser from the resonance. While this has a noticeable effect at high Ω due to detuning-dependent shifts in the Mollow triplet, at $\Omega < \Omega_S$, the major effect is a decrease in overall counts due to the random detuning, with no change to the coherence or lineshape of the elastically-scattered photons, since these properties are inherited from the excitation laser. In fact, detuning from resonance increases the effective saturation Rabi frequency Ω_S', i.e. the Rabi frequency above which the output photons from the QD are predominately from incoherent recombination of the exciton, giving a larger range of laser powers at which the spectrum is dominated by Rayleigh scattering. It is, however, unclear but very unlikely that this increase in "useful" excitation power would offset the overall decrease in counts due to detuning fluctuations, especially considering that higher excitation power leads to an increase in background counts.

5.3 Outlook and further work

5.3.1 Uniaxial strain tuning

The difference in QD photon tuning in a given wafer can be used to tune two emitters relative to one another with one tuning knob. We have shown that strain tuning can be used to tune two spatially separated QDs within the same focus spot through resonance: fine control an bring them into resonance. Photons from two resonant emitters can be made indistinguishable through polarisation control, and so entanglement between the spins in the emitters can be established[1, 2]. In addition, multiple QDs interacting with a common light field (i.e. within one wavelength of each other) should display superradiance: emission of photons from the two QDs becomes coherent, with a decrease in the emission lifetime with attendant increase

in emission intensity[3]. In addition, the photons become temporally correlated, resulting in bunching in the emission signal[4]. Tuning two QDs into resonance and carrying out second-order correlations as in Chapter 4 will verify the presence of superradiance.

The small number of QDs with close-to-zero minimum FSS can be overcome by combining uniaxial strain tuning with another tuning knob[5, 6]. An obvious candidate for this is electric fields, given the charge-tunable device structure, but the range of electric fields available is limited due to carrier tunnelling. Other potential candidates are magnetic field tuning and a second strain axis, which can be facilitated through careful design and engineering of the piezoelectric substrate[7].

5.3.2 Resonance fluorescence

An extension of the current set-up to make it more useful for quantum information applications is the ability to perform pulsed RF. In contrast to continuous-wave (CW) excitation, this allows the deterministic emission of single photons from the QD, and can be realised through the use of an electro-optical modulator (EOM) run by a fast pulse-pattern generator (PPG) to produce very fast pulses. By refining the planar cavity device structure (eg. switching to a 2nd-order cavity with a small, few-pair distributed Bragg reflector (DBR) above the QD, potentially engineering GaAs micro-SILs onto the wafer via focused ion-beam etching (FIB)), the efficiency can straightforwardly be boosted to at least 50%[8], making the QDs high-quality single photon sources.

5.4 References

[1] Duan, L.-M., Lukin, M. D., Cirac, J. I. & Zoller, P. Long-distance quantum communication with atomic ensembles and linear optics. *Nature* **414**, 413 (2001).

[2] Moehring, D. L. *et al.* Entanglement of single-atom quantum bits at a distance. *Nature* **449**, 68 (2007).

[3] Dicke, R. H. Coherence in Spontaneous Radiation Processes. *Phys. Rev.* **93**, 99 (1954).

[4] Hennrich, M., Kuhn, A. & Rempe, G. Transition from Antibunching to Bunching in Cavity QED. *Phys. Rev. Lett.* **94**, 053604 (2005).

[5] Wang, J., Gong, M., Guo, G.-C. & He, L. Eliminating the fine structure splitting of excitons in self-assembled InAs/GaAs quantum dots via combined stresses. *Applied Physics Letters* **101**, 063114 (2012).

[6] Trotta, R. *et al.* Universal Recovery of the Energy-Level Degeneracy of Bright Excitons in InGaAs Quantum Dots without a Structure Symmetry. *Phys. Rev. Lett.* **109**, 147401 (2012).

[7] Trotta, R., Martn-Snchez, J., Ortix, C. & Rastelli, A. Energy-tunable sources of entangled photons: a realistic concept for solid-state quantum relays. *arXiv:1412.5954 [cond-mat]* (2014). ArXiv: 1412.5954.

[8] Ma, Y., Kremer, P. E. & Gerardot, B. D. Efficient photon extraction from a quantum dot in a broad-band planar cavity antenna. *Journal of Applied Physics* **115**, 023106 (2014).